PRESTRESSING OF COMPOSITE STRUCTURES FOR ENHANCED STRUCTURAL EFFICIENCY

By

Mohammad Sayyar Bidgoli

A DISSERTATION

Submitted to
Michigan State University
in partial fulfillment of the requirements
for the degree of

Civil Engineering - Doctor of Philosophy

2014

ABSTRACT

PRESTRESSING OF COMPOSITE STRUCTURES FOR ENHANCED STRUCTURAL EFFICIENCY

By

Mohammad Sayyar Bidgoli

Due to their high strength-to-weight ratio, fiber reinforced polymer composites are finding growing applications in aerospace, automotive, infrastructure and other structural systems. Fiber reinforced polymer composites provide distinctly high tensile strength and modulus, which cannot be matched by their compressive performance. Reversible stress cycles are also detrimental to the fatigue life of composites. Hence, compressive stresses tend to govern the design of composite structures subjected to reversible stress systems, leaving their superior tensile attributes largely under-utilized. This undermines the structural efficiency of composite structures, and carries important weight penalties.

The primary purpose of prestressing is to introduce an initial stress system within the composite structure, which counteracts the critical (compressive) stresses developed in the structure under service loads. Control of critical stresses under service loads benefits the structural performance of prestressed composites, and enables design of structures with enhanced performance-to-weight ratios.

Initial proof of concept investigations focused on design and experimental validation of the benefits of prestressing to flexural performance of composite box sections under quasi-static and fatigue loading. Prestressing was used in this application to improve flexural strength and fatigue life by lowering peak compressive stresses. Theoretical models were developed for design of prestressed composite flexural members, and tooling and methodologies were developed for fabrication of prestressed composite box sections. Experimental results indicated that about 90%

(based on one replicated test) gain in the flexural strength of a specific composite flexural elements could be realized with prestressing which carried a weight penalty of approximately 15%. Fatigue life of the composite flexural element was found to increase by over 100% (based on replicated tests on two prestressed and two non-prestressed specimens) upon prestressing.

More refined applications of prestressing were focused on PRSEUS composite structures which are stiffened composite panels with pultruded ros incorporated in their stiffeners for improved structural efficiency. Use of these pultruded rods as prestressing elements enables prestressing of PRSEUS composite structures with no weight penalty. Use of the unilaterally reinforced pultruded rods in conjunction with multiaxially reinforced constituents which govern failure of PRSEUS leaves the pultrued rods under-utilized at failure. Use of this reserve capacity of pultruded rods towards prestressing eliminates any weight penalties associated with the application of prestressing force. The contribution of prestressing to performance characteristics of an existing design of a rod-stiffened (PRSEUS) composite structure was investigated analytically and experimentally. Experimental results indicated 32% gain in average compressive strength resulting from prestressing of stiffened composite panels. The benefits of prestressing were validated in application to PRSEUS components of different size and complexity. The long-term stability of prestressing force was evaluated experimentally and improved under sustained exposure to elevated service temperatures and also under exposure to freeze-thaw cycles at elevated humidity.

Finite element modeling verified the contribution of prestressing towards enhancement of the structural performance of PRSEUS under compressive loads. The predicted failure mode and ultimate strength of the stringer obtained through finite element modeling agreed with experimental results.

To my beloved parents and my family

ACKNOWLEDGEMENTS

I would like to express my special appreciation to my advisor and committee chairman, Dr. Parviz Soroushian, for his scientific guidance, moral support during the preparation and completion of this study. His trust, patience, knowledge, and great insight have always been inspirations for me.

I also want to express my gratitude to Dr. Burgueno, Dr. Drzal, and Dr. Kodur for serving in my graduate committee, for their interest in my research and careful evaluation of this dissertation. It is a great honor to have each of them to work with. All of my memories that I shared with my colleagues at Civil and Environmental Engineering Department of Michigan State University, and in Technova Corporation will be cherished, and I wish good luck to each one of them. I would like to express my special thanks to Mrs. Fran who motherly supported me during the past 4 years.

Most of all, I want to take this opportunity to express my gratefulness and love to my parents and my family whose words of encouragement and push for tenacity ring in my ears. Without their support, I am not able to overcome the difficulties ahead.

Finally, this dissertation is dedicated to my brother, Pouria. Although he is thousands of miles away, his love gave me hope when I needed it most.

TABLE OF CONTENTS

LIST OF TABLES

LIST OF FIGURES

Chapter 1. Introduction

Due to their high strength-to-weight ratio, composite structures are finding growing applications in aerospace, automotive, infrastructure, and other systems. [1]. Composite (and metal) aircraft structural components are generally thin-walled systems which are prone to buckling modes of failure in compression at stress levels which are below their tensile strength [2]. The reversible nature of stress systems in the same thin-walled structures (e.g. aircraft wing and wind turbine blade shown in Figure 1.a and 1b, respectively), thus leads to designs governed by compression, leaving the tensile strength of composites under-utilized.

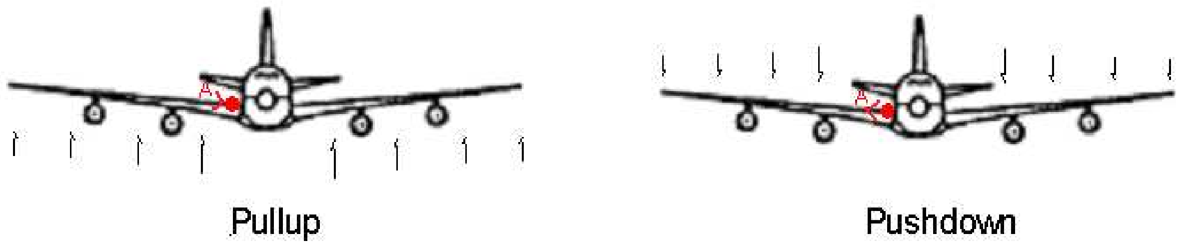

(a) Aircraft Wing

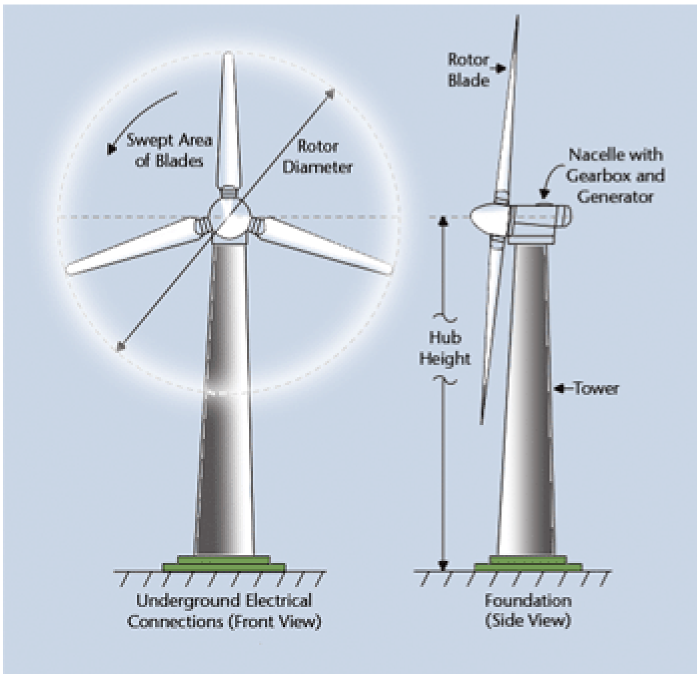

(b) Wind Turbine Blade

Figure 1. Near-Reversible Loading of Aircraft Wings and Wind Turbine Blades.

1.1. Statement of Problem

Landing, takeoff and other maneuvers subject the aircraft wing structure to pull-up and push-down forces of somewhat comparable magnitudes [3]. Similar reversible loading is observed in other composite structures such as wind turbine blades [4], hydrokinetic turbine blades [5], and composite bridge decks [6]. In aircraft structure, the near-reversible loading condition produces near-reversible stress systems within wing structures. For example, the pull-up and push-down forces applied to a wing structure would generate principal compressive and tensile stresses of almost comparable magnitudes at location “A” (See Figure 1a) in the wing structure. This near-reversible nature of the wing stress system leads to important inefficiencies in design of wing structures, as outlined below.

i. Composite (and metal) wing structural components are thin-walled systems (Figure 2a) which are prone to buckling modes of failure in compression (Figure 2b) at stress levels that are smaller than their tensile strength [2]. Some gains in buckling strength of structural panels can be achieved through introduction of stiffeners (Figure 2a) and adjustment of the element configurations [7-10] which carry important weight penalties. The effective compressive (buckling) strength of a composite element depends upon its geometry, mechanical properties and support conditions, the configuration of stiffeners and other supporting elements, and the specific modes of buckling. The effective compressive (buckling) strength is generally only a fraction of the tensile strength. Experimental results on the aircraft stiffened thin-sheet composite structures (few examples are shown in Figures 2b-2e) indicate that the effective (buckling) strength is generally less than tensile strength [11-14]. The reversible nature of stress systems in thin-walled wing structures thus leads to designs governed by compression, leaving the superior tensile strength of composites under-utilized.

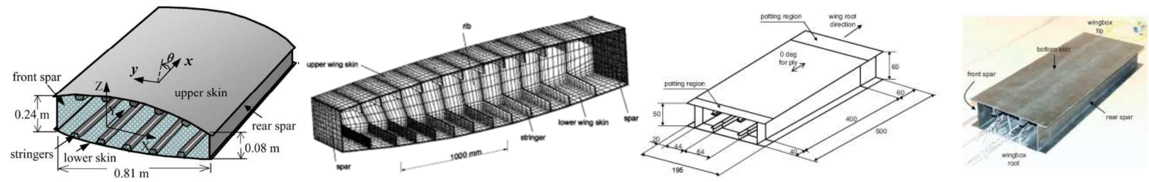

(a) Examples of aircraft composite wing structures [8, 9, 15]

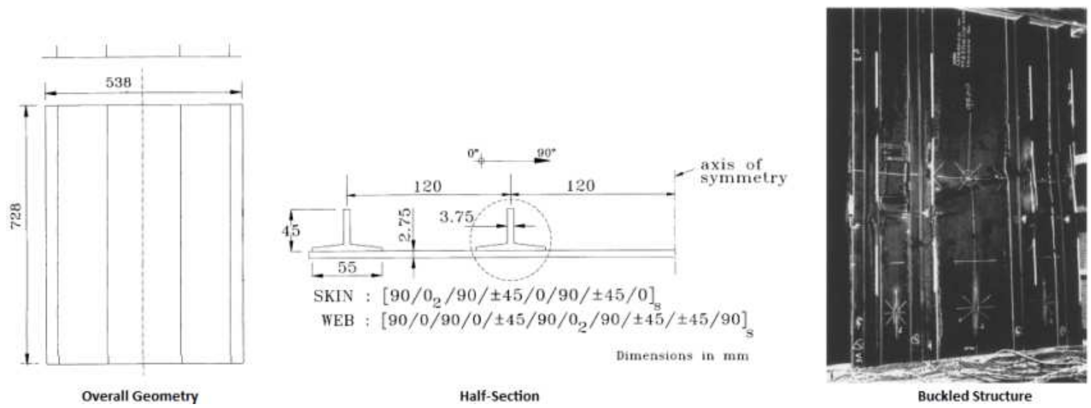

Laminate Tensile Strength: 1,100 MPa   Laminate Compressive Strength: 660 MPa

Effective Compressive (post-buckling failure) Strength: 235 MPa

Effective Compressive Strength – to – Tensile Strength Ratio: 0.21

(b) Example compressive-to-tensile strength ratios for aircraft stiffened composite laminates [11]

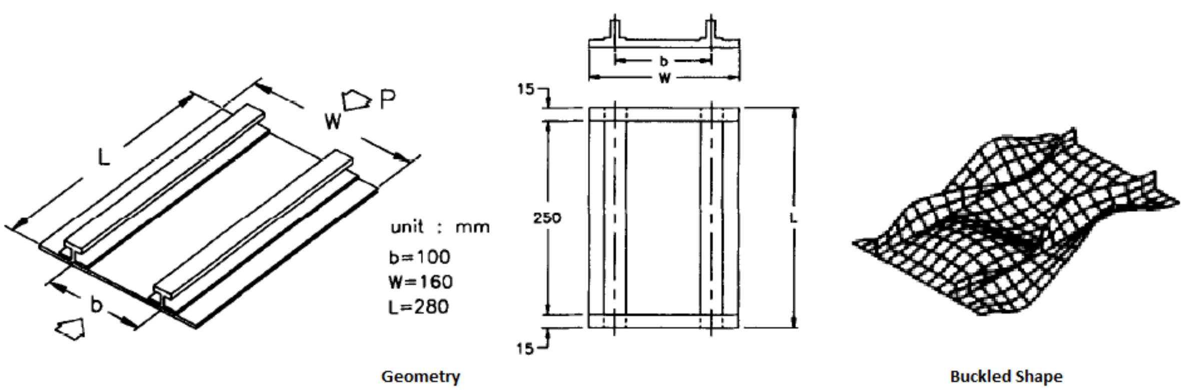

Laminate Tensile Strength: 800 MPa   Laminate Compressive Strength: 420 MPa

Effective (post-buckling failure) Compressive Strength: 175 MPa

Effective Compressive Strength – to – Tensile Strength Ratio: 0.22

(c) Example compressive-to-tensile strength ratios for aircraft stiffened composite laminates [16]

Figure 2. Buckling behavior of composite aircraft structures.

Figure 2 (cont'd).

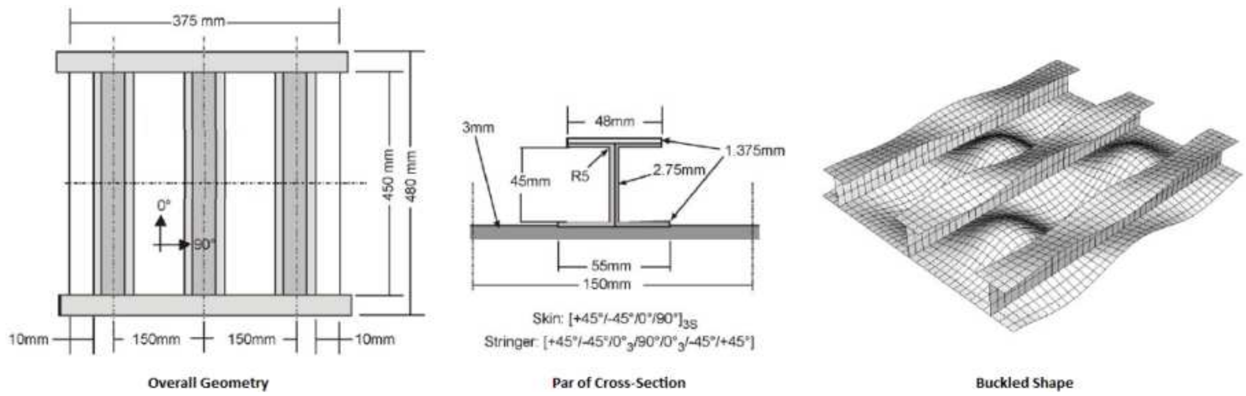

Laminate Tensile Strength: 1000 MPa Laminate Compressive Strength: Not Available

Effective (post-buckling failure) Compressive Strength: 360 MPa

Effective Compressive Strength – to – Tensile Strength Ratio: 0.36

(d) Example compressive-to-tensile strength ratios for aircraft stiffened composite laminates [13]

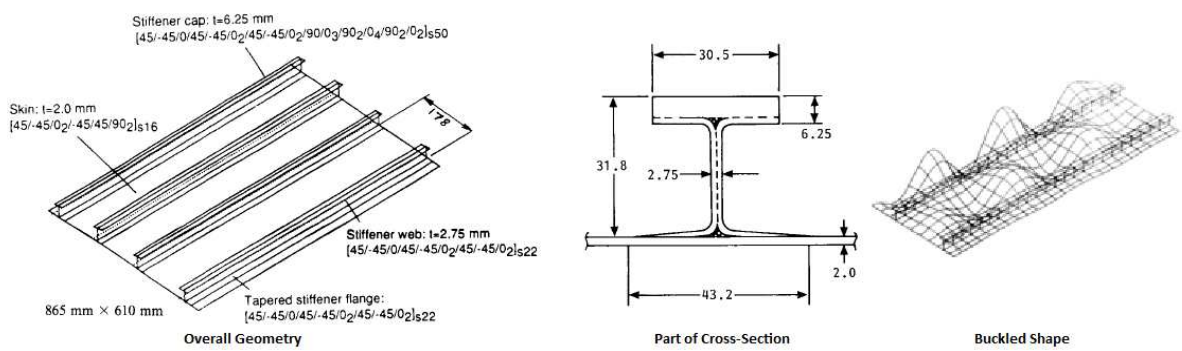

Laminate Tensile Strength: 900 MPa Laminate Compressive Strength: Not Available

Effective (post-buckling failure) Compressive Strength: 195 MPa

Effective Compressive Strength – to – Tensile Strength Ratio: 0.22

(e) Example compressive-to-tensile strength ratios for aircraft stiffened composite laminates [14]

ii. Composites in general (and carbon fiber composites in particular) offer inherently inferior material properties in compression, which further aggravate the problems with their buckling modes of failure. Figure 3a shows the inefficiency of compressive (versus tensile) strain transfer to fibers in composites (in spite of the prevention of the buckling modes of failure).

The compressive behavior of composites is marked by a pronounced nonlinear behavior with serious loss of (tangent) modulus and relatively low strength. The inferior performance of composites in compression has been attributed to the intrinsically nonlinear compressive behavior of (carbon) fibers, formation of low-modulus (interphase) zones within matrix in the vicinity of fibers, gradual deterioration of shear transfer efficiency in compression, and formation of an unstable kink band (Figures 3b), which is aggravated by the geometric imperfections of fibers, producing matrix stress concentrations and debonding [17-21]. In addition, composite laminates are prone to delamination due to out-of-plane (low-velocity) impact, manufacturing errors, vibrations induced by the propulsion system, or many other common events. Delamination further undermines the compressive behavior of composites [22, 23].

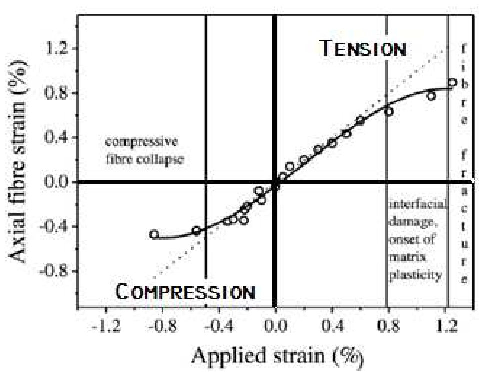

(a) Fiber strain versus composite strain

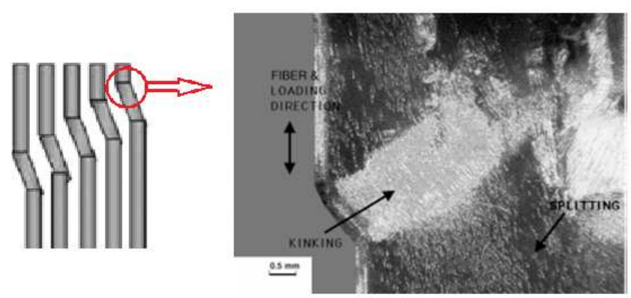

(b) Fiber instability (kinking) in compression

Figure 3. Inferior compressive behavior of carbon fiber composites [11, 12]

iii. The reversible stress system developed in composite wing structures is a major detriment to their fatigue life due to rapid delamination growth [24]. Delaminations form as flaws in composites during manufacturing or in service. Figure 4a shows a delamination caused by low-velocity impact. Under compression, delaminations undergo a mixed mode of buckling (Figure 4b) which induces stress concentration at the delamination front. Cyclic loading of compressed panels with delaminations (and hence repeated delamination buckling) causes a reduction of interlayer resistance as a result of damage accumulation at the tip. Therefore, delaminations that would not propagate under static loading may grow and cause failure after a sufficient number of compression cycles. Delamination growth under cyclic compression undermines the fatigue life of composite wing structures, and also causes deterioration of their strength, stiffness and energy absorption capacity. These damaging effects are particularly pronounced under reversible (compression-tension) cyclic loads when compared with non-reversible (tension-tension or even compression-compression) load cycles. The delamination growth also leads to the initiation of transverse cracks incorporating debris; closure of these partially filled cracks under reversible stress systems generates compressive stresses which further aggravate damage growth under tension-compression fatigue [25]. Figure 4c depicts the severe loss of flexural stiffness (represented by load required to induce a constant flexural deformation) of a composite panel subjected to reversible load cycles (when compared with non-reversible load cycles). Fatigue models [26] predict about four orders of magnitude reduction in fatigue life when a composite laminate is subjected to repeated application of stresses ranging from –100 MPa (compression) to 300 MPa (tension) versus stresses ranging from 0 MPa to 400 MP a (tension).

1.2. Proposed Solution: Prestressing

The approach devised in this research to resolve the structural inefficiencies described above subjects the critical regions of the composite structure to a tensile prestress system which controls the compressive stresses developed under service loads. This approach improves the balance of compressive and tensile stress-to-strength ratios, and also mitigates damaging stress reversals under fatigue loading.

1.2.1. Application in flexural elements

A basic implementation of this approach is schematically depicted in Figure 4 for an aircraft wing structure, where the compression applied to prestressing elements is balanced by the tension developed in the wing structure.

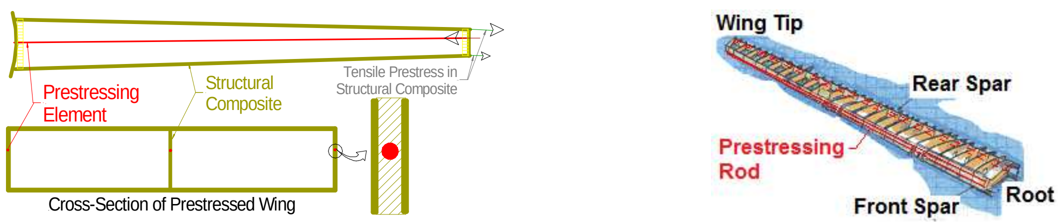

(a) Schematics (b) Use of spar webs to place the prestressing rods

Figure 4. Configuration of prestressing rods within wing structures.

Prestressing is an established practice in infrastructure systems, especially in application to concrete structures for overcoming the low tensile-to-compressive strength ratio of concrete (compared against the low compressive-to-tensile strength ratio of thin-walled polymer composites). Conventional prestressing of concrete with steel tendons (Figure 5a) involves pre-tensioning the prestressing tendons in order to apply a balancing pre-compression to the structure. Alternatively, prestressing can be used in a circular configuration to apply a hydrostatic pressure which counteracts the internal pressure of cylindrical structural systems, thus reducing the hoop tensile stresses developed in (concrete) structures under internal pressure.

Some common applications of prestressed concrete structures include long-span bridges (Figure 5b), roof shells (Figure 5c), and cantilever structures (Figure 5d).

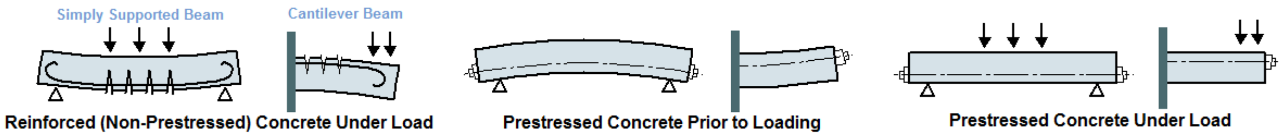

(a) Prestressed concrete principles

(b) Prestressed concrete bridge

(c) Prestressed concrete roof shell

(d) Prestressed concrete cantilever

Figure 5. Examples of prestressed concrete infrastructure systems.

Furthermore, the approach to prestressing proposed here improves the balance of compressive and tensile stress-to-strength ratios, and also mitigates damaging stress reversals under fatigue loads. The pre-tension applied to the critica regions of the composite structure by prestressing reduces the compressive stresses that would be developed in the structure under external loads. Given the relatively low compressive strength of composite structural elements, lowering of compressive stresses by prestressing can improve the effective load-carrying capacity of structures, enabling design of structures of reduced weight and improved service fatigue life). Figure 6 schematically depicts the stress systems developed in a non-prestressed structure under service loads, the prestress system, and the lowering of compressive stresses caused by prestressin.

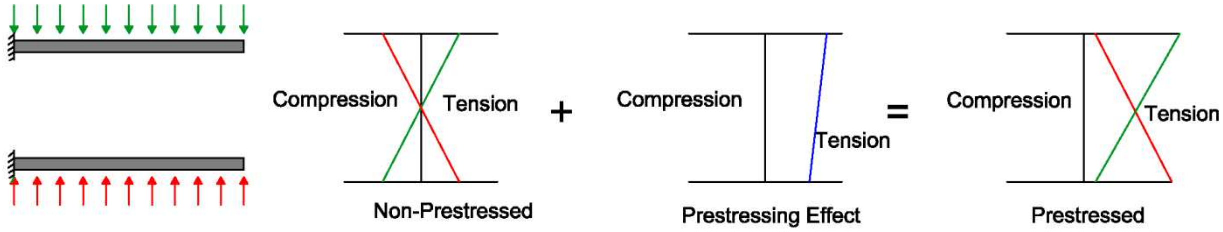

Figure 6. Flexural stress distributions in non-prestressed and prestressed composite structures.

Figure 7 shows a simplified configuration of prestressing elements in the web of the wing box section beam. The pre-compression force in the rods balances the pretension force developed in the composite box.

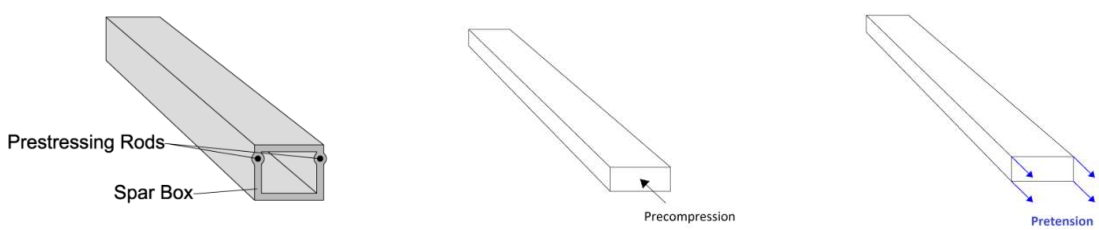

(a) Spar box with pultruded rods (b) Resultant pre-compression force (c) Balancing pre-tension

Figure 7. Schematics of a simplified prestress system in a composite box section beam.

1.2.2. Application in composite panel

Aircraft fuselages are shifting from metallic structures to composite to achieve lower weight thus higher fuel efficiency [27]. The composite stiffened panels are used in structures prone to buckling under compressive service loads. In order to prevent the early buckling modes failures, panels are reinforced with stiffeners [28]. The post-buckling strength of composite structures largely depends on the stiffener geometric configuration and spacing. Different stiffeners types such as J, I, and hat have been used extensively with composites following the example of metal stiffeners [29-31]. The Pultruded Rod Stitched Efficient Unitized Structure (PRSEUS) concept [32] has been introduced by Boeing and NASA as an efficient stiffened composite panel configuration. The highly integrated nature of PRSEUS (rod-stiffened) composite structures is evident in the strategic placement of carbon fibers (Figure 8). The 0-degree fiber in pultruded rod increases the local strength/stability of the stringer section while it also shifts the neutral axis away from the skin to further enhance the overall panel buckling resistance. Frame elements are placed directly on the skin surface, and are designed to take advantage of carbon fiber-tailoring by placing bending- and shear-conducive layups where they are most effective. In its entirety, this integral panel design is intended to first exploit the orthotropic nature of carbon fibers, and then to suppress the out-of-plane failure modes with through-the-thickness stitching. Taken together, these two features enable the application of a new damage-arrest design approach for composite structures [33, 34]. This research projects focuses on the application of prestressing towards enhancing the resistance of PRSEUS composite structures against buckling modes of failure. PRSEUS composite structures (Figure 8a) embody high-modulus and high-strength pultrudd rods in ‘stringers’ (Figure 8b). Figure 8c depicts the weight savings realized by replacing conventional composite structural systems with PRSEUS in application to blended wing body aircraft. The uniaxially fiber reinforced pultruded rods are under-utilized in the prevalent failure modes of PRSEUS, which are governed by material failures/instabilities of the multiaxial fibre reinforced, thin-section composite constituents. The reserve capacity, geometry and positioining of pultruded rods in PRSEUS suit their use towards prestressing of the structural system without any weight penalty. Prestressing also benefits the fatigue life of composites by mitigating detrimental stress reversals and compressive stress excursions under the fatigue loads experienced by the structure in service [35].

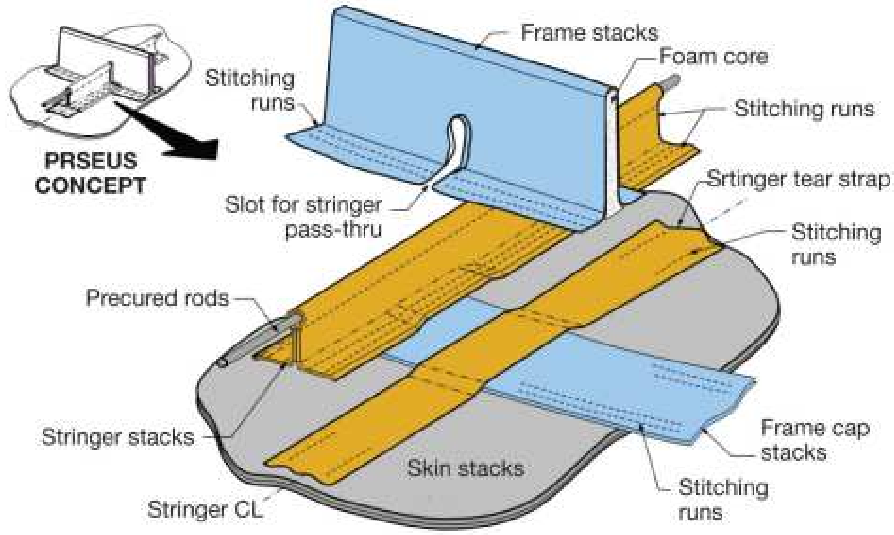

(a) PRSEUS preform assembly

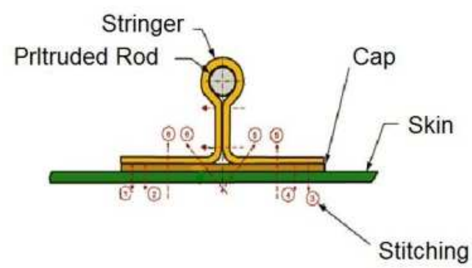

(b) Stringer with pultruded rod in PRSEUS

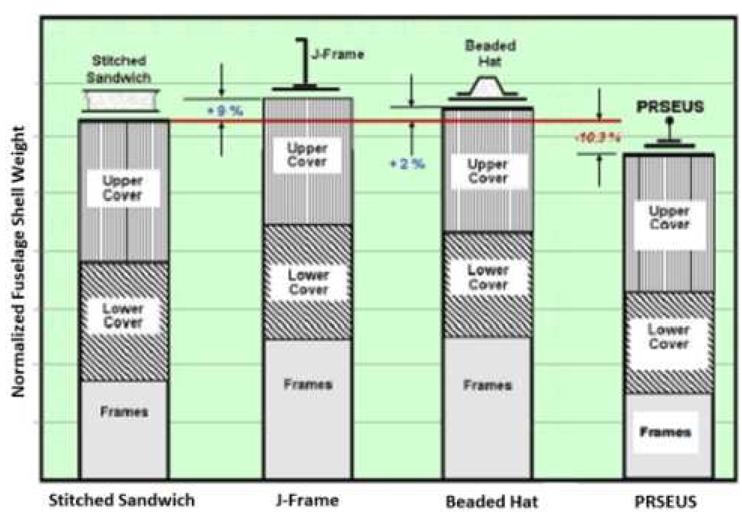

(c) Weight saving offered by PRSEUS

Figure 8. Schematics and comparative merits of the prseus (rod-stiffened) composite structures system [32].

Under-utilization of the pultruded rod in PRSEUS, the failure of which is prompted by that of the multiaxial composite constituent, is schematically depicted in Figure 9a by compraing the corresponding stress-strain curves. The prestress systems in different constituents of PRSEUS are shown in Figure 9b. As shown in Figure 9c, the prestress sysem increases the 'effective' strength of the multiaxial composite constituent of PRSEUS (using the under-utilized capacity of pultruded rods) to realize a balanced failure which makes effective use of all PRSEUS constituents. The prestress system shown in Figure 9b can be conveniently developed using simple tooling (Figure 10a) that is inspired by the way forces are transferred to a bicycle brake (Figure 10b). Force is transferred to bicycle brake via a wire that is surrouned by a plastic tube. The wire tensile force is balanced by the tube compressive force. This enables transfer of tension without straightening of wire because interfacial forces restore equilibrium (Figure 10c). In short, the wire transfers tension to brake without straightening because its tension is counteracted by the compression developed in the tube; forces are thus equilibrated at any point along the curved wire, enabling it to transfer tension without straightening. By the same token, the prestressing tooling depicted in Figure 10a can induce internal prestressing irrespective of the geometric complexity and size (with due consideration given to frictional losses) of the structural system. The prestressing process involves pre-compressing the pultruded rods while pre-tensioning the multiaxial composite using end fixtures, followed by establishing bond (via curing of an adhesive film) between the pultruded rods and the multiaxial composites, and finally removal of end fixtures (the prestressing tooling) for stress transfer via interfacial bonds.

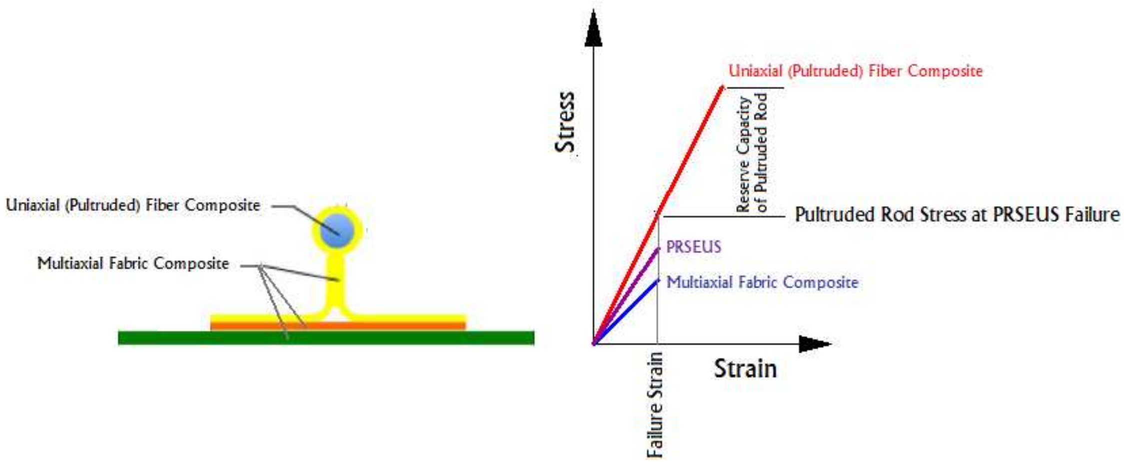

(a) Stress-strain curves of PRSEUS and its constituents (up to failure of PRSEUS)

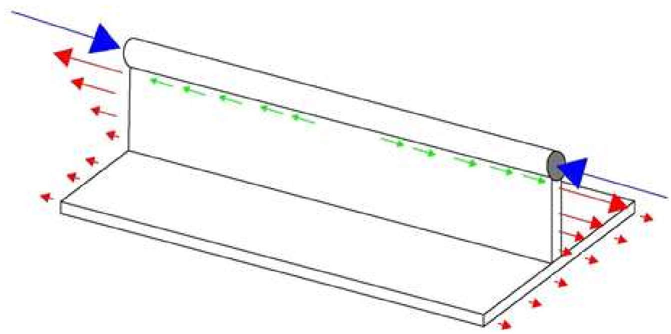

(b) Internal prestressing scheme

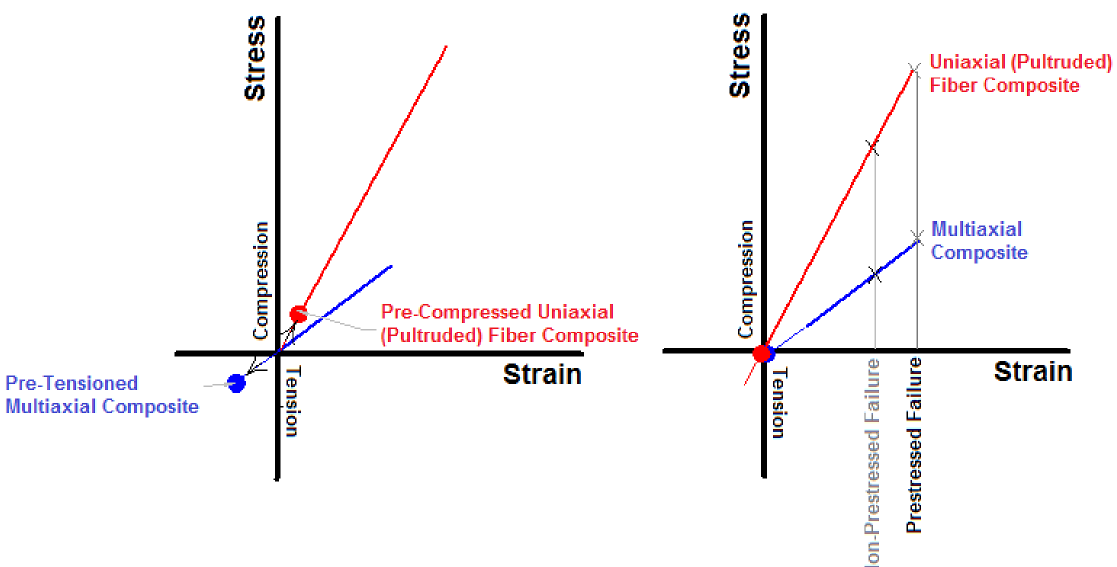

(c) Effective use of PRSEUS constituents via effective prestressing

Figure 9. Inernal prestressing of prseus without any weight penalty.

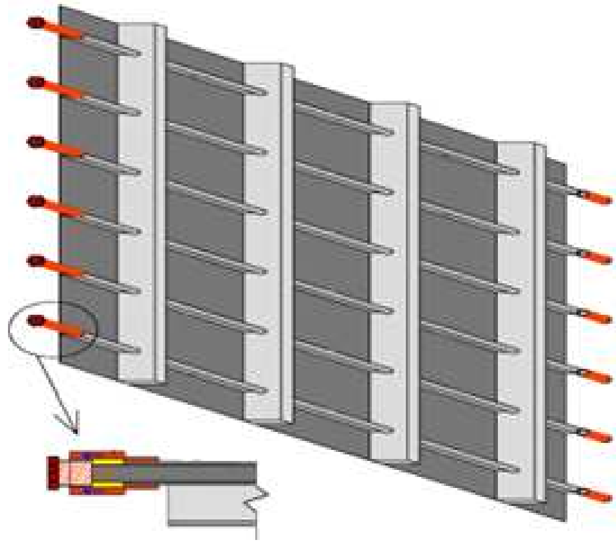

(a) Scalable prestressing tooling

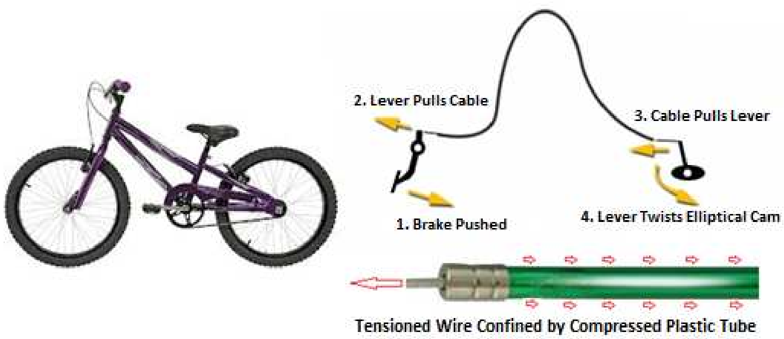

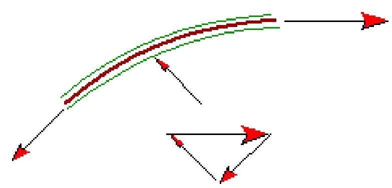

(b) Bicycle brake system

(c) Equilibrium of forces on a wire segment

Figure 10. The prestressing tooling, and principles based on which it operates.

1.3. Research objectives

The primary objectives of the project were: (i) design of prestressed composite structures, development of prestressing methods for application to composites, and experimental validation of the prestressing benefits to the structural performance of composites; (ii) assessment and improvement of the stability of the prestressing force in composite structures; and (iii) development and validation of finite element models for structural analysis of prestressed composites.

The effects of prestressing, as a means of inducing a stress system which counteracts the critical stresses developed under service loads, on composite structures are investigated. The benefits of prestressing are assessed both experimentally; analytical and numerical models are also employed to explain the contributions of prestressing to the structural performance of composites. Different prestressed composite structures of growing size and complexity were designed, fabricated and evaluated experimentally in order to verify the structural benefits of prestressing under loading conditions (quasi-static flexure and compression, and flexural fatigue). Finite element analyses of prestressed composite structures were conducted in order to provide further insight into the prestressing effects on composite structures.

1.4. Background

Applications of prestressing have been investigated in some composite structures in order to improve their structural and/or aerodynamic performance. Pretensioniong of fibers has been proposed as a way to minimize the residual stresses and to improve the mechanical properties of composites [36-38]. Improvements in impact resistance of composite structures by pretensioning of fibers have also been reported by Fancey [39]. Schulte proposed prestressing of carbon fiber composites in order to enhance their resistance transverse cracking [40].

Prestressing has been applied to composite flywheel rotors; this is accomplished via prestressing of multiple rims to generate compressive radial stresses which counteract critical tensile radial stresses generated in service normal to the direction of fibers (Figure 11) [41]. In pressure vessels, metal liners have been prestressed (subjected to hoop pre-compression) via pretensioning of an overwrapped composite [42]. A similar concept has been used in light-weight guns with a prestressed carbon fiber composite overwrapping the gun tube in large caliber weapons systems [43]. The prepreg overwrapping was applied under tension resulting in a favorable prestress in the composite jacket. The design resulted in a gun tube that was 93 kg (corresponding to 10%) lighter than its all steel counterpart while maintaining the same performance. Pre-tensioning of fibers during filament winding and curing of composites [37, 44, 45] has indicated that straightening of pretensioned fibers benefits the structural performance of composites. Prestressing has also been employed to produce bistable composites [46-48] for use in aircraft wing airfoils (Figure 12). It has been shown that it is possible to induce bistable behaviour in symmetric laminates due to careful tailoring of the residual stresses across the width of the laminate. Almeida et al. investigated the aeroelastic stability of flutter in aircraft composite panels, subject to the effect of stress stiffening caused by the piezoelectric actuator (PZT) [49]. A significant increase of the aeroelastic stiffness in flutter was achieved via piezoelectric actuation (prestressing), with the piezoelectric actuator bonded to the vibrating structure. The study showed that it is possible to increase the aerodynamic pressure factor, therefore the airspeed, upto72% under specific conditions.

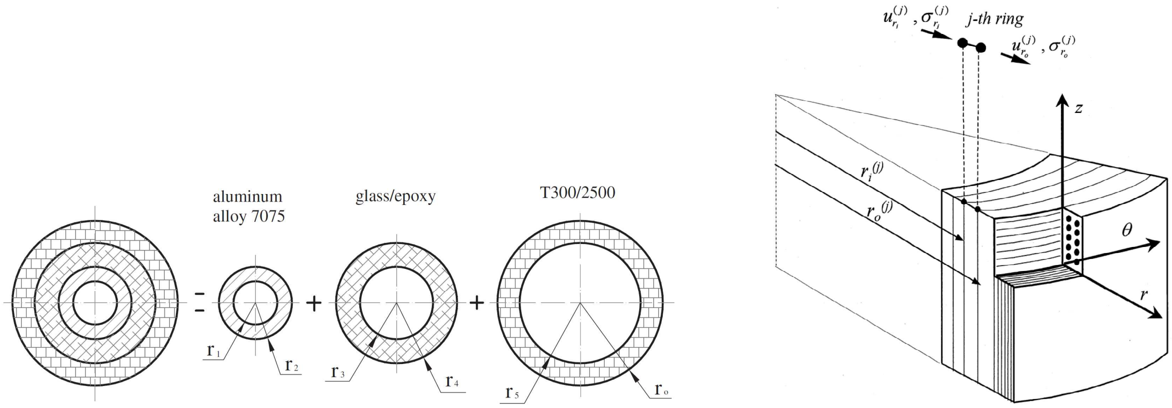

Figure 11. Schematics of flywheel composite rotors

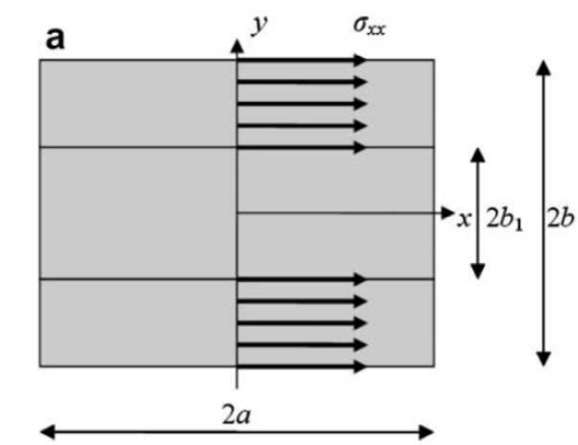

(a) Stress distribution immediately after curing

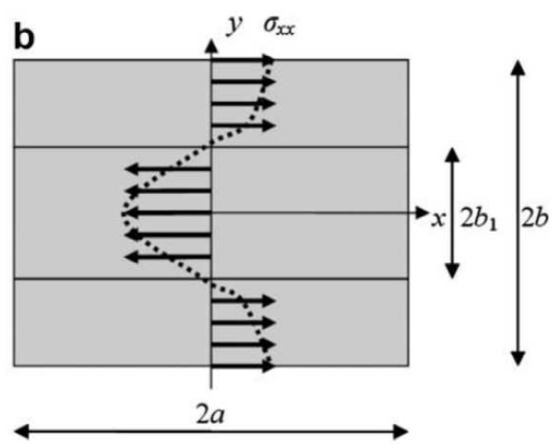

(b) Stress distribution upon cooling and tooling removal

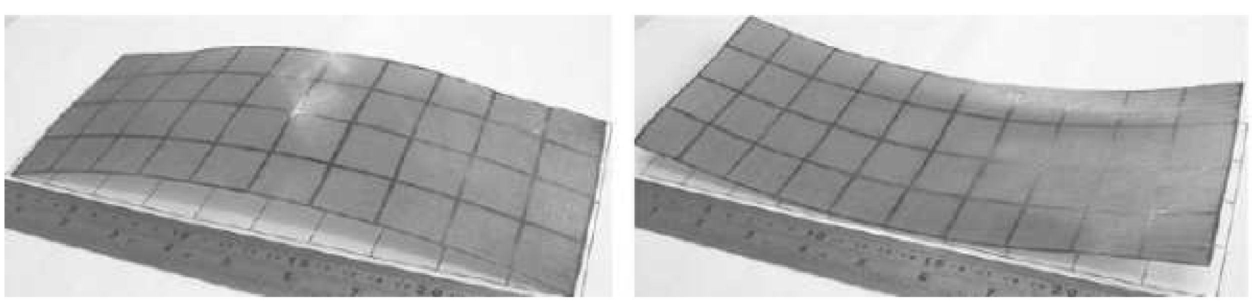

(c) Geometries of a typical GFRP prestressed buckled laminate

Figure 12. Development of Stress Distribution in Bistable Laminate Composites [46].

Carbon fiber composite bars have been used as replacement for steel tendons in prestressing of composite structures; their corrosion resistance enables external prestressing for upgrading and repair of existing bridges (Figure 13). Prestressed carbon fiber composite sheets anchored upon concrete surfaces via adhesion and/or mechanical anchorage are also used increasingly toward upgrading and repair of bridges and other structures. [50-52].

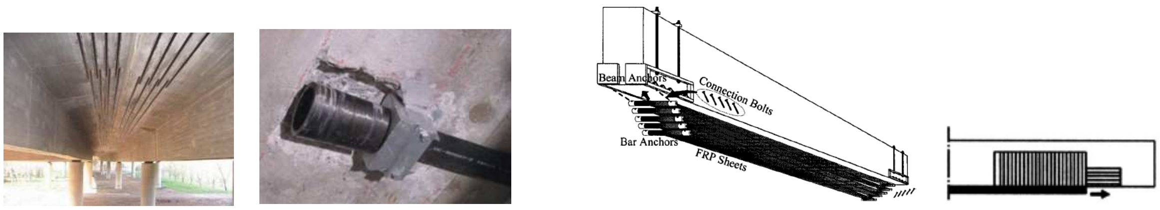

(a) Prestressing composite bars (b) Prestressing composite sheets

Figure 13. Repair/rehabilitation of a reinforced structures concrete through external post-tensioning using composite (a) bars; (b) sheets [51, 52].

Some previous investigations have employed prestressing to control flexural stresses or delay local buckling of structural components. The main thrust of this research is to use prestressing towards improvement of the structural performance and efficiency of composite structures under flexural (Chapter 2) and compressive (Chapters 3 & 4) loading conditions. Finite element modeling was employed in order to gain insight into the prestressing effects on the stress paths and failure modes of composite structures (Chapter 5).

Chapter 2. Application of Prestressing to Enhance the Flexural Strength of Composite Beams

2.1. Introduction

Comprehensive analytical and experimental studies were conducted to assess the benefits of prestressing to the structural performance of composite box beams under flexural loading.

Nature has also resorted to prestressing to achieve enhanced load-bearing capacities. The trunks and branches of trees carry internal stresses that help them against external wing loads. If a trunk is cut into planks, reassembling of the planks will not get produce the original trunk. The center of the tree trunk is in compression, and the outer layers are in tension (Figure 14a). This prestressing configuration uses the superior compressive strength of heartwood (core) to control the damaging compressive stresses that would otherwise develop in the outer layers under wind loads.

The benefits of prestressing are not limited to significant enhancement of structural efficiency through control of compressive stresses and mitigation of stress reversal under fatigue loads. Prestressing tailors the dynamic response characteristics of structures [53, 54], and can be used to enhance the aeroelastic stability of wing structures. A somewhat related prestressing effect is used by nature towards improvement of flight efficiency. Turkey Vulture (*Cathartes aura*) spreads its wings in the sun (Figure 14b); the dark feathers absorb the solar energy, and the air inside the shafts is warmed. The resulting increase in pressure subjects the shaft body to a pre-tension, which makes the feathers stiffer and thus benefits the efficiency of its flight.

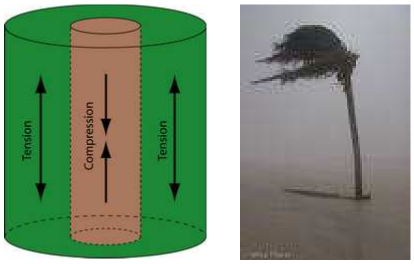

(a) Naturally prestressed tree trunk

(b) Turkey vulture using solar energy to prestress its feather shafts

Figure 14. Examples of prestressing in nature.

2.2. Basic Principles of Prestressing

The approach to prestressing devised here for resolving the above structural inefficiency issues subjects the composite wing structure to a tensile prestress system which controls the compressive stresses developed under service loads. This approach improves the balance of compressive and tensile stress-to-strength ratios, and also mitigates damaging stress reversals under fatigue loads. While the emphasis of this research is on prestressing of the whole wing structure after assembly, one may also prestress the spar alone (prior to assembly) to enhance its structural efficiency. The prestressing rod could be added to the spar web by introducing stiffeners (e.g., hat or box section) onto the webs, within which the rods could be placed.

2.3. Application of Prestressing to Enhance Flexural Performance

The work reported herein concerns enhancement of the flexural performance of commonly encountered beam elements in prestressing. The pre-tension applied upon the wing structure by prestressing reduces the compressive stresses that would be developed in the structure under external loads. Since compressive strength controls the design of wing (thin-walled composite) structural elements, the lowering of compressive stresses by prestressing improves the effective load-carrying capacity of wing structures (enabling design of lighter structures). Typical effects of prestressing on flexural stresses at a wing cross-section are presented in Figure 15. While the non-prestressed wing section develops large compressive stresses, prestressing is shown to lower the peak compressive stress levels.

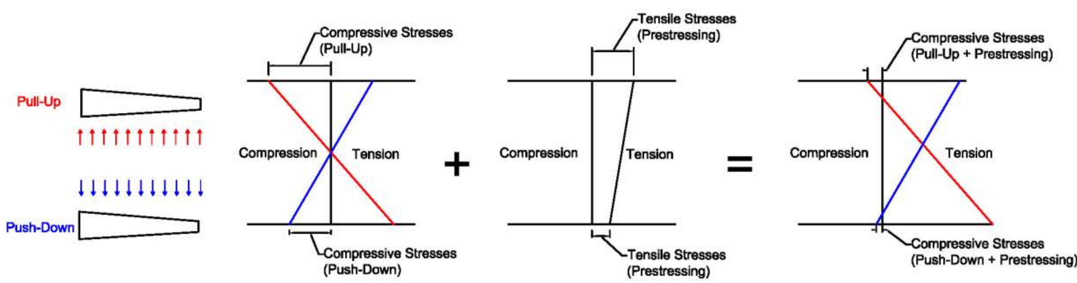

Figure 15. Typical flexural stress distributions in non-prestressed and prestressed wing structures.

This investigation focused on design of a simple wing box section (Figure 16) which was made using carbon fiber reinforced epoxy (5-layer specially orthotropic) laminates with 1.5 mm thickness. Pultruded carbon fiber reinforced epoxy tubes (with square cross sections) were used as stiffeners; two of these tubes (in each box section) carried the prestressing rods. The eccentricity of prestressing rods is noted ‘e’ in Figure 16. This eccentricity as well as the prestressing force applied via prestressing rods would be selected to bring about improvements in the structural performance of wing box sections.

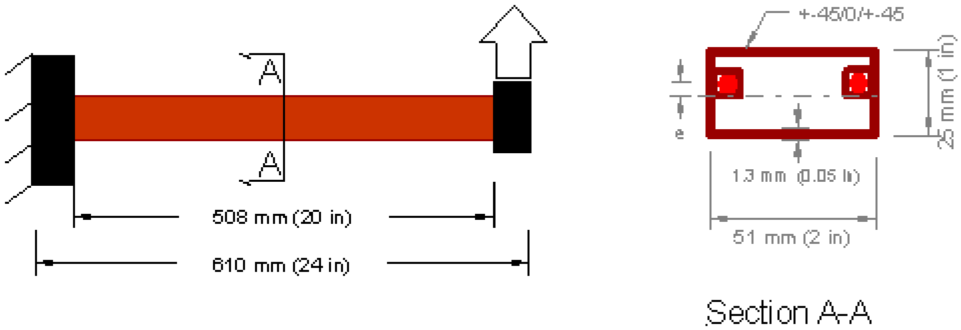

Figure 16. The composite box section.

2.3.1. A Preliminary Design of the Prestressed Composite Box Structure

Some simplifying assumptions were made for a preliminary design of the prestressed composite box structure. The top flange of the box (Figure 16) was assumed to buckle as a plate which is simply supported at edges under in-plane compressive loading. The critical flange buckling load per unit width can then be approximated using the elastic laminate theory as follows [55]:

$$N_{xcr} = (\pi^2/L^2).[m^2.D_{11} + 2\ H.(L/b)^2 + (D_{22}/m^2).(L/b)^4] \quad (1)$$

where, L is twice the cantilever length (see Figure 16), and m is an integer referring to the number of buckled segments developed along length (the governing value of m minimizes N_{xcr}). D_{ij} refers to the bending stiffness coefficients of the laminated composite and H= $(D_{12}+2D_{66})$. For the conditions shown in Figure 16, the buckling stress is σ_{cr}=Nxcr/thickness=104 MPa

In order to design the prestressing system, a 60% gain in a flexural strength of the box structure was targeted. The simple box cross-section provides an area of about 200 mm^2 and a moment of inertia, close to 23,000 mm^4 (with a section modulus of 1,900 mm^3). The non-pretressed nominal flexural strength (at flange buckling) is 198,000 N.mm (corresponding to a force of 389 N applied on the cantilever beam of Figure 7). The 60% gain in flexural strength upon prestressing represents a nominal flexural strength of 317,000 N.mm, corresponding to an applied force of 624 N. The design equations for deriving the values of initial prestressing force, P_i, and eccentricity, e, would be as follows (derived to control peak axial-flexural stresses under different loading conditions) [56]:

Initial Prestressing: $P_i/A+P_i.e/S \le \sigma_{ut}$ (991 MPa) & $P_i/A-P_i.e/S \ge \sigma_{uc}$ (-104 MPa) (2)

Pullup Loading: $0.8P_i/A+0.8P_i.e/S-M/S \ge \sigma_{uc}$ & $0.8P_i/A-0.8P_i.e/S+M/S \le \sigma_{ut}$ (3)

Pushdown Loading: $0.8P_i/A+0.8P_i.e/S+0.6M/S \le \sigma_{ut}$ & $0.8P_i/A-0.8P_i.e/S-0.6M/S \ge \sigma_{uc}$ (4)

where A, S, and I are section area, section modulus and moment of inertia of section, respectively. σ_{ut} and σ_{uc} are ultimate tensile and compressive stress of the box.

Substitution of A=200 mm^2, S=1,900 mm^3 and M=317,000 N.mm in above equations yields:

Initial Prestressing: $P_i/200+P_i.e/1{,}900 \le 991$ MPa & $P_i/200-P_i.e/1{,}900 \ge -104$ MPa

Pullup Loading: $0.8P_i/200+0.8P_i.e/1{,}900-317{,}000/1{,}900 \ge -104$ MPa &

$0.8P_i/200-0.8P_i.e/1{,}900+317{,}000/1{,}900 \le 991$ MPa

Pushdown Loading: $0.8P_i/200+0.8P_i.e/1{,}900+0.6\times 317{,}000/1{,}900 \le 991$ MPa &

$0.8P_i/200-0.8P_i.e/1{,}900-0.6\times 317{,}000/1{,}900 \ge -104$ MPa

The above expressions can be simplified as follows:

Initial Prestressing: $e \le 1.88\times 10^6/P_i -9.5$ & $e \le 197{,}600/P_i +9.5$

Pullup Loading: $e \ge 149{,}625/P_i-9.5$ & $e \ge -1.96\times 10^6/P_i+9.5$

Pushdown Loading: $e \le 2.11\times10^6/P_i-9.5$ & $e \le,-9,250/P_i+9.5$

The design of Figure 7 uses two prestressing rods with about 3.6 mm diameter. These two rods, assuming an allowable (initial) stress of 600 MPa, can apply 12,000 N initial prestressing force (P_i). Substitution of these values of P_i in above expressions yields:

Initial Prestressing: $e \le 147$ mm & $e \le 26$ mm

Pullup Loading: $e \ge -3$ mm & $e \ge -154$ mm

Pushdown Loading: $e \le 166$ mm & $e \le 8.7$mm

The above constraints indicate that the acceptable levels of eccentricity (e) for the initial prestressing force (P_i) of 12,000 N can be met with an eccentricity of 5 mm. These prestressing conditions would increase the flexural strength of composite sections by 60%. The two prestressing rods (with 3.6 mm diameter) add 20 mm^2 cross-sectional area (or 10%) to the original (non-prestressed) cross-sectional area of 200 mm^2.

The peak stresses developed in the simple composite section under initial prestressing, and under pullup and pushdown loads are summarized below (e=5 mm).

Initial Prestressing: $P_i/200+P_i.e/1,900 = 92$ MPa ≤ 991 MPa &

$P_i/200-P_i.e/1,900 = 28$ MPa ≥ -104 MPa

Pullup Loading: $0.8P_i/200+0.8P_i.e/1,900-317,000/1,900 = -94$ MPa ≥ -104 MPa &

$0.8P_i/200-0.8P_i.e/1,900+317,000/1,900 = 190$ MPa ≤ 991 MPa

Pushdown Loading: $0.8P_i/200+0.8P_i.e/1,900+0.6\times317,000/1,900 = 173$ MPa ≤ 991 MPa &

$0.8P_i/200-0.8P_i.e/1,900-0.6\times317,000/1,900 = -77$ MPa ≥ -104 MPa

The above calculations indicated that the stresses developed in box flanges do not exceed the ultimate stresses, with the prestressed system providing 60% greater load-carrying capacity than the non-prestressed system.

Given the adverse effects of compressive stress excursions on the fatigue life of composite structures, the ability of prestressing to avoid or reduce compressive stress development under fatigue loads can be used to enhance the fatigue life of composite structures. The authors have validated this benefit of prestressing through the analytical and experimental investigations reported elsewhere [57]. These investigations point at the stability of prestressing force under thousands of cycles of fatigue loading.

2.3.2. Experimental Program

The Schematics of a prestressed box beam system is presented in Figure 17. The key structural constituents of the system shown in Figure 18 include composite box section, two composite tubes that would incorporate the prestressing rods, and the titanium prestressing rods.

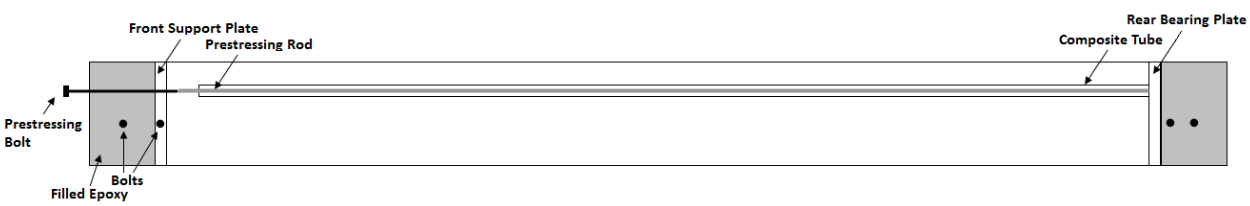

Figure 17. Schematics of the structure, the end-anchorage, and prestressing mechanisms.

Figure 18. Key structural constituents of the system.

The first step in the manufacturing process involves adhering the composite tubes inside the composite box. These tubes would encore the prestressing rods at 5 mm eccentricity (above the neutral axis). Adhesive films were used for adhering the tubes on the interior surfaces of the box section. Wedges were used as tooling for application of pressure on the tubes during curing of the adhesive film (Figure 19a). The composite box with tubes adhered on its interior surface is shown in Figure 19b. Support plates were then placed at the two ends of box section (Figure 20a), followed by introduction of the prestressing rods (Figure 20b), prestressing bolts (Figure 20c), and anchorage bolts (Figure 20d). Filled epoxy (with discrete fiber reinforcement) was then introduced at the box ends (Figure 20e), and cured. The role of epoxy is to transfer the prestressing force from titanium rods to the composite box section. By tightening the prestressing bolts, titanium rods were subjected to compression, which was equilibrated by the tensile force developed in the box section. Composite tubes surrounding the rods prevent them from buckling.

(a) Wedges used for application of pressure on adhesive films (via smaller tubes) during curing

(b) Smaller tubes adhered onto the larger tube

Figure 19. Adhering of the smaller tubes on the interior surface of the larger tube via adhesive films.

(a) Introduction of support plates at two ends

(b) Placement of prestressing rods

(c) Introduction of the prestressing bolts

(d) Placement of the anchorage bolts

Figure 20. Introduction of the prestressing rods, and the end-anchorage and prestressing mechanisms.

Figure 20 (cont’d).

(e) Introduction of filled epoxy

The structure was instrumented with strain gages at locations shown in Figure 21a. A picture of the instrumented structure is shown in Figure 21b. As noted earlier, the prestressing force was applied by simply fastening the prestressing bolts (Figure 21c), with strain gage outputs used to monitor the level of pre-strain (and thus prestress) actually developed in the structure.

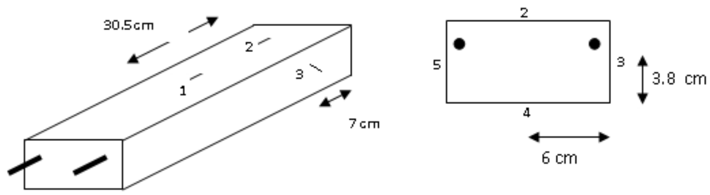

(a) Locations of the strain gages

(b) A picture of the composite structure with strain gages installed

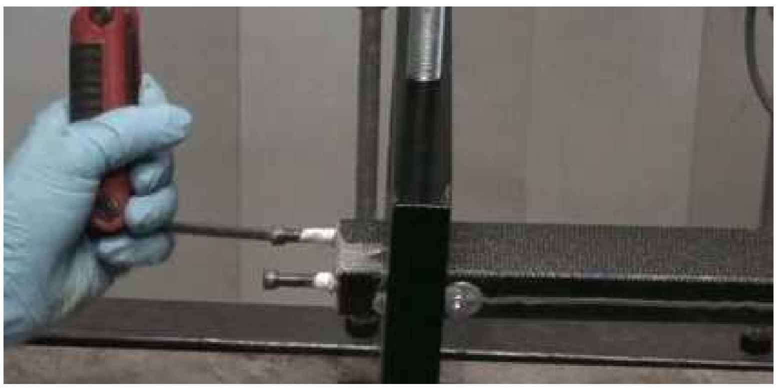

(c) Application of the prestressing force by fastening the prestressing bolts

Figure 21. Instrumentation and prestressing of the composite structure.

The composite box sections were tested as cantilever beams (Figure 22) subjected to uplift load (concentrated at the free end). Tests were conducted at a constant (free-end) displacement rate of 0.1 mm/min with the values of deflection and force as well as strains monitored throughout the tests.

Figure 22. A picture of the flexure test setup.

2.3.3. Load-Carrying Capacity of Non-Prestressed Composite Box Section With and Without Titanium Rods

The experience we have gained throughout the project led to improved design and detailing of the prestressed structure for application of increasing levels of prestressing force. The level of prestressig increased progressively to 100% of design level (full prestressing condition). Test data are presented here causes prestressing forces which increased from 40% up to 100% of the design level.

Experimental studies were conducted in order to determine any gains in the load-carrying capacity of non-prestressed sections (incorporating titanium rods which were only tightened without application of any significant prestressing force). Comparisons were also made with the load-carrying capacity of composite box sections and those of non-prestressed composite sections which did not include the prestressing rods.

Four replicated non-prestressed composite box sections (NN1, NN2, NN3, and NN4) were tested as cantilever beams without introduction of titanium rods. Their ultimate load-carrying capacities were compared against those of four replicated non-prestressed composite box sections (NR1, NR2, NR3, and NR4). The mean values and standard deviations of the test results are summarized in Table 1 and Figure 23. On the average, the introduction of titanium prestressing rods (without application of prestressing force) increased the load-carrying capacity of non-prestressed composite box sections (tested as cantilever beams) by 8% (464.8/428.5=1.085).

Table 1. Ultimate load-carrying capacity of non-prestressed composite box sections tested with and without introduction of titanium prestressing rods.

Specimen	Status	Ultimate Load, N
NR1	With Titanium	447
NR2	With Titanium	456
NR3	With Titanium	473
NR4	With Titanium	483
NN1	Without Titanium	440
NN2	Without Titanium	421
NN3	Without Titanium	431
NN4	Without Titanium	422

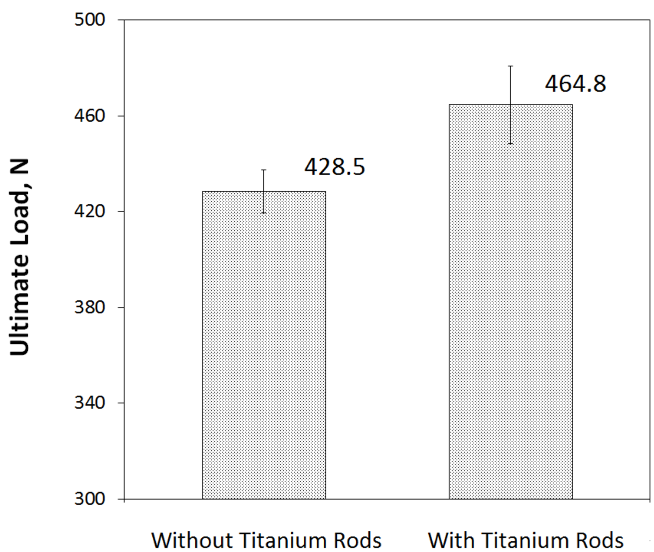

Figure 23. Mean values and standard deviations of the ultimate load-carrying capacities of non-prestressed composite box sections tested with and without titanium prestressing rods.

2.3.4. Prestressing Effects on the Load-Carrying Capacity of the Composite Box Section

In an effort to assess the benefits of prestressing in terms of strength-to-weight ratio, the ultimate load-carrying capacity and weight of prestressed sections were compared against those of non-prestressed sections tested without introduction of titanium prestressing rods. The comparisons made in Table 2 and Figure 24 indicate that prestressing increases the average load-carrying capacity of the composite box section tested in this experimental program by approximately ~90% (based on one replicated test) noting that the non-prestressed sections considered here do not incorporate the titanium prestressing rods. Considering that introduction of the titanium prestressing rods adds 15% to the weight of the composite box section, the average gain in strength-to-weight ratio resulting from prestressing was 64%. When compared with non-prestressed box section which did incorporate the prestressing rods, the average gain in strength upon prestressing was about ~75% (811/464.8=1.74) at similar weight. This experimentally obtained gain in load-carrying capacity upon prestressing compares relatively well with the theoretically predicted value of 60% presented earlier.

Table 2. Ultimate load-carrying capacity of prestressed composite box sections versus non-prestressing sections which did not incorporate the prestressing rods.

Specimen	Status	Prestressing Force, KN	Ultimate Load, N
NN1	Non-prestressed	0	440
NN2	Non-prestressed	0	421
NN3	Non-prestressed	0	431
NN4	Non-prestressed	0	422
PR-1	Partially	5.72	630
PR-2	Partially	7.73	657
PR-3	Partially	10.32	694
PR-4	Fully Prestressed	14.23	811

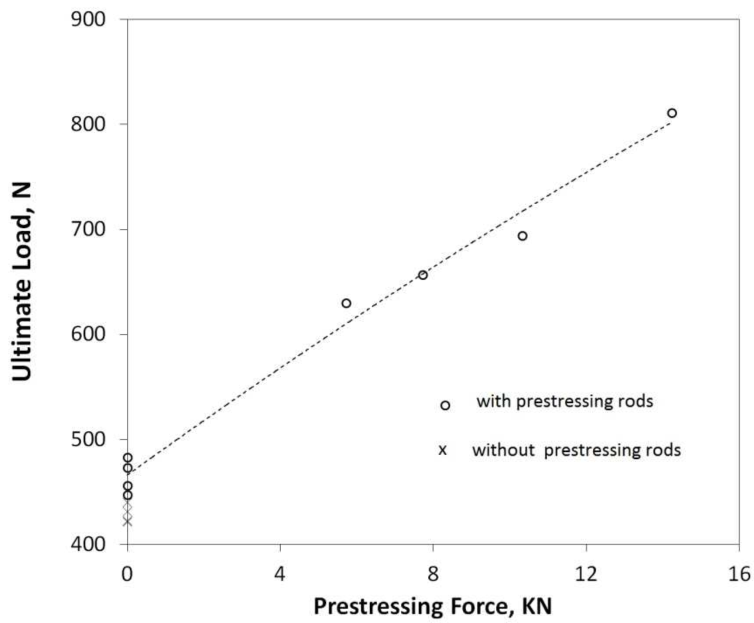

Figure 24. Ultimate load-carrying capacity of composite box sections versus the prestressing force level.

Figure 25 shows load versus tip deflection curves for the fully prestressed and a non-prestressed specimen. It should be noted that the governing failure mode for all non-prestressed and prestressed specimens was buckling of compression flange; prestressing delayed this buckling mode of failure by pretension the flange.

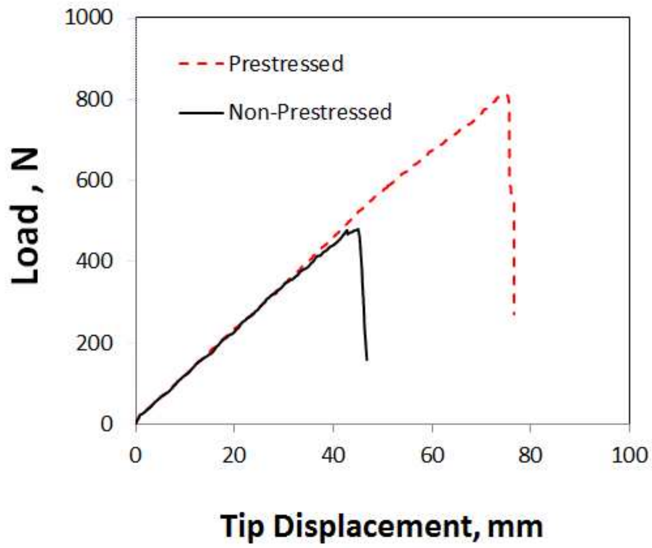

Figure 25. Experimental load-deflection curves for non-prestressed and fully prestressed composite box sections.

Strain gages were installed (Figure 21a) prior to prestressing in order to monitor development of prestrain under loading, data form these strain gages were obtained in order to further insight into the prestressing effects on structural behavior. The strain gage readings under load are presented in Figure 26, pointing that the initial readings (at zero load) are the prestressing levels generated by the prestressing effects. These strain gage readings clearly show that prestress was developed in a section at opposing the negative (compressive) strain system developed under loads, which is why prestressing delays failure of the composite structure under load. It should be noted that loading in this experiment was unilateral to failure.

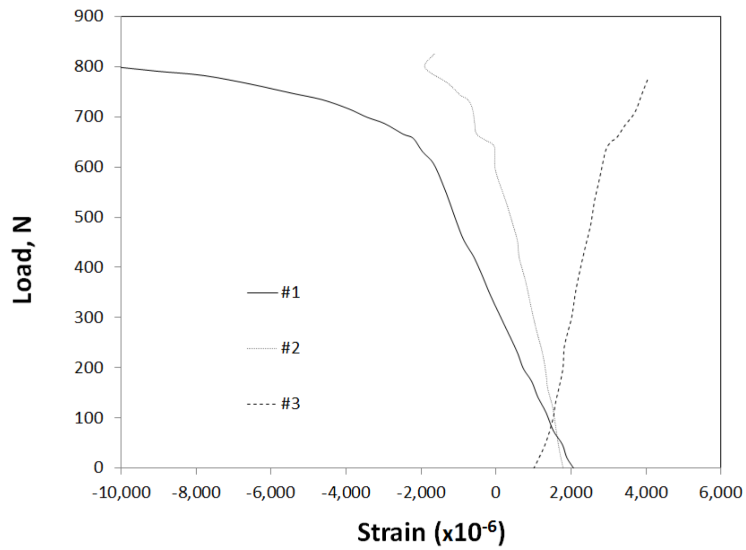

Figure 26. Strain gages reading of the fully prestressed composite box sections.

2.4. Fatigue Life of Composite Structure

As mentioned earlier, performance of composite structures under fatigue loads is greatly depends on the direction of applied load. Caprino and D'Amore proposed a two-parameter model which predicts the fatigue life under both compressive and tensile loads [26].

$$N_t = \left(1 + \frac{\sigma_{to} - \sigma_{\max}}{\alpha_t \cdot \Delta\sigma}\right)^{1/\beta_t}$$
$$N_c = \left(1 + \frac{\sigma_{\min} - \sigma_{co}}{\alpha_c \cdot \Delta\sigma}\right)^{1/\beta_c} \quad (5)$$

where N_t and N_c are fatigue life under tensile and compressive cyclic loads, respectively. σ_{to} and σ_{co} are strength of specimen under monotonic tensile and compressive loading, respectively, and $\Delta\sigma$ is stress range of the cyclic load. It is expected that $\alpha_t \neq \alpha_c$ and $\beta_t \neq \beta_c$, because in general compressive strength decreases following a trend different from the tensile strength. Under tension-compression fatigue loading, the actual critical number of cycles to failure will be the minimum of N_t or N_c.

Table 3. Values of the constants α_t and β_t appearing in Equation (5), calculated for different values of σ_{min} [9].

σ_{min} (ksi)	α_t	β_t
0	0.0838	0.153
–10	0.0423	0.217
–16	0.0366	0.238

The constants in Equation 5 depend on the stress level applied to the specimen. These constants do undergo variations when a tension-compression fatigue loading is applied. Moreover, a clear trend is can be derived from the data presented in Table 3; as $|\sigma_{min}|$ increases, β_t also increases, but α_t decreases. Equation (5), indicates that an increase in β_t and a decrease in α_t lower the fatigue life of carbon fiber composite for high level of σ_{max} (i.e. $\sigma_{max} > 0.7\ \sigma_{to}$).

The adverse effects of reversible stresses in composite wing structures noted above compromise the structural efficiency and thus the weight of aircraft wings. Mitigation or reduction of the reversibility of stresses in wing structures would thus yield benefits in terms of structural efficiency and weight saving [58].

Fatigue is a progressive damage process which undermines the structural qualities of composites. Fatigue damage to composites generally involves matrix cracking, fiber breakage, fiber-matrix debonding, void growth, and delamination. These damage mechanisms degrade such key mechanical properties of composites as strength and modulus. As noted above, fatigue life of composites is significantly lower under repeated tension-compression than under tension-tension loadings. The cyclic (pull-up/push-down) nature of loads applied to wing structures subjects them to tension-compression fatigue loading, which compromises the fatigue life of composites.

One element of our approach to design of prestressed composite (wing) structures involves elimination of compression excursions under fatigue loading. The study reported herein employs prestressing of composite structures to eliminate compressive excursions under repeated reversible (simulating pull-up/push-down) loading, and thus achieve improved fatigue life.

2.4.1. The Prestressing Approach to Resolve Fatigue Problem

As noted earlier, one aspect of the approach to design of prestressed composite (wing) structures involves elimination of compression excursions under fatigue loads; the elimination of compressive stresses enhances the fatigue life of composite structures.

The approach devised to resolve the above structural inefficiencies subjects the composite wing structure to a tensile prestress system which controls the compressive stresses developed under service loads. This approach improves the balance of compressive and tensile stress-to-strength ratios, and also mitigates damaging stress reversals under fatigue loads.

As noted earlier, one aspect of the approach to design of prestressed composite (wing) structures involves elimination of compression excursions under fatigue loads; the elimination of compressive stresses enhances the fatigue life of composite structures. Figure 27 indicates typical effects of prestressing on flexural stresses developed under cyclic loads.

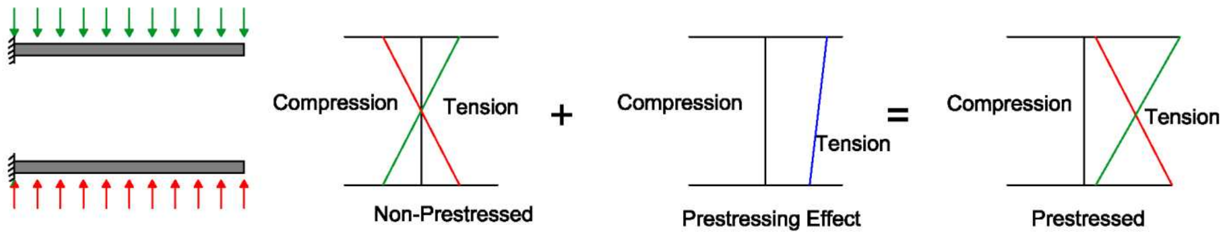

Figure 27. Typical flexural stress distributions in non-prestressed and prestressed wing structures.

This section focuses on experimentally verification of the contributions of prestressing to the fatigue life of composite structures. The fatigue experiments conducted in this project involve repeated flexural loading/unloading of prestressed and non-prestressed composite box sections to a constant maximum deflection (which initially generated a fixed percentage of their corresponding failure loads). The progressive buildup of fatigue damage lowers the maximum load corresponding to the (fixed) maximum deflection under repeated loading. The rate of degradation of maximum load under repeated loading/unloading cycles provides a quantitative means of evaluating the fatigue life of prestressed and non-prestressed composite structures.

2.4.2. Experimental Program

Composite beams with box sections, similar to those used in quasi-static flexure tests, were fabricated and tested under cyclic loading.

Two prestressed and two non-prestressed beam specimens were fabricated and subjected to flexural fatigue loading. The fatigue loading involved subjecting the composite box section, tested as a cantilever beam, to a constant deflection which initially produced a load equal to approximately 70% of the ultimate load of the composite section, followed by full unloading of the section. The repeated stress system developed under this loading condition would be zero-compression in non-prestressed sections, and tension-tension in prestressed sections (which have received an initial tensile prestress).

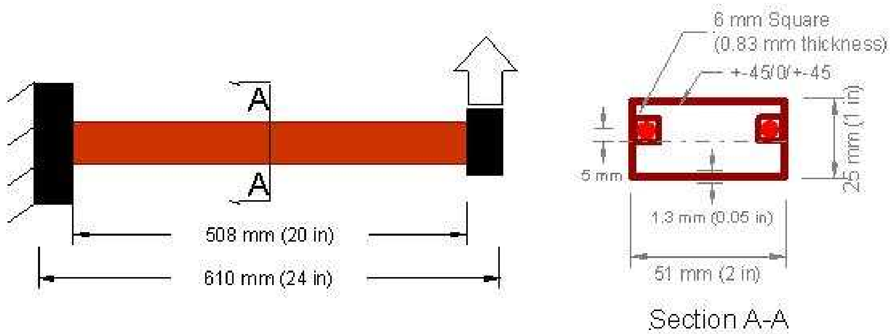

Figure 28. Schematically setup of fatigue specimen and fatigue loading.

2.4.3. Test Results

The prestressed and non-prestressed composite sections were subjected to a load equivalent to approximately 70% of their corresponding ultimate load during the first application of the repeated (constant) deflection. For the non-prestressed specimens, this load produced a peak compressive stress of 0.7x104=-72.8 MPa, which droped to σ_{min}=0 MPa upon unloading. In the prestressed systems, due to the presence of pretension, the stress system reached σ_{min}=9.7 MPa upon loading, and σ_{max}=82.5 MPa in unloaded state.

The initial loading for reaching the targeted deflection did not produce any buckling tendencies. The non-prestressed composite section experienced obvious buckling (Figure 29) of the top (compressive) flange near the fixed end (at peak deflection) after about 47,000 fatigue load cycles. When the loss of modulus compared to first cycle (F_{cycle}/F_0) dropped to 0.7 (where, F_0 and F_{cycle} are the loads at peak deflection prior to and after application of load cycles, respectively). The prestressed composite box section experienced only minor buckling at the same location after a large number of load cycles. For the prestressed system, it took a larger number of cycles (about 95,000) to experience the same loss of modulus (F_{cycle}/F_0=0.7) as the non-prestressed system. Figure 30a and 30b show the prestressed box section (near fixed support) in unloaded and fully loaded states (after about 95,000 cycles),

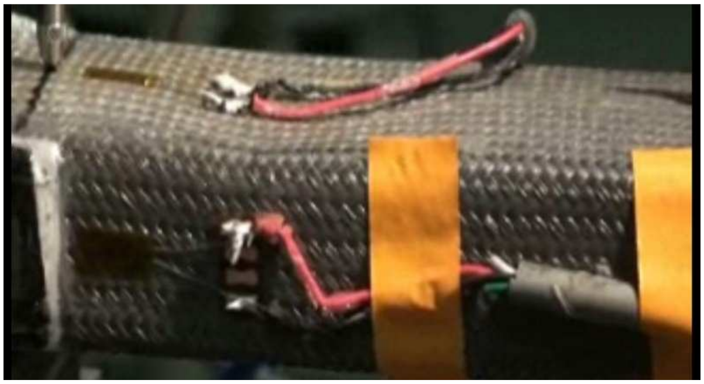

Figure 29. Buckling of the top (compressive) flange of the composite box section after 47,000 cycles of applying a constant deflection.

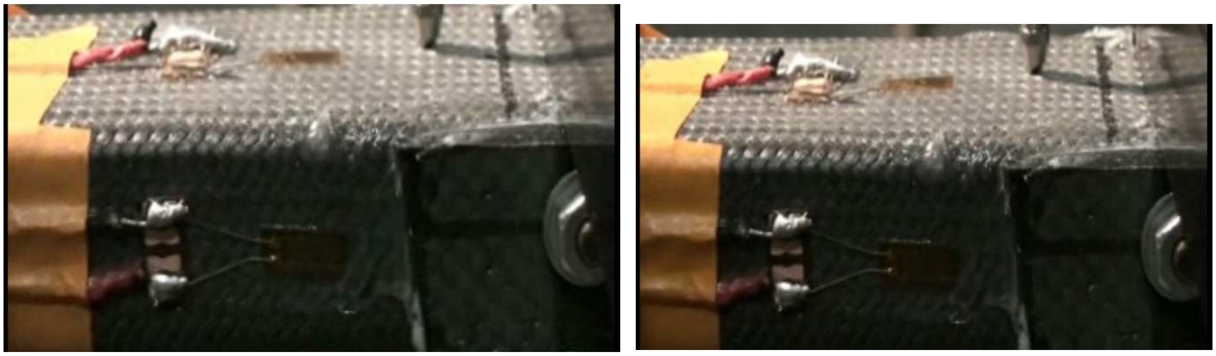

(a) Unloaded state (b) Fully loaded state

Figure 30. The prestressed composite box section appearance near the fixed end after 95,000 cycles in unloaded (a) and fully loaded (b) states.

The displacement developed in the non-prestressed composite cantilever beam under 70% of its ultimate load (490 N) is 34 mm; fatigue testing of the composite beam involved repeated loading to 34 mm peak deflection followed by unloading at a frequency of 4 cycles per minute.

Fig. 31 compares the degradation of peak loads (normalized with respect to their corresponding first-cycle values) with the number of fatigue cycles for replicated non-prestressed and prestressed composite sections. The results presented in Figure 31 confirm that prestressed sections when compared with the non-prestressed ones provide a higher fatigue lives with residual rate of stiffness loss.

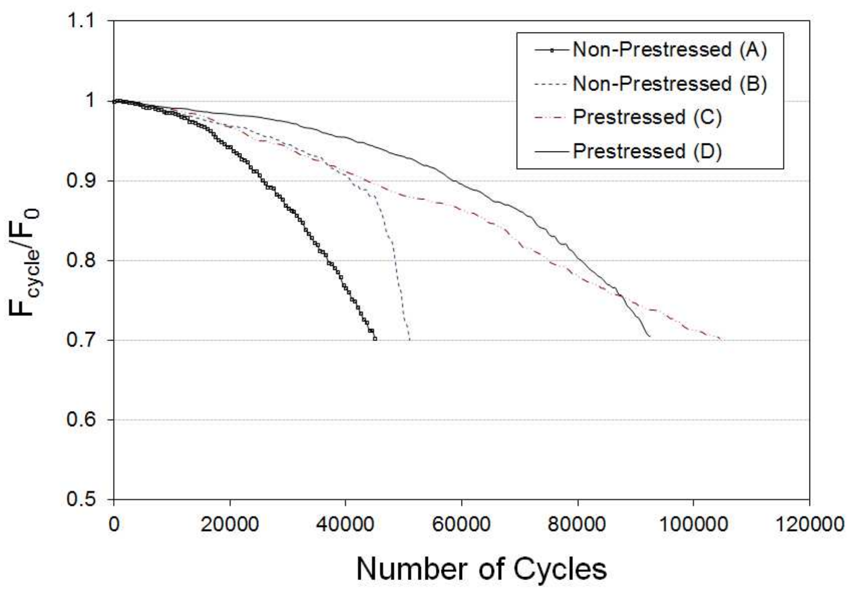

Figure 31. The trends in loss of (normalized) maximum load at constant deformation versus the number of cycles in fatigue tests for replicated non-prestressed and prestressed composite box sections.

In order to appreciate the deterioration effect of fatigue loading, the specimens were subjected to tip loading until failure. The ultimate tip loads (post-fatigue strengths) of samples are presented in Table 4. The average residual ultimate strength of prestressed composite sections (after fatigue failure) is observed to be over ~50% greater that of non-prestressed sections (based the tests on two prestressed and two non-prestressed specimens).

Table 4. Post-fatigue (residual) ultimate load-carrying capacity of prestressed and non-prestressed composite box sections.

Specimen	Status	Ultimate Load, N
A	Non-Prestressed	334
B	Non-Prestressed	347
C	Prestressed	542
D	Prestressed	484

Chapter 3. Processing of Stiffened Composite Panel with Pultruded Rod Incorporated Into Its Stiffener

3.1. Introduction

As a part of this investigation, efforts were made to experimentally verify the contributions of prestressing to the performance characteristics of a composite structure. This experimental work was conducted on an existing design of a stiffened composite panel which incorporated a pultruded rod within its stiffener (developed by Boeing) [59]. This existing design was developed without `prestressing in order to establish the processing methods, and also compare the structural performance of the specimen fabricated in this investigation against those produced by Boeing. This step allowed for validation of the processing methods before assessing the prestressing effects on structural performance.

Laboratory setups were established for processing of the composite structural component (‘stringer’ specimen) schematically depicted in Figure 32. Tolerances and capabilities of the processing system were evaluated. The end products were subjected to axial tests, and the results were compared with those reported in the literature for similar composite structural components.

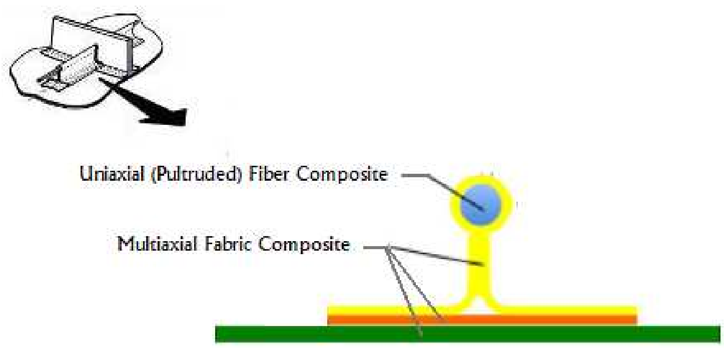

Figure 32. Schematic depiction of the composite structure.

3.2. Materials

The pultruded rods used in the 'stringer' specimens had a diameter of 9.4 mm (0.375 in) diameter, and a smooth surface texture. The pultruded Carbon/Epoxy rods were provided by Acp USA; their elastic modulus and tensile strength were 140 GPa, and 2.3 GPa, respectively. The ultimate elongation of these pultruded rods are reported by the manufacturer at 16,500 microstrain.

This Warp-Knit Fabric (3-D dry fiber preform for PRSEUS) was constructed primarily from warp-knit carbon fiber fabric. The multi-axial fabric is produced commercially on a warp-knitting textile machine in a continuous process (Figure 33). The machine consists of a flat bed (or tenter frame), multiple tow placement devices located over the open bed, a multi-needle sewing machine, and large racks (or creels) for storing the numerous spools of carbon fiber tow. The tenter frame contains two endless chains spaced at a fixed distance with pins pointing vertically upward. The tow placement heads are guided by computerized numerical control (CNC) to lay down tows of fiber while moving back and forth between the two rows of pins. The heads wrap the carbon fiber around the pins. The orientation of the tows is specific for a given ply, and the number of plies in a fabric stack dictates the number of lay-down devices required. The carbon fiber is held under controlled tension to minimize draping as it spans across the width of the tenter frame. The layers of carbon fiber are advanced forward to a multi-needle sewing machine by the endless chains. A tricot stitching seam is then used to sew the individual plies of carbon fiber together with a very fine glass, or thermoplastic thread. The finished product is wound on a support tube as the material exits the sewing machine.

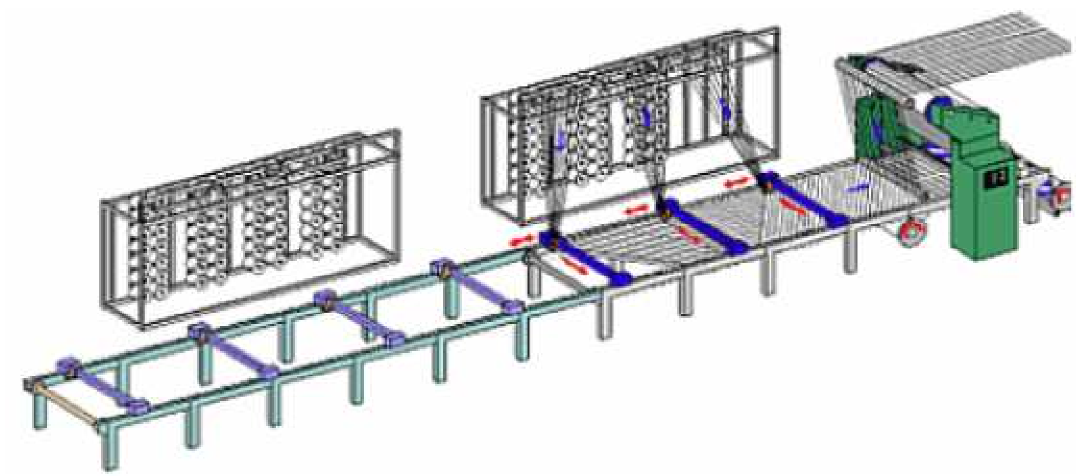

Figure 33. Warp-knit fabric machine.

Fabrics with up to seven plies have been produced using warp-knitting machines. This process is fully automated and cost-effective. It allows the tailoring of material architecture for a specific application. Fiber type, weight, and orientation, in each discrete ply can be specified so that the end product is a customized fabric (Figure 34). With an established supplier base and applications in Boeing and Airbus aircraft, this class of fabrics has been thoroughly characterized.

The PRSEUS panel which is the focus of our project uses warp-knit fabric with nine plies of carbon fiber orientated at -45°, +45°, 0°, 0°, 90°, 0°, 0°, +45°, and -45°. The separate layers of fibers are held together with a 76dtex polyester sewing thread. The seams of tricot stitching were spaced 5 mm apart. The residual seam thread tension is loose for enabling the material to form near-90° angles for stiffener and frame details.

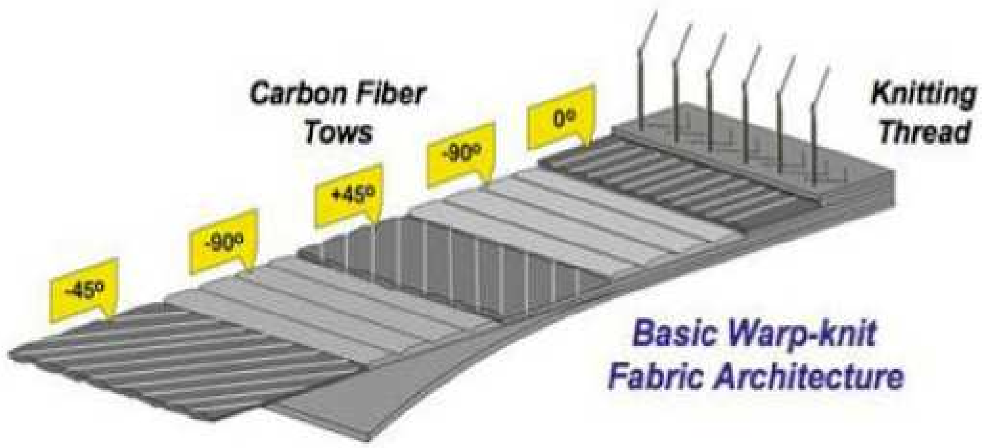

Figure 34. Example of multiaxial warp knit fabric.

The epoxy resin used here was HexFlow VRM-34 supplied by Hexcel. VRM-34 is a structural epoxy for aerospace applications and customized for CAPRI process. Its long pot life of 4 hours facilitates infusion of large structures. The high performance core foam used in frame specimens was WF-110 supplied by Rohacell. The fabric, resin and foam were identical to those used in Boeing's PRSEUS.

3.3. PRSEUS 'Stringer' Composite Specimen

3.3.1. Processing

The Controlled Atmospheric Pressure Resin Infusion (CAPRI), developed by Boeing, was used for processing of composite specimens. CAPRI is a process for resin infusion of a dry fiber preform in a mold cavity under vacuum. The unique feature of this process is that resin is under less than one atmosphere pressure during infusion, and thus a pressure differential between the inside and the outside of the mold tool is maintained upon completion of infusion (Figure 35). Once the mold and preform are completely filled with resin, and infusion has stopped (inlet and outlet lines closed off), this pressure differential produces a net force applied to the vacuum bag and the preform lying underneath. This force keeps the preform in a consolidated (de-bulked) condition, and produces higher fiber volume fractions within the cured laminate than normally achieved in a conventional vacuum assisted resin transfer molding (VARTM) process. Application of a controlled vacuum on the feed pot ensures that: (i) the preform is always under a net compaction pressure, and will be held in position on the forming surface; and (ii) adjustments can be made in the net compaction pressure in order to compensate for thickness variances and also ambient pressure variances [60].

Figure 36 shows the steps taken in our laboratory for preparation of 'string' specimens. The process starts with cutting and kitting of the plies of dry fabrics that make up the skin and stringer components of specimens. A 50-inch wide wrap-knit multi-axial carbon fiber fabric was cut into individual details, and placed into kits. Two 3.4x20 in, one 6x20 in and one 10x20 in piece fabric were used to assemble the stringer specimen. The detailed were then joined by stitching, with two rows of stitching placed along the edges of stringer wall and flanges (Figure 36a). The assembled preform was the transferred to a rigid tool (outer mold) (Figure 36b). Vacuum (outlet) and resin line (inlet) were connected to the preform, and the epoxy resin was pre-heated and degassed for 15 minutes at 250^{o}F. Once the desired vacuum level was reached, resin was introduced into the flow media (which rest on the inner surface of the part) to rapidly move across the part surface before finally migrating through thickness. After thorough infusion with resin at 250°F, the cure cycle was implemented at 350°F (Figure 36c). Figure 37 shows the stringer specimen after removal from the vacuum infusion bag.

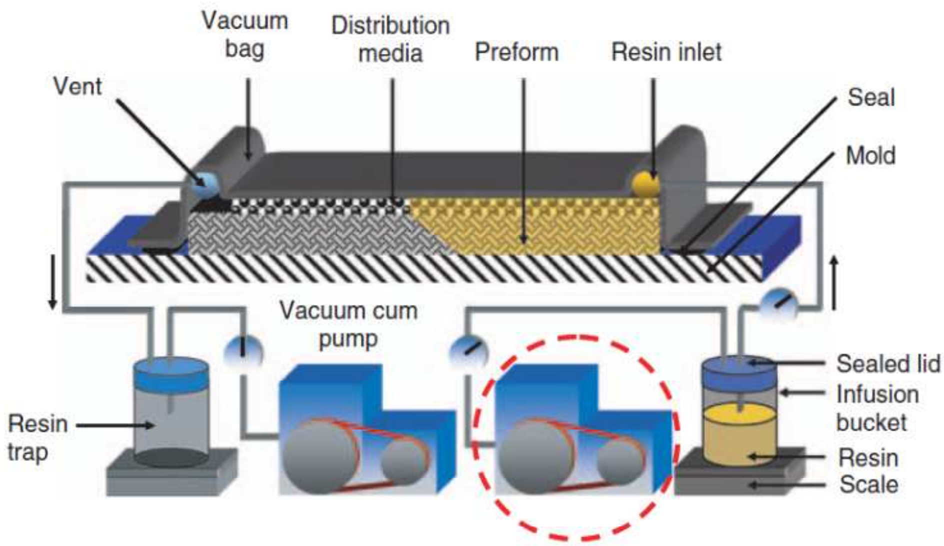

Figure 35. Schematic of the CAPRI process setup [61]

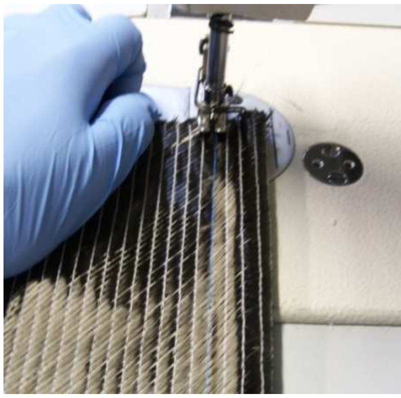

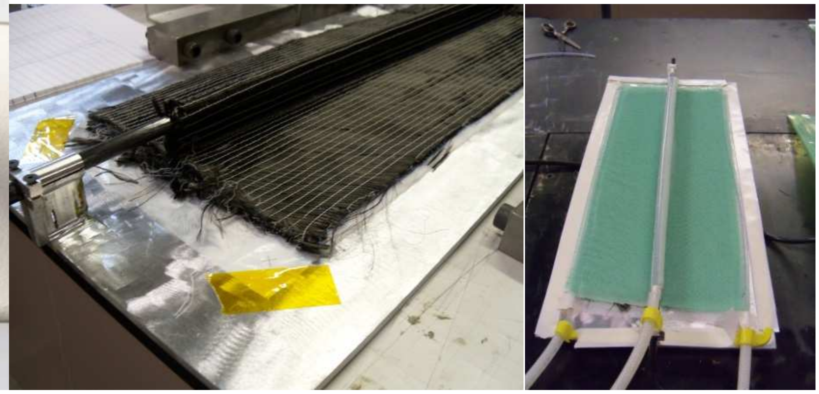

(a) Stitching operation (b) Assembly of preform and tooling

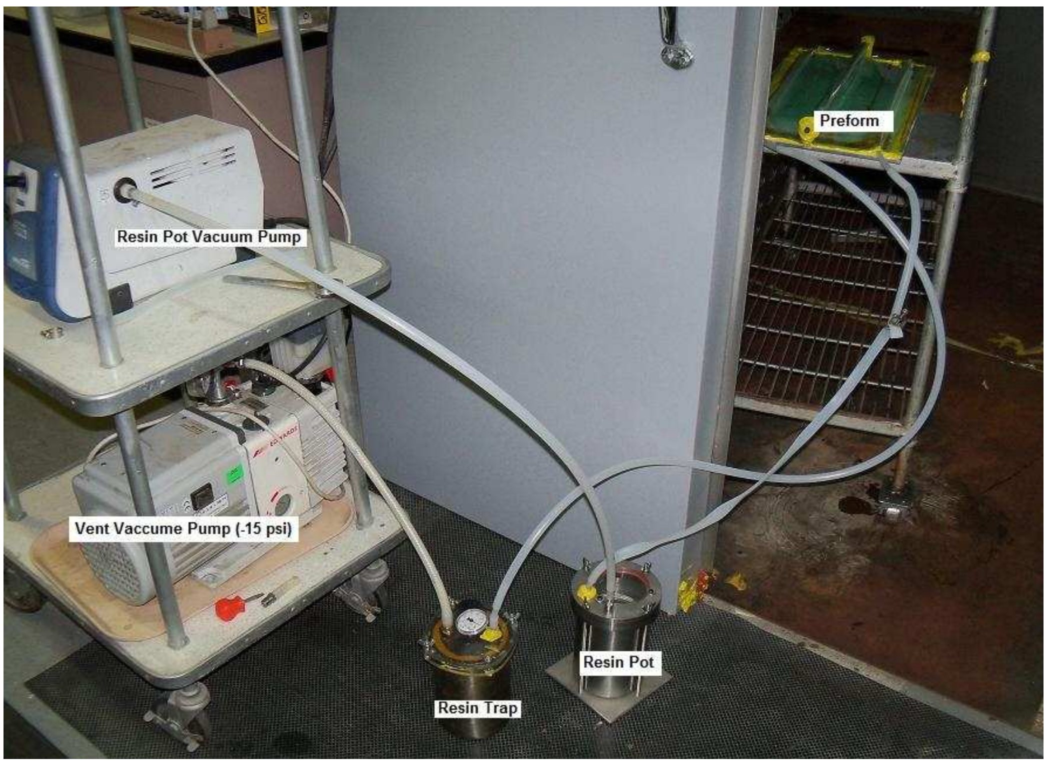

(c) Infusion and curing setup

Figure 36. Fabrication setps.

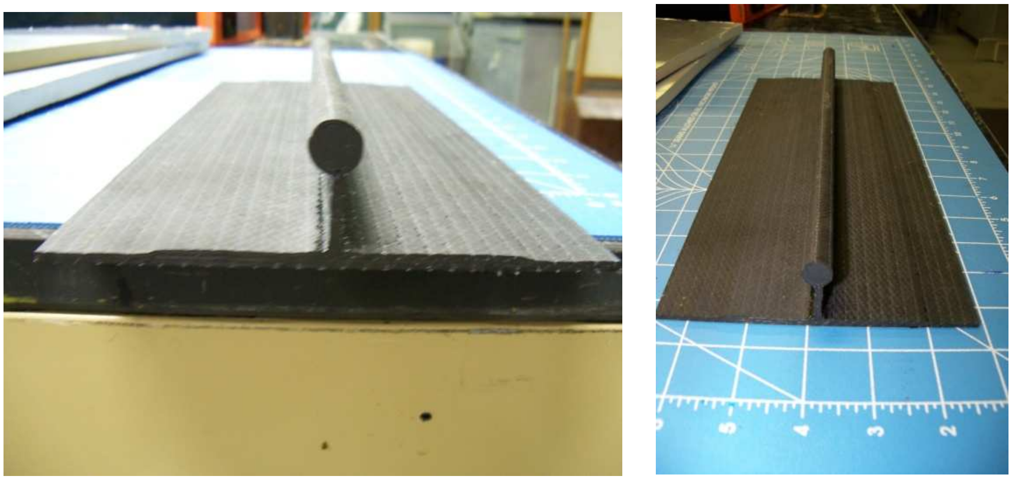

Figure 37. The stringer specimen.

3.3.2. Compression Tests for Process Validating

Specimens were prepared for compression tests by installing end (potted) plates (Figure 38).

The end plates provide a fixed support condition (in addition to transfer of compression via shear stresses. The end plate was 25 mm thick, with a T-shaped piece cut into it for insertion of the specimen end. After the specimen was inserted into this cut segment of the plate, the gap between the metal plate and the stringer specimen was filled with a high-performance epoxy. The end condition created by end plates simulates the actual support conditions of PRSEUs stringer in service environment.

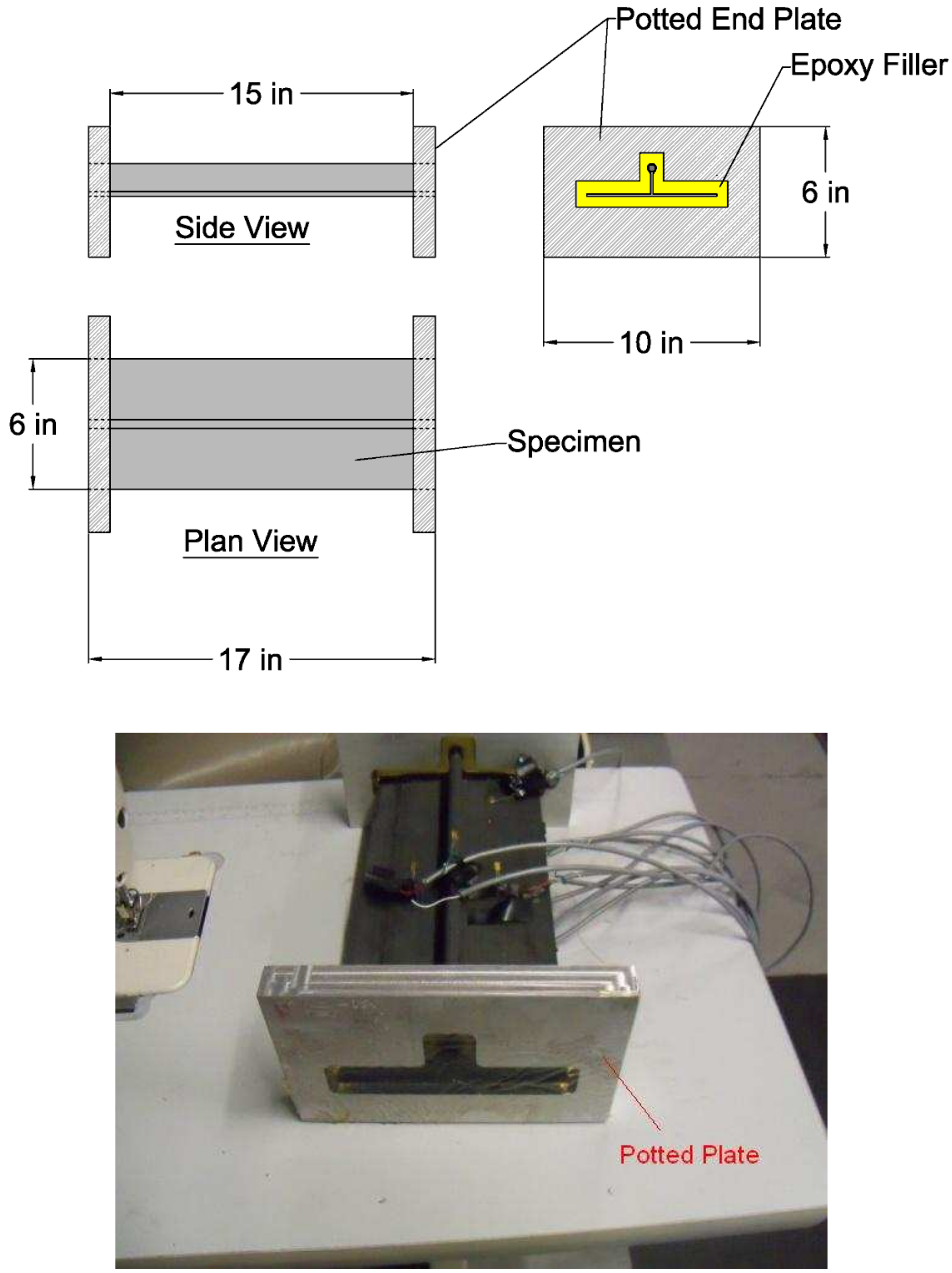

Figure 38. End (potted) used in compression tests on PRSEUS stringer specimens.

A servovalve-controlled hydraulic test system was used for performance of compression tests on stringer specimens (Figure 39). In order to simulate side conditions of a stringer within the structural system (where continuity of the panel produces lateral constraint), two side restraints were used to prevent edge buckling of the stringer specimens. Tests were performed in deflection-controlled mode, using a deflection rate of 0.1 mm/sec. Loads and deflections were monitored throughout compression tests.

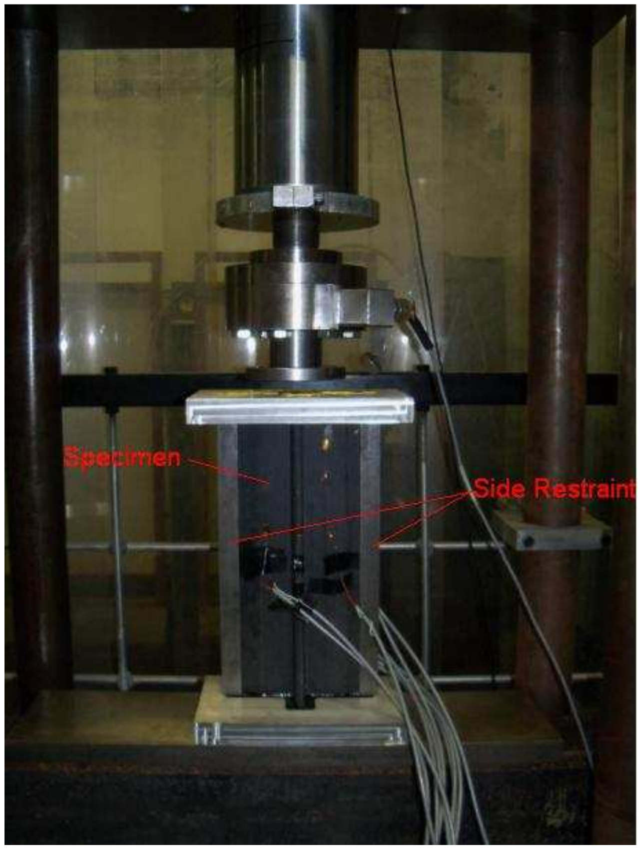

Figure 39. The setup for performance of compression tests.

Figure 40 presents average of compressive load-strain behavior of four stringer specimens fabricated and tested in this investigation. The average peak load obtained here (185 KN) is ~93% (with 95% level of confidence) of the corresponding peak value obtained in stringer specimens fabricated and tested by Boeing. The difference between our stringer specimen and that produced by Boeing, which can explain the difference between their compressive strengths, can be attributed to the diagonal stitching at web-skin joint in Boeing stringer yields improved structural integrity of the web-skin joint area.

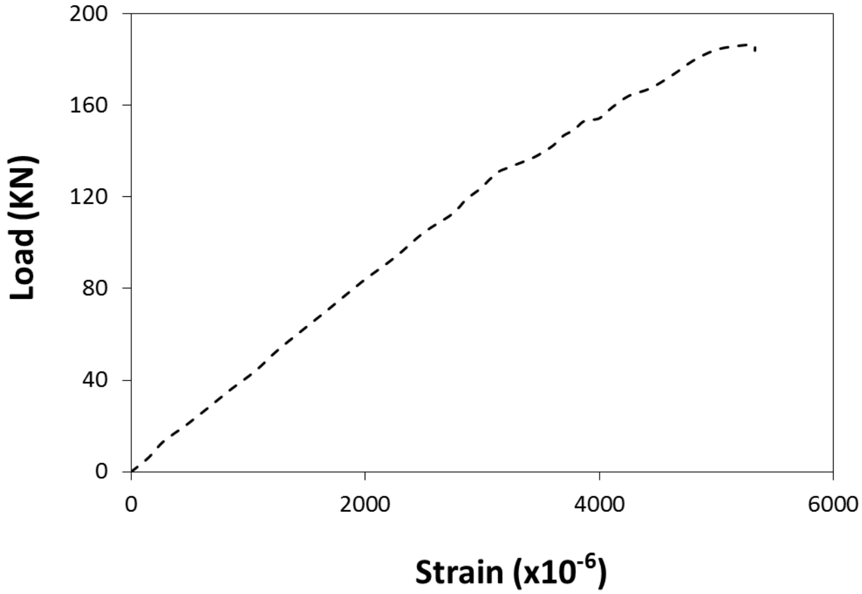

Figure 40. Compressive load-strain test results for stringer specimens.

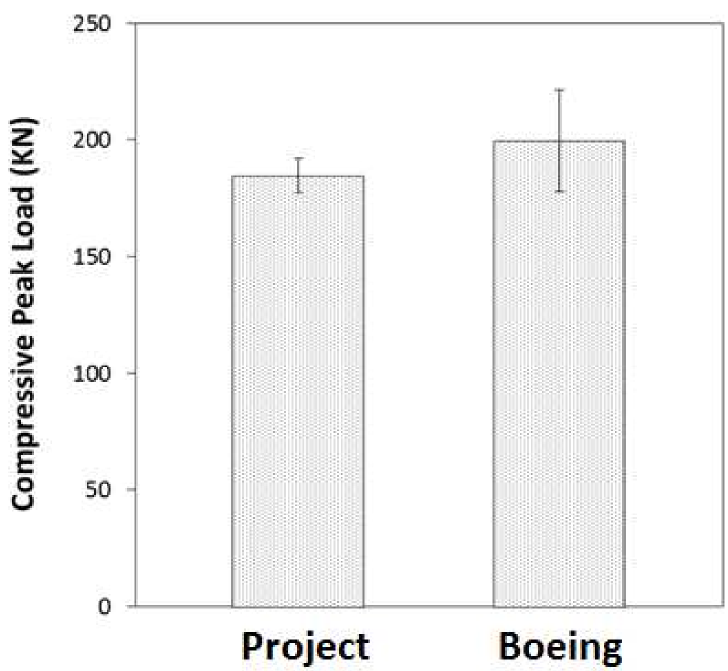

Figure 41. Average peak compressive loads reported by Boeing and obtained in the project.

Figure 42 shows the prestressed specimen after failure, which initiated by lateral buckling of the stringer web and pulturded rod, and was followed by failure of the multiaxial composite wrapping of the pultruded rod.

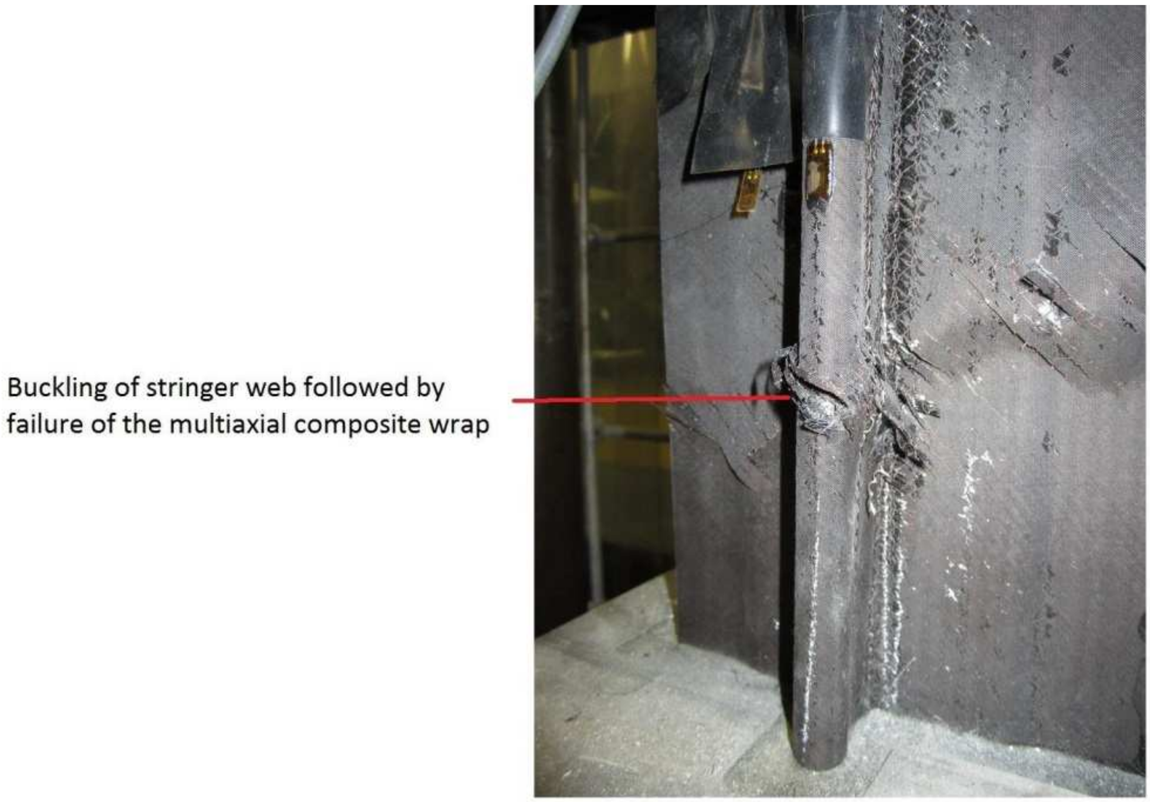

Figure 42. Prestressed PRSEUS stringer composite specimen after failure under compression.

3.4. Fabrication of the PRSEUS Frame Composite Structures

In order to evaluate the prestressing effect on scaled-up PRSEUS structures, the frame specimen comprising a frame, two stringers and skin will be fabricated and tested for evaluation of the prestressing effects. Because of the complexity of the frame structure, its fabrication process must be carefully established, and the final product must be checked against the minimum PRSEUS criteria.

3.4.1. PRSEUS Frame Composite Specimen

CAPRI process was employed for resin infusion of “frame” PRSEUS specimens. Assembly of the dry fiber preforms for processing the PRSEUS specimen starts with cutting and kitting of the plies of dry fabric that make up the skin, the stringer and the frame components. The 50-inch wide warp-knit multi-axial carbon fiber fabric was cut into individual details, and placed into kits. Three pieces of 3.4 x 20in, one piece of 20x20in and one piece of 32x20in fabric were used to assemble the PRSEUS frame specimen. The foam core was CNC machined with all the detail features required to support the frame plies (Figure 43a), carbon fiber rods and resin infusion processing. The fabric plies for the frame were cut net as described above including the keyhole features required at stringer intersections. The details were then joined by stitching in order to create a preform assembly. The completed preform assembly was then transferred to a rigid tool (outer mold) (Figure 43b). After attaching the vacuum (outlet) and resin line (inlet) to the preform, the epoxy resin was pre-heated and degassed for 15 minutes at 250^{o}F. Once the desired vacuum level was established, the resin was introduced into the flow media (which rests on the inner surface of the part) where it rapidly moved across the part surface before finally migrating through the thickness. Once the part was filled with resin at 250°F, the cure cycle was implemented at 350°F (Figure43c). Figure 44 shows the frame component after removal of the infusion vacuum bagging.

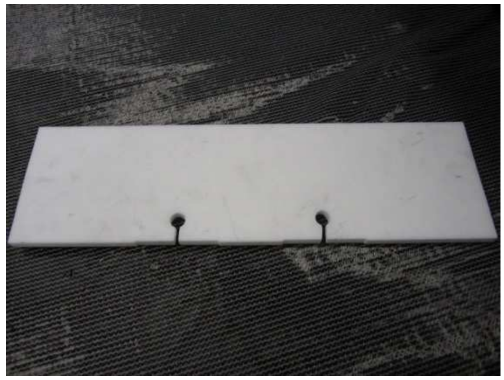

(a) CNC machined core foam

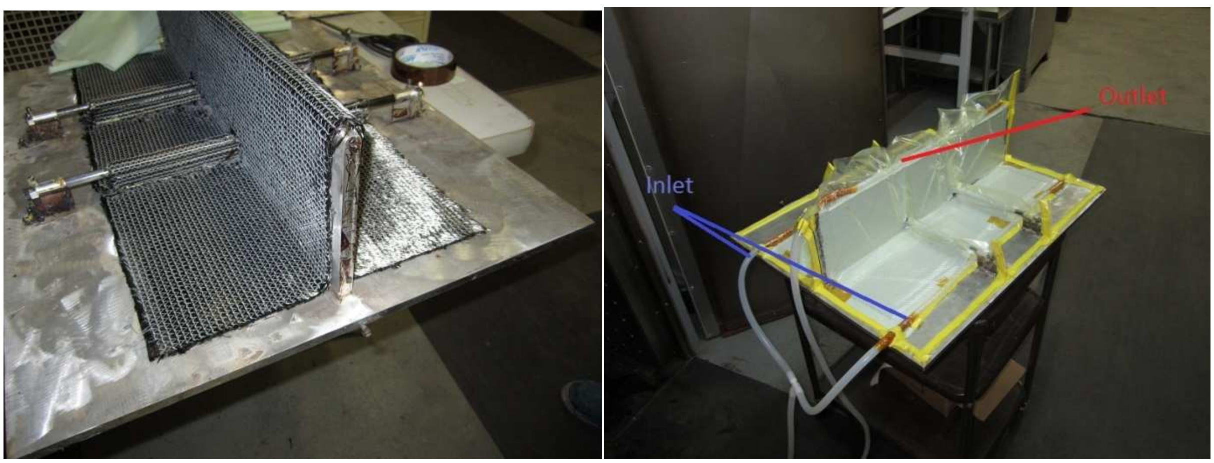

(b) Assembly of preform and tooling

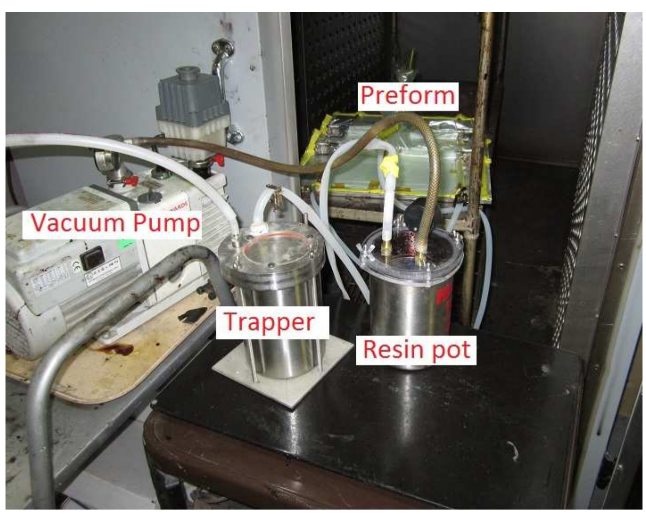

(c) Infusion and curing setup

Figure 43. PRSEUS frame fabrication steps.

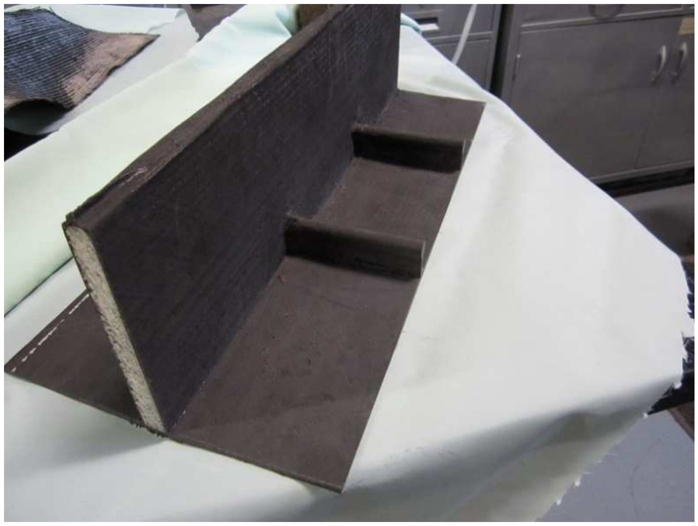

Figure 44. The PRSEUS "frame" specimen.

Alternative Infusion Configurations

Due to the greater complexity and relatively large size of the PRSEUS frame composite specimens, when compared with the PRSEUS stringer specimens fabricated and tested earlier, various options exist for positioning of the inlet (resin line) and outlet (vacuum line) for realizing thorough infusion of the fabric. Different inlet and outlet positioning configurations were evaluated, and the preferred configuration which produced a more thoroughly infused final product was identified. The three configurations evaluated are introduced in Figures 44a, 44c and 45e. The first configuration (Figure 45a) employs one inlet and one outlet at opposite ends, and is similar to that used successfully for infusion of PRSEUS stringer component. This configuration produced a partially infused specimen where the upper areas of the frame component were not infused (Figure 45b). The second configuration (Figure 45c) employed one inlet line along the top of the frame component, and two outline vacuum lines at opposite ends. This configuration also did not yield a fully infused end product; some dry areas were detected in skin areas occurring between the frame and stringers (Figure 44d). The third configuration

(Figure 45e) employed to inlets at opposite ends and one outlet along the top of the frame; this configuration yielded a fully infused specimen (Figure 45f).

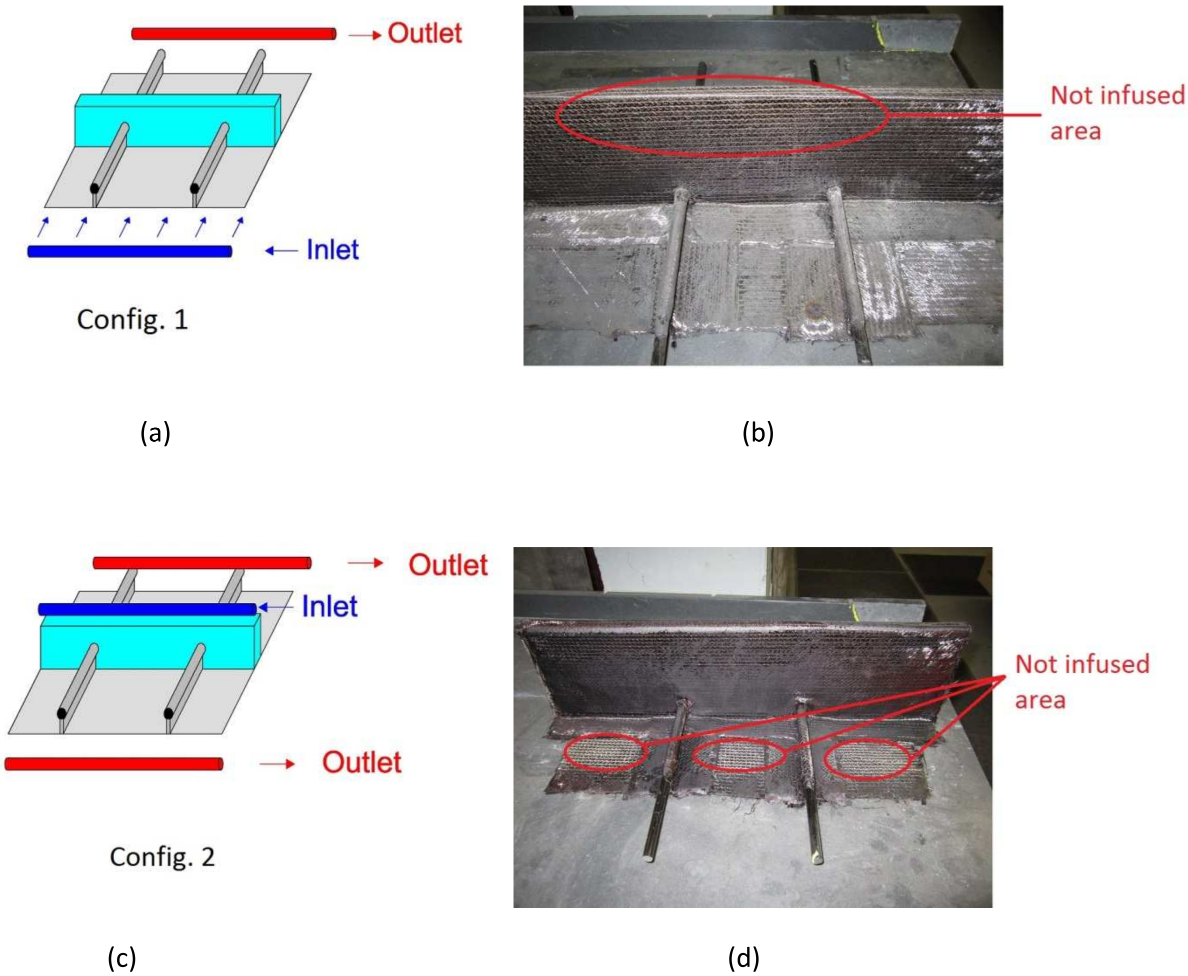

Figure 45. Different inlet/outlet positioniing configurations for resin infusion of “frame” stringer specimens.

Figure 45 (cont'd)

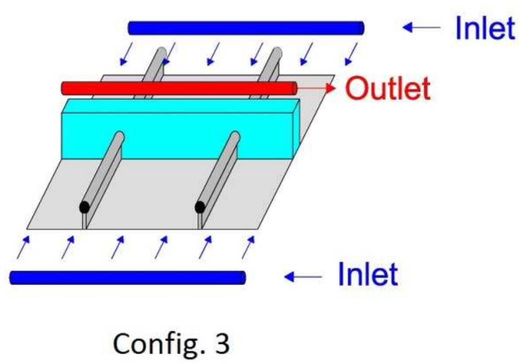

(e)

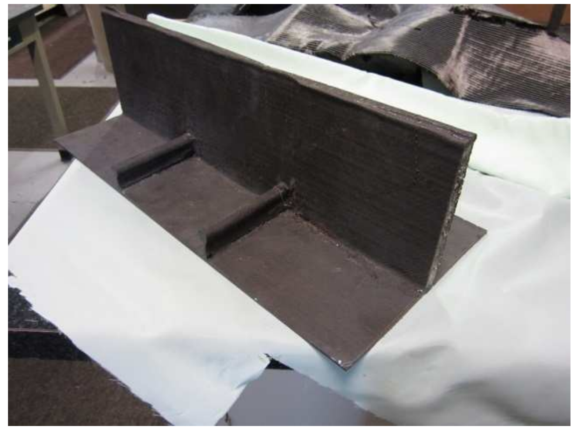

(f)

3.4.2. Compression Tests for Process Validating

Compression tests were performed in order to assess the quality of the processed specimens. To prepare the frame specimen for compression testing, two potted plates were used as end fixtures. They produce fixed support conditions, and also allow for load transfer to specimen via shear mechanism between the end grips and the PRSEUS frame (avoiding application of direct bearing pressure which could locally damage the composite). As shown in Figure 46, a steel plate 25 mm in thickness, with a T shaped piece cut out of it, constitutes the end fixture. The gap between the end plate cut-off and the specimen is filled by a high-performance epoxy to simulate the actual support condition of PRSEUS under service loads.

A PRSEUS frame specimen was subjected to compression loading to at a constant displacement rate of 0.1 mm/sec. During compression tests, the applied load and the crosshead displacement were recorded using a computer-based data acquisition system. As noted above, this test was performed in the direction of the frame (as performed by Boeing for their frame specimens) in order to compare the test results on our specimen with those reported by Boeing. Figure 47 shows the compression test setup.

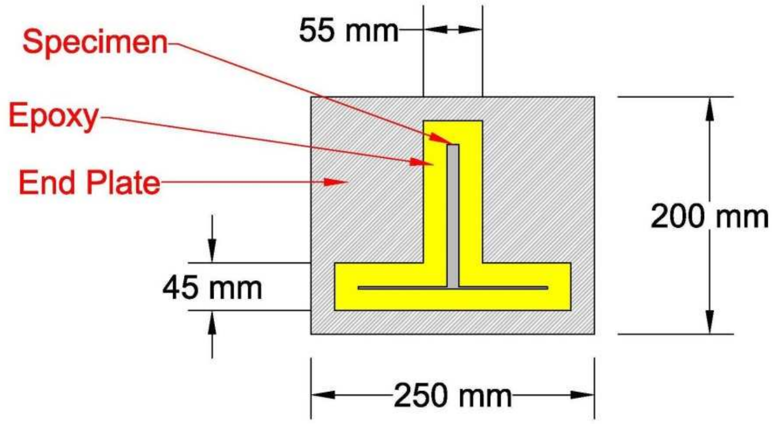

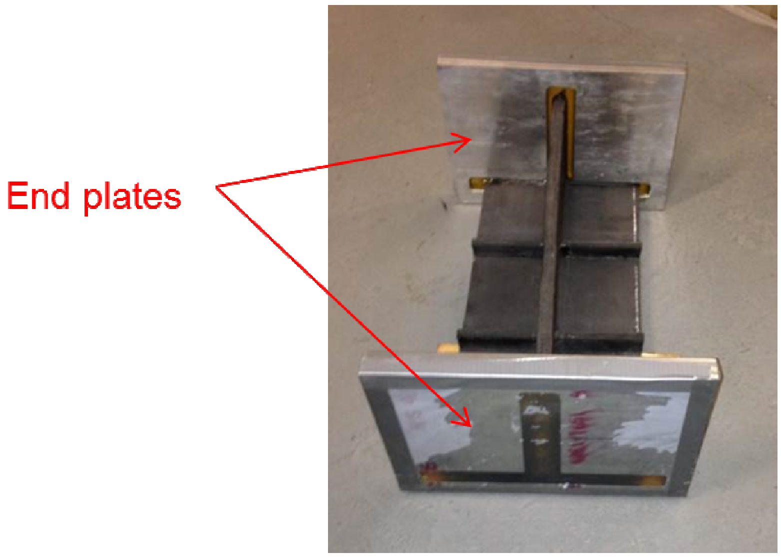

Figure 46. End fixtures (potted plates) used in compression tests on PRSEUS frame specimens.

Figure 47. Compression test setup.

The compression test result generated for the ‘frame’ specimen fabricated at MSU was compared against the compression test results generated by Boeing. Figure 48 presents a comparison of the average peak loads for Boeing and MSU PRSEUS frame specimens in compression tests. The peak load for our PRSEUS specimens was 335 KN, which is ~95% (based on one test) of that of the Boeing PRSEUS specimens (355 KN). The somewhat lower values achieved in our test can be attributed to the fact that diagonal stitching at the web-skin joint in the Boeing PRSEUS renders higher integrity (and structural contributions) at the critical web-skin joint area. The failure mechanism of the frame specimen involved this joint area. Failure started with buckling of the skin, which was followed by failure of the joint between the frame constituent of PRSEUS and the skin. The final step in failure of the frame PRSEUS specimen involved buckling of the frame constituent. The failure path and trend were the same as those reported by Boeing for their frame specimens subjected to compression tests. Figure 49 shows the failed frame specimen after compression test.

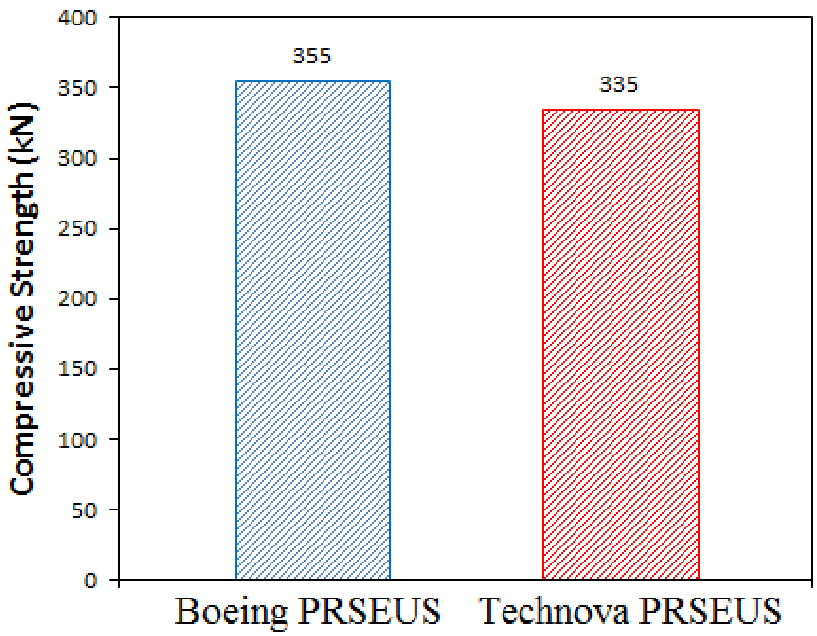

Figure 48. Compressive load-carrying capacities of Boeing versus technova PRSEUS frame specimens.

Figure 49. Failed PRSEUS frame specimen after compression test.

3.5. Physical Characteristics of the PRSEUS Specimens

In order to assess infusion conditions of PRSEUS "frame" specimens, the fiber volume fraction and the void content of the resulting composite were assessed, and were compared with those of the PRSEUS composite specimens produced by Boeing. The fiber volume fraction in composites was assessed through digestion of polymer matrix with an acid. Following ASTM D371 (Procedure A), which is used for carbon fiber epoxy composites, three specimens were cut from different areas of the PRSEUS composite "frame" (near inlet and outlet zones). The initial weight (M_i) and volume (V_i) of each specimen were measured; they were then placed in separate beakers containing 30 mL of 70% nitric acid. The beakers were heated on a hot plate (Figure 50) for six hours until all the epoxy portion of the specimens were digested by the acid. The matrix was considered fully digested when no trace of the reinforcement/matrix laminate could be detected. The content of the beaker was subsequently filtered into a pre-weighted (M_t) sintered glass filter under 28 KPa vacuum. Fibers were washed with distilled water three times, and then washed with acetone. This procedure was applied to each specimen separately. Subsequent drying of specimens was accomplished in an oven at 100^{o}C for 1 hour. The filter was then cooled down to room temperature, and the specimen and its holder were weighed.

Figure 50. digestion of the polymer matrix of specimens cut from PRSEUS composite frame.

The fiber volume fraction, Vr, was calculated using the following expression:

V_r= (M_f/M_i)xr_c/r_rx100

Where, r_c and r_r are the density of composite and reinforcement, respectively, M_i is initial weight of the specimen, and M_f is final weight of the specimen after digestion.

For Specimen #1, with measured values of M_i=0.8379 gr and M_f=0.5622 gr, using 1.405 and 1.28 gr/cm^3 as densities of fiber and composite, respectively, the above expression yields:

V_r=(0.5622/0.8379) x1.28/1.405 x100=61.1%

The void content, in percent, can be calculated as:

V_v=100-Vf-Vm

Where, V_m is the volume of matrix, in percent, which is calculated as:

$V_m=(M_i-M_f)/M_i$ xr_c/r_mx100

Where, r_m is density of matrix which is equal to 1.12 gr/cm^3 for the epoxy used in the project.

For specimen #1, the matrix volume fraction can be calculated as:

V_m=(0.8379-0.5622)/0.8379x1.28/1.12x100=37.6%

The void content is thus:

V_v=100-61.1-37.6=1.3%

Similar calculations were performed using the test data produced with other specimens cut from the PRSEUS composite frame. Table 5 summarizes the physical properties of all specimens. The average calculated fiber volume fraction was 62%, which is close to the 60% fiber volume fraction of the PRSEUS specimens fabricated by Boeing. The average void content for the three specimens was ~1.5%, which is within the range (<2%) measured for Boeing specimens. Figure 51 presents mircroscopic images of the specimens, which point at the thoroughness of resin infusion.

Table 5. Fiber volume fraction and void content test results for specimens cut from PRSEUS composite frame.

	M_i (gr)	M_f (gr)	V_r%	V_v%
Specimen #1	0.8379	0.5622	61.08	1.35
Specimen #2	0.7253	0.4898	61.40	1.56
Specimen #3	0.5501	0.3822	63.54	1.45
Average			62.01	1.45

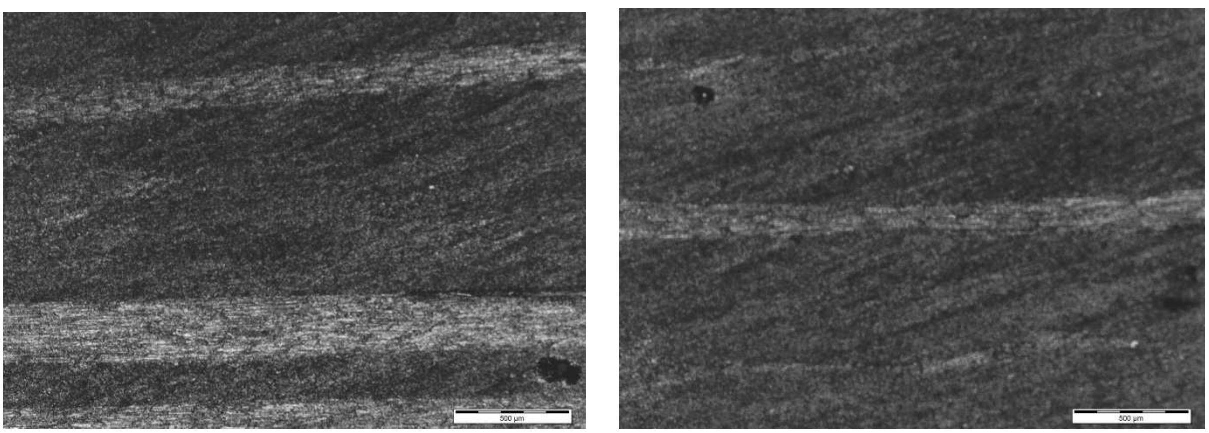

Figure 51. Microscopic images of PRSEUS composite specimens.

Chapter 4. Processing and Experimentation of Prestressed PRSEUS

4.1. Introduction

In rod stiffened composite structures, the uniaxially reinforced pultruded composite constituents (rods) provides a higher compressive strain capacity when compared with the quasi-istotrapic composite constituent of the structure. At failure, which is dominated by that of the multiaxial composite constituents (wrapping part and web of the stiffener), pultruded rods would thus remain under-utilized. The ultimate failure strain in compression of pultruded rods is 11,000 microstrain, while that for the multi-axial fiber reinforced composite is 4,500 microstrain. A comparison of stress-strain curves for rod stiffened stringer and the pultruded rod in Figure 52a demonstrates that failure of rod stiffened stringer (governed by the failure strain of the quasi-istotropic laminated/stitched composite) leaves a reserve strain capacity in the pultruded rod (i.e., the pultruded rod is under-utilized in this system). Prestressing (Figure 52b) is an attempt to produce a prestrain system in the structure which enables effective use of the pultruded rod as well as the multiaxial (stitched laminate) composite constituent towards achieving enhanced structural efficiency. In our approach to prestressing of PRSEUS composite structures, the prestressing force is transferred from the pultruded rod to the multiaxial composite via the interfacial bond. Figure 53 shows the distribution of the prestress system at a cross-section of the PRSEUS stringer.

The experimental work conducted in this investigation sought to verify gains in structural performance of rod stiffened stringer upon prestressing. The processing of pre-tensioned rod stiffened stringer was slightly modified according to different situations of prestressing mechanism. Since the pultruded rod is under compression it is vulnerable to buckling prior to the prestressing load transferring step. The pultruded rod is subjected to compression and it balances with tension in multiaxial composite. In order to prevent the pultruded rod against buckling the rod must be confined by an external mean. The processing was modified in order to confine the pultruded rod using the multiaxial composite. In the first step of processing the multiaxial composite was infused and cured while there was no bond between the rod and multiaxial composite. At the second step, prestressing step, the pre-compressed pultruded rod was bonded to the multiaxial composite using an adhesive agent.

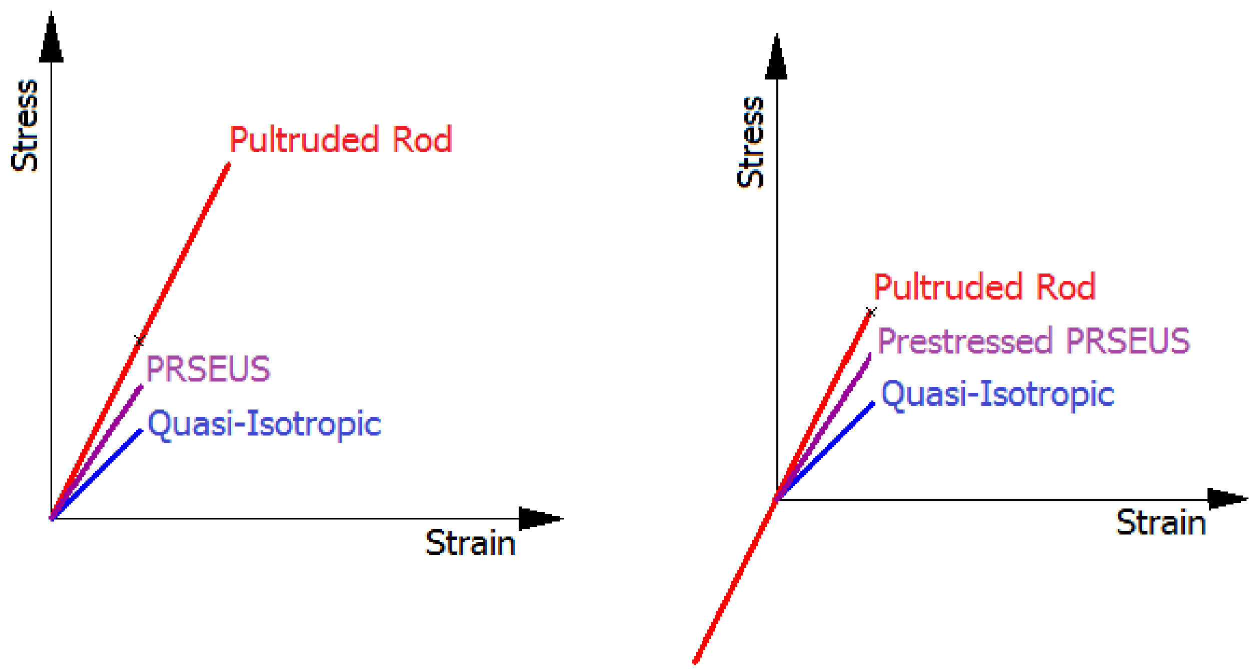

Figure 52. Typical compressive stress-strain behavior of PRSEUS, and its pultruded rod and quasi-isotropic (stitched) composite constituents.

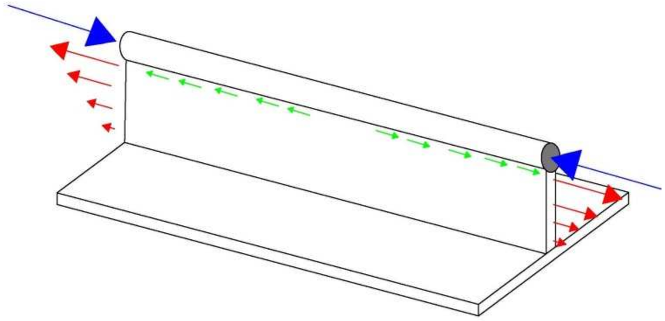

Figure 53. Distribution of prestress system on PRSEUS stringer.

4.2. Prestressing Transfer

The approach devised to pre-tensioning the composite structures relies upon pre-compression of pultruded carbon fiber composite rods. Upon release this pre-compression (after curing of the composite), the prestressing force is transferred to the structure via interfacial bond stresses. For pre-tensined specimen the prestressing load is transferred to the multiaxial composite after establishing the bond between the rod and the remainder of the structure using an adhesive agent. The end-anchorage used for application of either pre-compress or pre-tension to pultruded rods should be capable of transferring the required tensile prestress (prestrain) to the rod, and should also be reliable, lightweight, convenient and economical.

Due to the relatively small transverse (compressive) strength of pultruded (uniaxially reinforced) carbon fiber composite rods, the wedges and barrel anchors commonly used for tensioning metal rods cannot be applied directly to carbon fiber composite rods. Serrated wedges will tend to crush the matrix and eventually fracture the fibers before any significant tension could be developed in composite rods. Several methods are available to circumvent this problem; some protect CFRP rods with a metal sleeve or sheathing. In the approach used here (Figure 54), a thick metal tube with an internal diameter larger than that of the rod is used around the rod over a prescribed length. The gap between the tube and the rod is filled with a bonding agent. This agent could be a high-performance epoxy resin (considered here), or a molten alloy that is die-cast onto the composite rod before attaching the metal tube. In this approach, force is transferred to the pultruded rod via interfacial bond stresses developed between the rod and the bonding agent. For this purpose, the tube is gripped with matching wedges, or it can be threaded (on outside surface) and anchored using a nut..The pultruded rod is threaded via sandblasting (Figure 55), with an indentation depth of 2 mm (spaced at 5 mm). It is worth mentioning that temporary end fixtures are required at both ends of the pultruded rod. The modified surface of rods produces mechanical interlocking effects which benefit stress transfer via the epoxy filler. The tube used here was made of cold-drawn steel; its diameter and wall thickness were 25 mm and 4 mm, respectively, producing a 3 mm gap between the tube and the pultruded rod (to be filled by high-performance epoxy). The epoxy resin used here suits room-temperature curing, and has a relatively low viscosity for convenient and thorough filling of the gap between the pultruded rod and the steel tube. In order to improve interfacial bonding of epoxy to tube, the inner surface of the metal tube was also threaded.

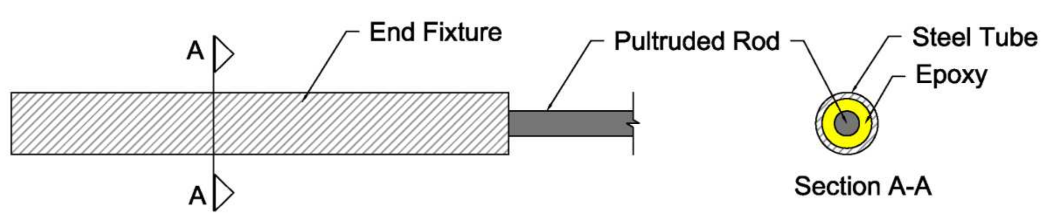

Figure 54. Configuration of the anchorage system for pre-compressioning the pultruded composite rods.

The bond lengths between pultruded rod and end fixture considered in experiments were 100, 200 and 300 mm. The 9.4 mm (0.374 in) diameter pultruded rods used in the experimental program were supplied by AcpUSA. The elastic modulus and tensile strength of these rods were 140 MPa and 2.3 GPa, respectively. The high-performance epoxy used as the bonding agent was MarineEpoxy 300. The two components of this high-performance epoxy were preheated to 60^{o}C for 15 minutes, mixed in equal volumes, and degassed for 15 minutes under vacuum. The resin was injected through a hole at the end of the sleeve (tube) after the rod was aligned vertically and centered inside the tube (with its lower end blocked by a rubber stopper). Due to the small gap between the rod and tube, the tooling used in this step (Figure 56) was designed to assure that the rod is centered parallel to tube. The metal tube was filled with epoxy resin, and then kept stationary for 48 hours at room temperature to cure the epoxy. A similar procedure was followed for application of the fixture to the opposite end of the pultruded rod.

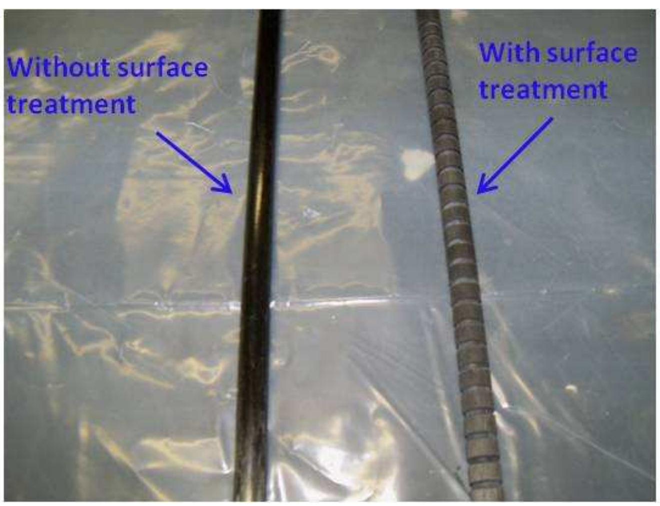

Figure 55. Rods without (left) and with surface treatment.

Figure 56. Resin-filled tube encasing pultruded rod.

All specimens were tested in tension to failure using a servovalve-controlled hydraulic test system at a constant displacement rate of 0.1 mm/sec. For the performance of tension tests, the end-anchorages were placed within modified grips (Figure 57) which reproduced the end conditions of pultruded rods during prestressing of composite structures. During tension tests, the applied load and the crosshead displacement were recorded using a computer-based data acquisition system. The strain developed in the pultruded composite rod was also recorded using a strain gage attached to the mid-height of the rod.

Figure 57. Tension test setup: end grip (left), and overall view (right).

All specimens failed by pullout of the pultruded rods from the end-fixture. Interfacial bond strength thus determined the failure load (in lieu of the pultruded rod rupture strength). The mean value of interfacial bond strength to modified (threaded) pultruded rods, for the bond lengths considered here (100, 200 and 300 mm), was 9.38 MPa. The bond strength test results for specimens without and with surface modification (threading) are compared in Figure 58. The average bond strength of epoxy to pultruded rods is observed to increase by 40%, with 95% level of confidence, (from 6.59 to 9.38 MPa) upon modification (threading) of rod surfaces.

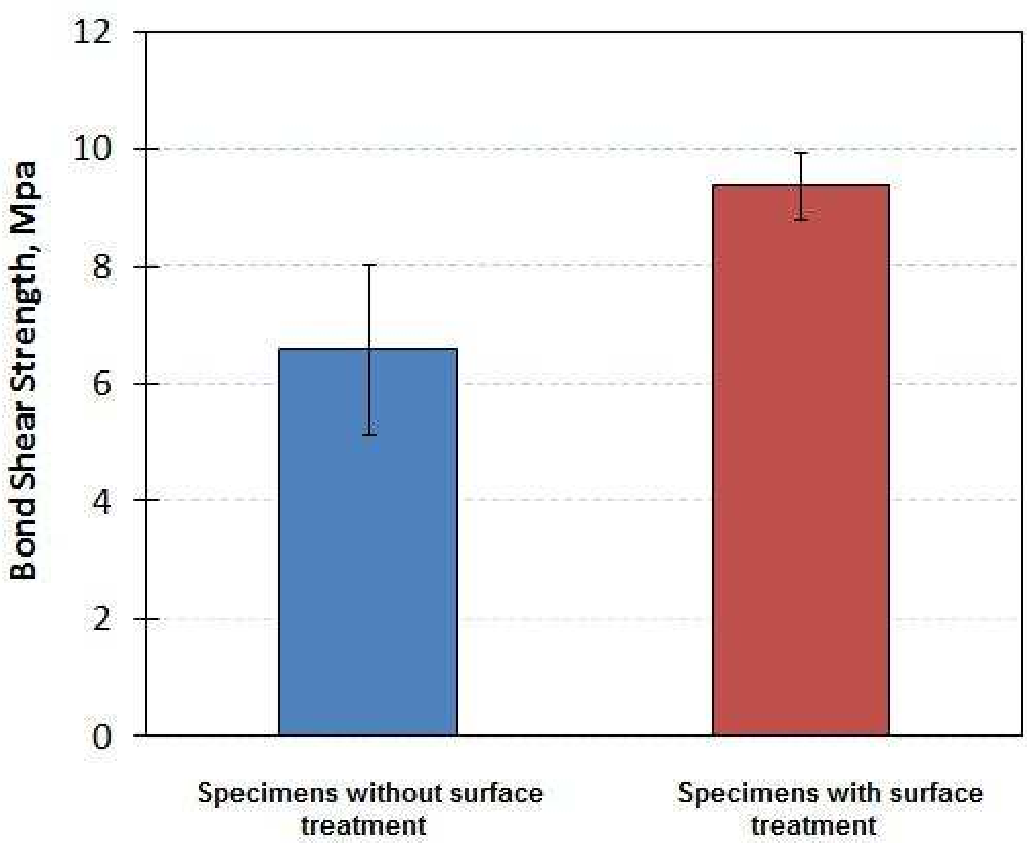

Figure 58. Average of Bond shear strengths of high-performance epoxy to pultruded rods without and with surface treatment (threading).

Figure 59 compares the peak tensile strains developed in pultruded rods (with unmodified and modified surfaces) during pullout tests from end fixture with different embedment lengths.

Increased bond lengths as well as surface modification of rods are observed to produce higher peak tensile (pre-)strains in pultruded rods. The average peak strain in modified specimens with 200 mm bond length was 6,240 microstrain, which was ~40% higher than the peak strain of 4,427 microstrain developed in unmodified rod with similar bond lengths. The average peak strain in modified rods with 300 mm bond length was also ~30% higher when compared with unmodified rods of similar bond length (10,323 versus 7,302 microstrain). Modified rods with 300 mm bond length thus provides peak prestrains (10,323 microstrain).

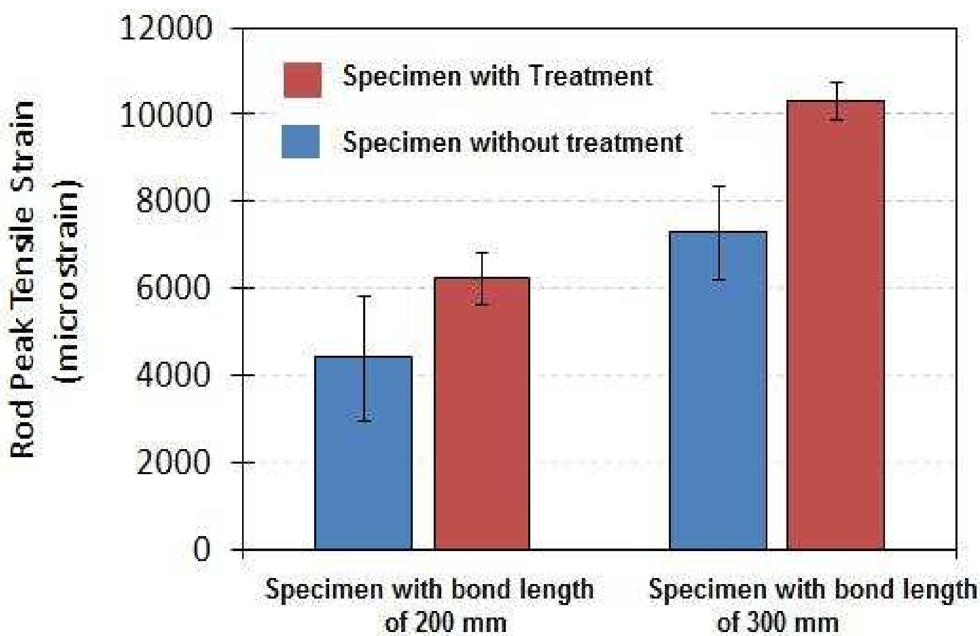

Figure 59. Average of peak tensile strains developed in treated and untreated pultrued rods of different bond lengths.

The 300 mm long fixtures with modified surfaces were used for the purpose of prestressing as they provide sufficient capacity to apply a prestraing of 8,000 microstrain.

4.3. Evaluation of the Bond Strength Between Pultruded Rod and Multiaxial Fiber Reinforced Composite

Prestressing of composite structures is accomplished in our approach by precompressioning of the pultruded rod, followed by curing of the multiaxial composite, and finally release of the rod precompression for prestressing the composite. Upon release of the rod precompression, the prestressing force is transferred to the multiaxial composite via the bond developed between the putruded rod and the multiaxial composite during curing of the composite. An experimental study was conducted to ensure that the bond strength is adequate for transfer of the prestressing force from pultruded rod to multiaxial fiber composite structure.

Rod pull-out tests were conducted which yield bond strength as a basis to determine the required development length, Lc, for full transfer of the prestressing force from the pretensioned rod to the multiaxial fiber composite (Figure 60).

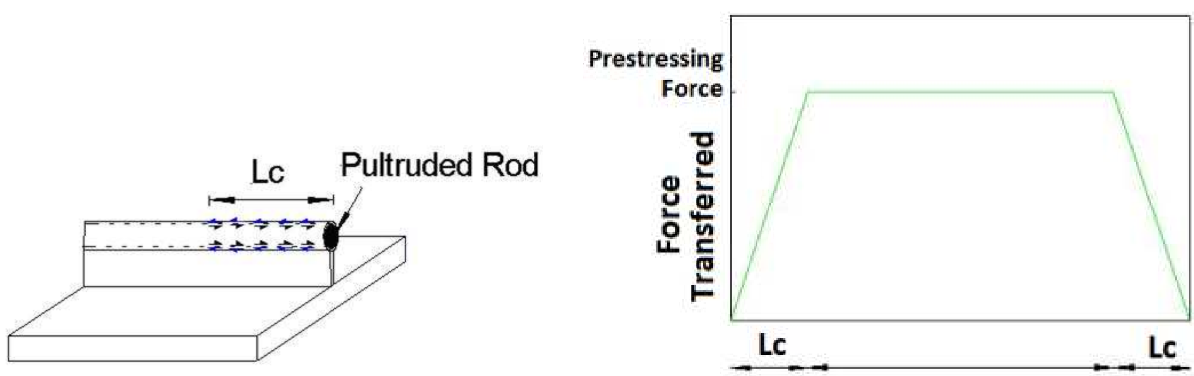

Figure 60. Load transfer mechanism at the pultruded rod-multiaxial fiber composite interface.

The pull-out test specimen comprised a pultruded rod sandwiched between two stacks of multi-axial fabric, which were stitched together (using two rows of stitching) and then infused with resin using the CAPRI process. This pull-out test specimen is shown on the left hand side of Figure 61. After resin infusion and curing, the test fixture shown on the right hand side of Figure

61 was prepared for gripping the pultruded rod during pull-out. This fixture is a steel tube encasing the pultruded rod, with a high-performance epoxy (AeroMarine) filling the gap and bonding the pultruded rod to the steel tube.

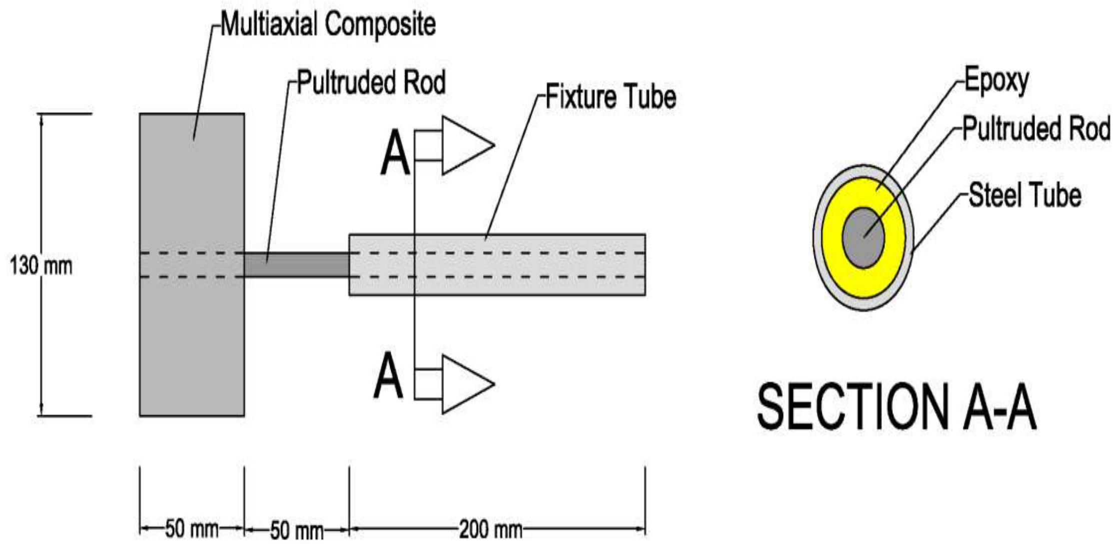

Figure 61. Schematic configuration of Pull-out specimens.

Figure 62 presents the pictures taken during processing of the pull-out test specimens. Figure 63a shows the pultruded rod sandwiched between two stacks of multi-axial fabrics stitched together and placed on the one sided mold. Figure 63b shows the vacuum bagging mounted on the dry perform. Figure 63c shows the specimen during resin infusion (after which curing was accomplished at 350^{o}F over 2 hours). In order to perform the pull-out test, the fixture at the free end of the pulturuded rod was mounted. As noted earlier, this fixture consists of a steel tube filled with high-performance epoxy. The steel tube length is 250 mm; it has an outer diameter of 25 mm and a wall thickness of 5 mm. In order to enhance the bonding between filled epoxy and the steel tube, the inner surface of the tube was threaded. Figure 64 shows the free end of the pultruded rod placed inside the steel tube for filling with epoxy. Pull-out tests were performed in displacement-controlled mode at a rate of 0.1 mm/sec (Figure 64).

(a) Dry perform (b) Specimen under vacuum bag (c) Specimen during infusion

Figure 62. Processing stages of pull-out test specimen.

Figure 63. Preparation of the pullout test fixture mounted at the free end of the pultruded rod.

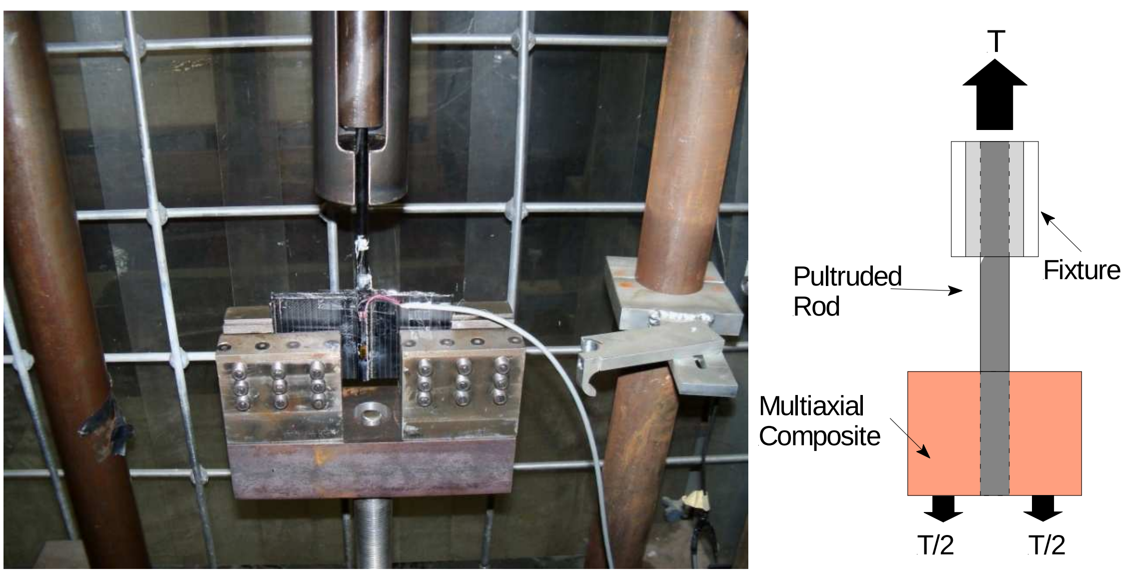

Figure 64. Pullout test setup.

The pullout load-deflection test results (Figure 65) pointed at a linear elastic behavior up to sudden failure by pullout of the putruded rod, which was marked by a sharp drop in pullout load followed by a more gradual decrease in load with increasing pullout deflection. After completion of the pullout process (Figure 66), the multiaxial fiber composite seemed to remain intact, suggesting that failure was predominantly by interfacial debonding and frictional pullout. The average (peak) shear bond strength in pullout tests was 26.8 MPa, and the peak strain reached in pultruded rod during pullout was 9,420 microstrain. These results indicate that a 75 mm bond length is adequate for reaching the teargeted tensile prestrain of 8,000 microstrain in pultruded rods. An evaluation of experimental results based on fracture mechanics principles [62] yielded an interface fracture toughness of 37 J/m^2, and a peak debond stress value of 33.2 MPa.

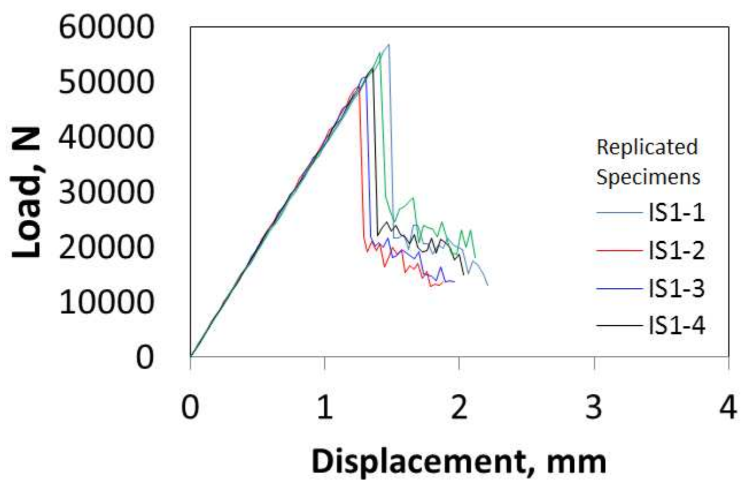

Figure 65. Pullout load-displacement curves .

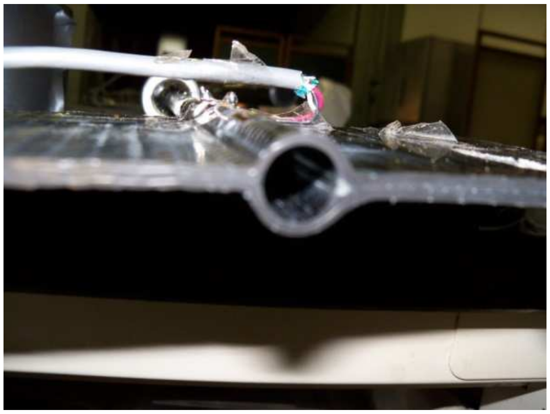

Figure 66. Multiaxial composite after pullout of pultruded rod.

Experiments were conducted for evaluating the bond strength between pultruded carbon fiber composite rods and the multiaxial fiber reinforced composite used in PRSEUS structural systems when low-creep adhesive agent is employed. Processing of the multiaxial composite started with cutting and kitting of the plies of dry fabric. Two 10 x 5 in. pieces were cut, and then joined by stitching in order to create a preform assembly. In order to make a hole for later insertion of the pultruded rod, a Teflon rod was sandwiched between the multiaxial fabrics; two rows of stitching were used to stitch the stacks together. The thread used for stitching was Kevlar Tex69 supplied by The Thread Exchange. The procedure for processing followed that of PRSEUS, as explained in previous reports. Figure 67 shows the multiaxial composite after resin infusion of fabric, curing, and removal of the Teflon rod.

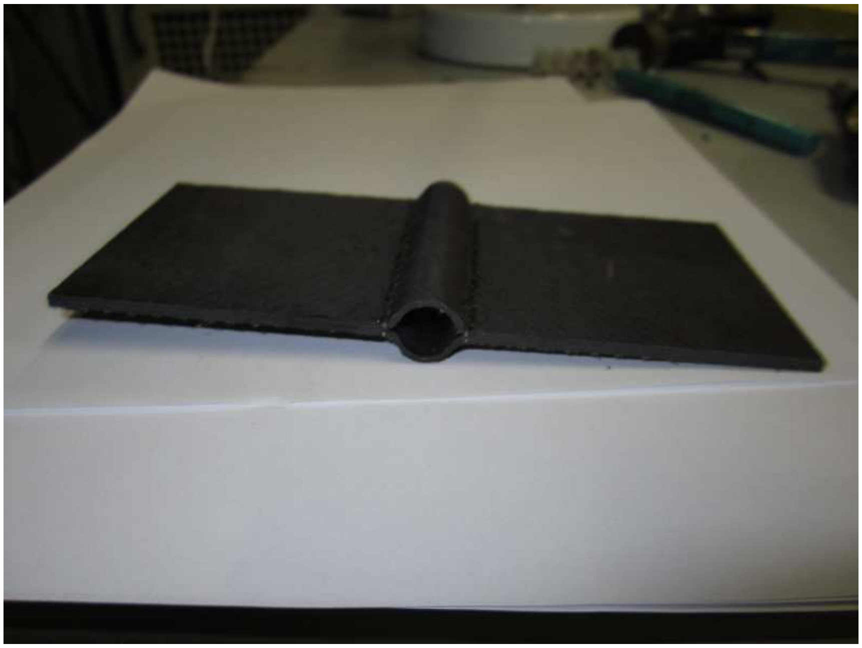

Figure 67. The multiaxial composite after removal of the teflon rod.

The pultruded carbon fiber/epoxy rod wrapped with the low-creep adhesive film Figure 68 was inserted into the hole of the multiaxial composite, and the adhesive film was cured in an oven at the recommended temperature of 300^{o}F over 2 hours in order to establish the bond.

Figure 68. Pultruded rod wrapped with the low-creep adhesive film

Experimental Results

The load-deflection curves produced in pullout tests are shown in Figure 69. The pullout load is observed to increase linearly with displacement; failure by pullout is sudden, causing a sudden drop in load, that is followed by increasing displacement (i.e., further pullout) at a relatively constant load level (indicating frictional pullout after bond failure).Figure 70 shows the multiaxial composite component of the pullout test specimen after complete pullout of the pultruded rod. Failure seems to occur at the interface, leaving the composite specimen intact.

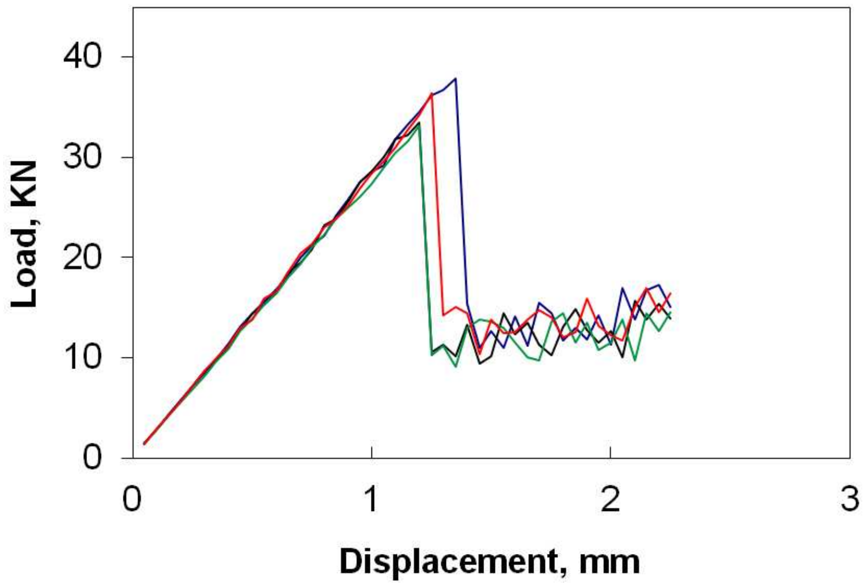

Figure 69. Pullout load-displacement curves.

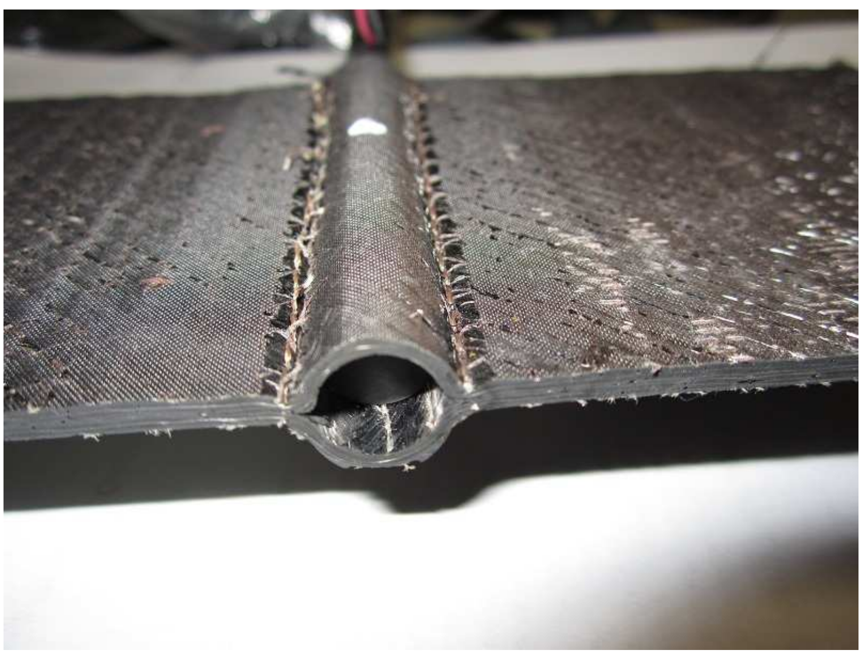

Figure 70. The multiaxial composite component of the pullout test specimen after complete pullout of the pultruded rod.

Pullout test results are summarized in Table 6. The pullout (debonding) load is used to calculate the average bond strength as $P/\pi.D.L$ (where P is the maximum load, and L and D are the bonded length of rod and its diameter, respectively). For specimen PADH-1, for example, τ_{ave}=38900/(πx0.0094x0.05)=26.4 MPa. The average bond strength was measured 25.1 MPa. Considering the targeted prestrain of 8000x 10^{-6} in pultruded rod, the prestressing foce is calculated as $P= E_{rod}.\varepsilon_{rod}.A_{rod}$= 140 GPa x 8000 x$10^{-6}$ x 69 mm^2= 77,280 N. The bond length required for transfer of this prestressing force from the pultruded rod to the multiaxial composite can thus be calculated as:

$L= P/(\tau_{ave}\pi.D)$=77280/(25.1x π x9.4mm)= 104 mm

The above calculation indicates that a 'development' length of 104 mm is required for transfer of the full prestressing force from the pultruded rod to the multiaxial composite.

Table 6. Pullout test results.

Specimen	Pullout Load, KN	Average bond Strength, τ_{ave} , MPa
PADH-1	38.90	26.4
PADH-2	35.96	24.4
PADH-3	35.84	24.3
PADH-4	37.39	25.3

Pullout tests were reported earlier where the pultruded rod was bonded to the multiaxial composite via infusion and curing of the epoxy resin (during processing of the multiaxial composite – as is done in non-prestressed PRSEUS production). The average interfacial bond strength in these specimens was 26.8 MPa, which is comparable with the bond strength of 25.1 MPa obtained here with the low-creep adhesive film. Figure 71 compares the mean values and variations of the bond strength obtained via epoxy resin infusion versus that achieved with low-creep adhesive film.

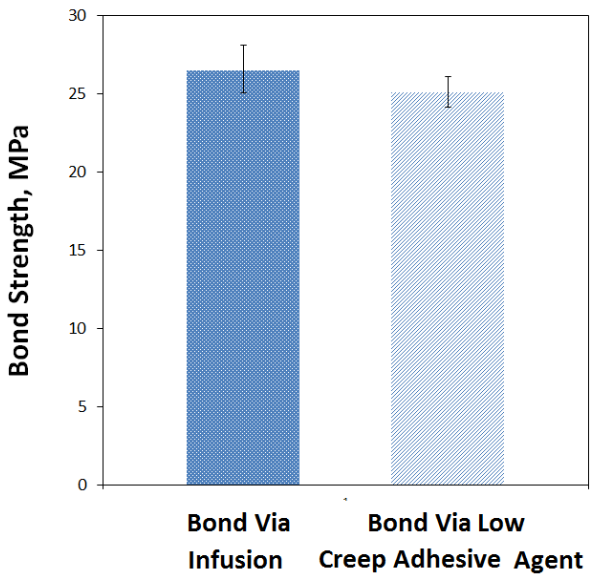

Figure 71. Interfacial bond strengths produced via conventional resin infusion versus use of low-creep adhesive film.

4.4. Pretensioned PRSEUS Stringer

4.4.1 Adjustments in Processing

As mentioned earlier, processing of the pretensioned rod-stiffened stringers was performed in two steps: (i) processing of multiaxial composite, and (ii) prestressing. In the first step, processing is similar to that of non-prestressed rod-stiffened stringer except that the bond between the rod and the multiaxial composite constituent of the specimen is prevented by a Teflon tube covering the rod during resin infusion. Once the infusion and curing cycles are completed, the pultruded rod is withdrawn from the stringer specimen, and prepared for the subsequent prestressing step. Figure 67 shows the stringer component after infusion vacuum bagging and removal of the pultuded rod.

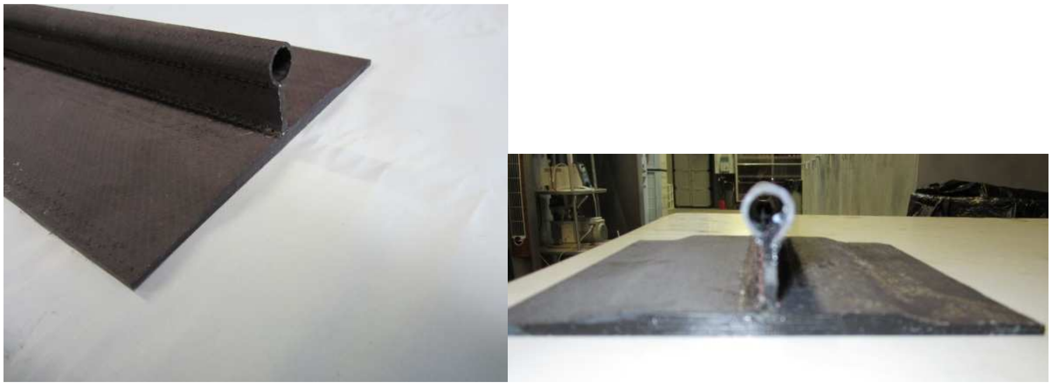

Figure 72. Stinger after removal of the pultruded rod.

After resin infusion and curing of the multiaxial fabric constituent of PRSEUS, the pultruded rod was removed from the specimen, and the Teflon tube surrounding the rod was taken off. The rod was then wrapped with a high-performance epoxy adhesive film. The adhesive film would help establish onaerospace-quality bonds between the pultruded rod and the multiaxial fibric constituent of the rod stiffened stringer. Figure 68 shows the pultruded rod wrapped with the adhesive film.

Figure 73. Pultruded rod wrapped with epoxy adhesive film.

4.4.2. Prestressing tooling

In earlier efforts, different prestressing toolings were designed and employed. None of them could be employed to prestress large specimens which had a frame component intersecting the stringers. Also, the heavy weight of the toolings employed earlier was a major disadvantage. Design of a light-weight and efficient prestressing tooling was an important objective of the project. A key factor contributing to the efficiency of the new prestressing tooling is the direct balancing of the pre-compression in prestressing elements (pultruded rods) with the pre-tension in adjacent structural elements (which are the prestressing tooling prior to curing and the multiaxial composite after curing); this balancing of forces developed in adjacent elements effectively restrains the prestressing element against buckling, as explained in the following.

Figure 74a shows self-equilibrating compressive forces developed in adjacent elements. We analyzed the effect of the prestressing force F on the buckling load of the prestressed element (P = P_p+P_s in Figure 74b, where P_p and P_s are the compressive forces developed in the prestressing and structural elements, respectively). The forces applied to the buckled prestressed panel shown in Figure 74c include the axial force P_p+F at ends, and the transverse force q_r. Our theoretical analysis confirmed that the resistance against buckling provided by this transverse force compensates for the effect of the end compressive force F. Hence, prestressing does not lower the buckling resistance of the system. In Figure 74c, the prestressing element is subjected to the axial force $P+F$ at its ends, and also to the transverse distributed force $q_r = F/\rho$ applied by the structural element due to the curvature $1/\rho=w''(x)$ as the system deflects. The differential equation for the deflection $w(x)$ of the prestressing element is:

$$(EIw'')'' + (P_p+F)w'' = q$$

For small curvatures, $q = -q_r = Fw''$ (negative curvature makes q negative). Substitution into the preceding differential equation yields:

$$(EIw'')'' + P_p w'' = 0$$

which is the same as the differential equation for $F = 0$. Hence, application of the pre-compression force F on the prestressing element does not cause its buckling. This analysis is contingent upon the prestressing elements being placed in contact with the structural elements without free play.

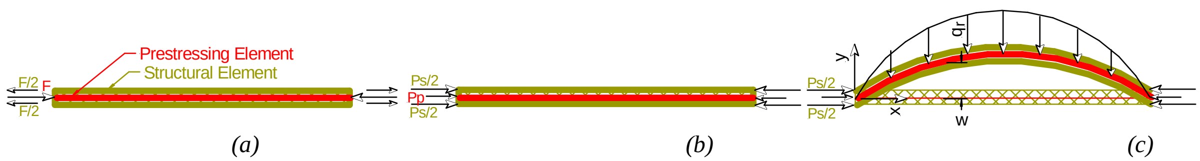

Figure 74. Buckling of the prestressed panels.

The above concept, which requires contacting pre-compressed and pre-tensioned elements, was used to develop a new prestressing tooling (Figure 75). The tooling is small and lightweight; it is installed (gripped onto the skin) only at the part ends, and applied compression to pultruded rods using a bolt. The tensile force transferred to skin via the grip is balanced by the compressive force applied to pultruded rods by the bolt. The tooling weight as a fraction of the part weight decreases as the part size grows. In the case of the frame PRSEUS specimen shown in Figure 3, the weight of the tooling installed at each end of the specimen is 3 lb.

(a) Individual tooling

(b) Prestressing of the frame prseus specimen with the new tooling

Figure 75. The prestressing tooling, and its application towards prestressing of the frame PRSEUS specimen.

The pultruded rod was subjected to pre-compression using the light-weight prestressing tooling described earlier. The pre-compression load is transferred from the tooling to the fixture tube via bearing action, and then transferred to the wall of the end fixture. The load is finally transferred to the pultruded rod via interfacial shear between the epoxy filled end fixture and the rod. The pre-compression load is marked by red arrow in Figure 76; it is balanced by the pre-tension forced developed in the skin (blue arrows in Figure 76). Pre-tension is transferred to skin via grips which are part of the prestressing tooling. These grips are similar to those used in tension tests. The prestressing process is monitored using strain gages which are mounted on the pultruded rod and the multiaxial fiber composite constituent of PRSEUS.

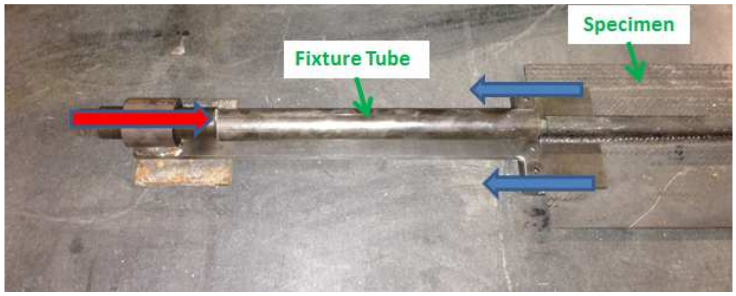

Figure 76. The lightweight prestressing tooling, and its mechanism of action.

The rod was pre-compressed by tightening contracting nuts until the rod strain reached 6200 micro-strain. With this pre-strain retained, the whole system was placed in an oven, and subjected to the curing cycle of the epoxy adhesive films. The whole system was retained at 300^{o}F for 1 hour in order to develop bond between the pultruded rod and the multiaxial composite constituent of PRSEUS. After curing of the adhesive film, the prestressing force was released for transfer to the multiaxial composite. The pre-compression in rod induces a balancing pre-tension in multiaxial composite, which is largest near the wrapping area in the stiffener web. Figure 77 shows the prestressing and bonding step in preparation of the prestressed PRSEUS specimen.

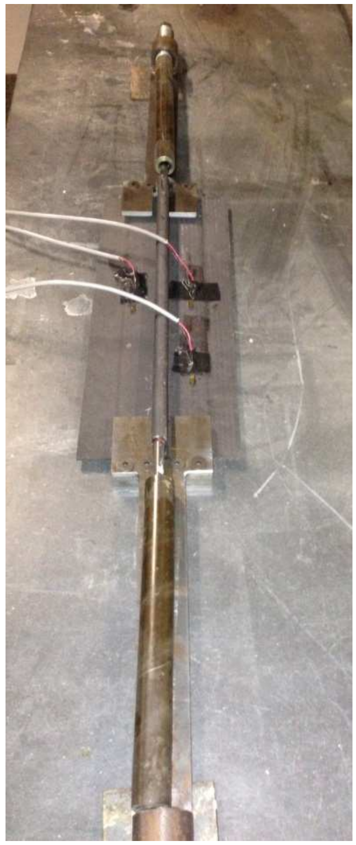

Figure 77. The prestressing and bonding step in preparation of the prestressed stringer specimen.

The initial pre-strain developed in the pultruded rod was -8000 micro-strain (just prior to release of prestressing). After the prestressing force was released, the pre-strain in rod (outside of the specimen) was lowered to 0, and the pre-strain at specimen reached 2050 micro-strain (which corresponds to 100% of the targeted prestressing level).

4.4.3. Experimental Results

Prestressed specimens were prepared for compression testing as explained in Chapter 3. The test setup and loading conditions were similar to those used with non-prestressed specimens. During compression tests, the applied load and the crosshead displacement were recorded continuously using a computer-based data acquisition system. The strains developed in the PRSEUS stringer specimen at its mid-height was also recorded using strain gages attached to the skin and the stringer web.

The measured values of ultimate compressive loads of prestressed and non-prestressed PRSEUS stringer subcomponents are compared in Figure 78. Prestressing enhanced the (buckling) failure load by (32   12)% (with 95% level of confidence). The mean value of peak loads for the non-prestressed PRSEUS stringer subcomponent was 185 KN, which was increased to 243 KN with application of the targeted prestress level (without any weight penalty). The failure modes observed in recent tests were similar to those observed earlier, involving lateral buckling of the stringer web and pultruded rod followed by failure of the multiaxial composite wrapping around the pultruded rod.

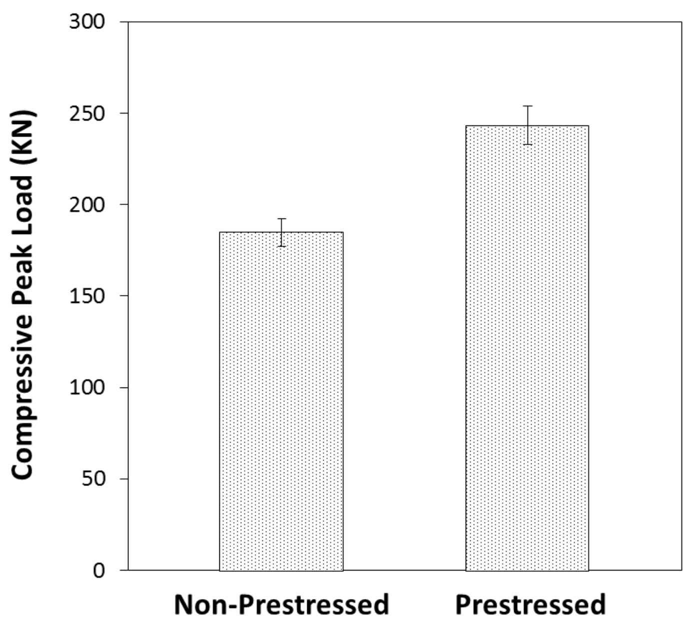

Figure 78. Failure compressive loads of non-prestressed and prestressed PRSEUS stringer subcomponents.

The initial compressive prestrain developed in the pultruded rod was -8000 microstrain (which was balanced against the tensile force developed in the tooling). After release of the prestressing force to the multiaxial composite constituent of the rod stiffened stringer, a tensile prestrain of 2,050 (corresponding to 100% of the targeted level) was developed in the stiffener web (multiaxial composite).

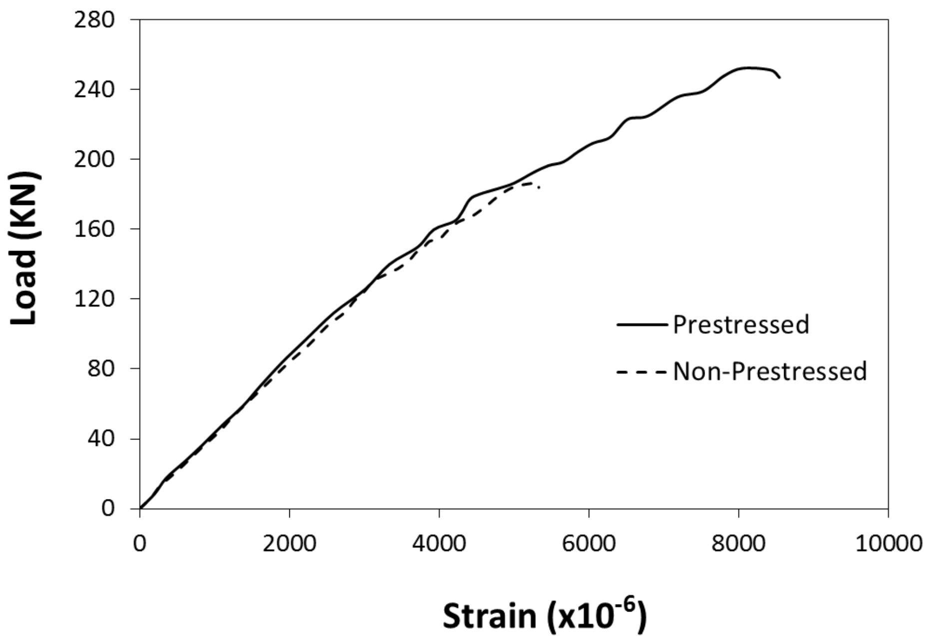

Figure 79. Compressive load versus strain for prestressed and non-prestressed PRSEUS stringer specimens.

4.4.4. Statistical Analysis of Test Results

Table 7 shows the peak compressive loads obtained in tests on non-prestressed and prestressed specimens. The normalized strength (strength in each test divided by mean value) is also presented because the variations of the test data for different groups of specimens need to be compared considering the mean value for each group of data.

Table 7. Summary of experimental results

Specimen	Compressive Strength (KN)		Normalized Strength (Strength/Mean)	
	Non-Prestressed	Prestressed		
1	194	231	1.05	0.95
2	187	248	1.01	1.02
3	181	239	0.98	0.98
4	177	255	0.96	1.05

Statistical analyses of the compression test data were performed using the SYSTAT software [63]. Figure 80 shows the distribution of test results for prestressed and non-prestressed apecimens. Comparison of mean values of the test results was performed using the t-test procedure, with the results summarized in Table 8. Statistical analysis showed that the mean of value pertaining to prestressed specimens exceeds that of non-prestressed specimens at 0.05 level of significance. Table 8 shows the analysis results for prestressed and non-prestressed specimens.

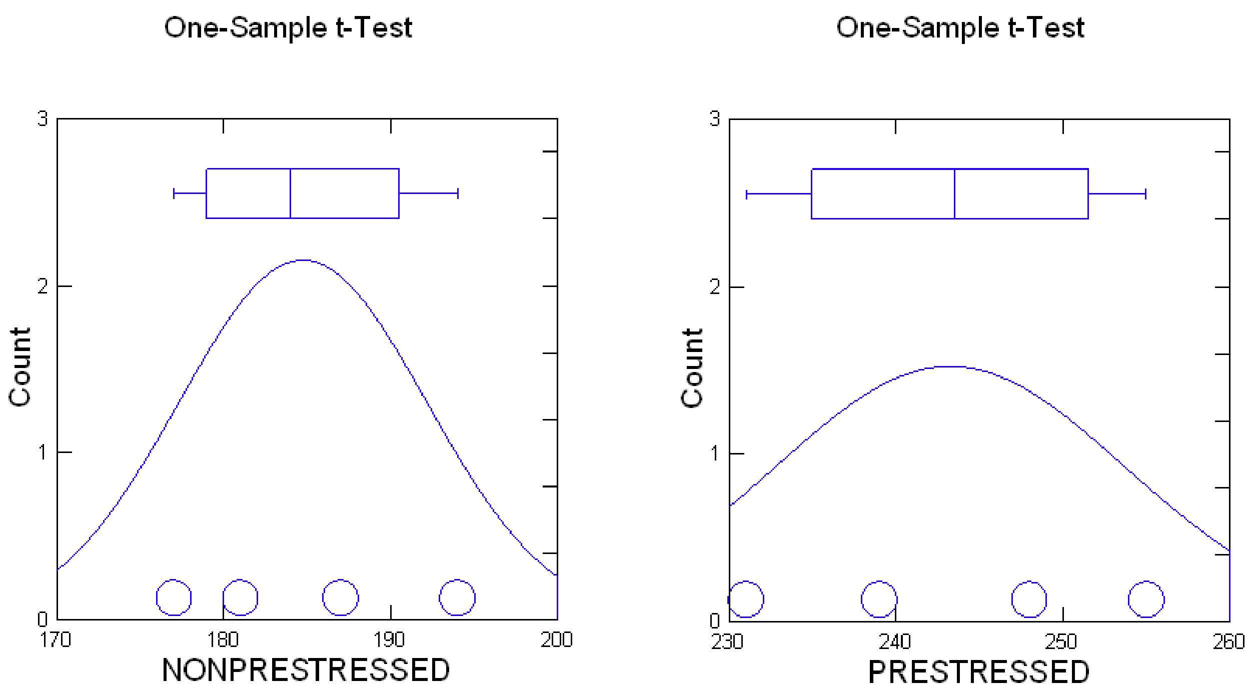

Figure 80. Statistical analysis of experimental results.

Table 8. Statistical analysis of data for prestressed and non-prestressed

Variable	N	Mean	Standard Deviation	95.00% Confidence Interval		t	df	p-Value
				Lower Limit	Upper Limit			
PRESTRESSED	4.000	243.250	10.468	226.593	259.907	46.474	3.000	0.000
NONPRESTRESSED	4.000	184.750	7.411	172.958	196.542	49.861	3.000	0.000

The standard deviation of the measured valued of peak compressive load for prestressed specimens was higher than that for non-prestressed specimens. However, since the mean value of peak loads for prestressed specimens was also higher than that of non-prestressed specimens, comparison of variatios was conducted using the normalized values of strength. Equality of two variance test [64] was performed with the null hypothesis, Ho, and alternative hypothesis, H1, defined as:

Ho: Sd1=Sd2
H1: Sd1≠Sd2

where, Sd1 and Sd2 are standard deviations of the normalized values of strength for non-prestressed and prestressed specimens, respectively.

Table 9 summarizes the results of the “equality of two variance test” for significance level α= 0.05. The results indicate that the p-Value>α= 0.05. Hence, the null hypothesis cannot be rejected, and it can not be concluded that the variation of the normalized strength values for prestressed specimens is higher than that for non-prestressed specimens. In short, considering the rise in mean compressive strength with prestressing, the variances of peak compressive loads for non-prestressed and prestressed PRSEUS stringer subcomponents are statistically comparable. Figure 81 shows the distribution of the normalized strength values for prestressed and non-prestressed specimens.

Table 9. Results of the equality of two variance test

Variable	PRESTRESSING$	N	Mean	Variance
STRENGHT_RATIO	No	4.000	1.000	0.002
	Yes	4.000	1.000	0.002

Variable	PRESTRESSING$	95.00% Confidence Bound	F-Ratio	Df	p-Value
STRENGHT_RATIO	No	0.094	0.875	3, 3	0.542
	Yes				

Equality of Two Variances

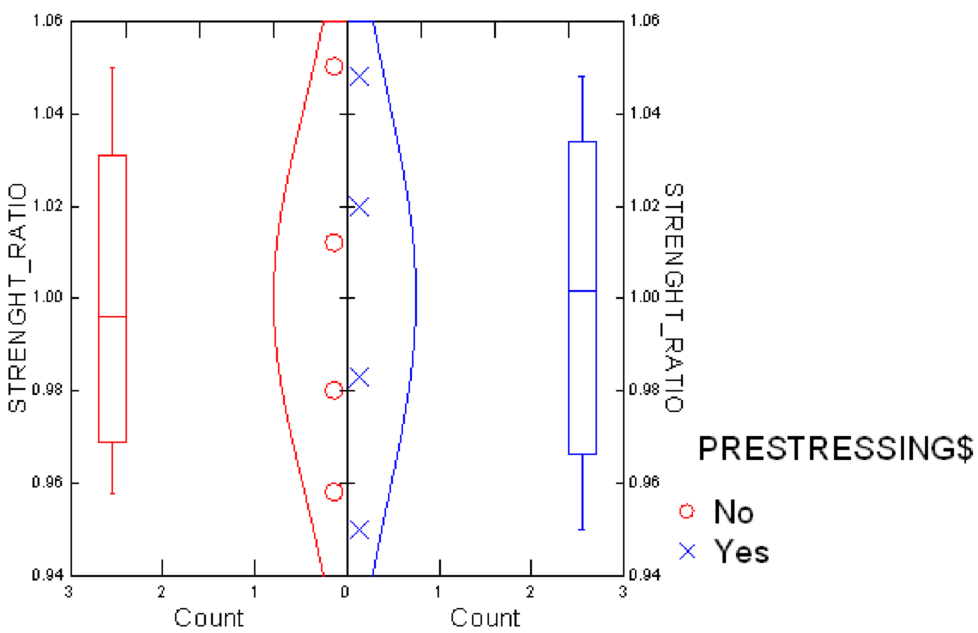

Figure 81. Distributions of the normalized strength values for prestressed and non-prestressed PRSEUS stringers.

4.5. Pretensioned PRSEUS Frame

In order to evaluate the prestressing effects on PRSEUS structural components of increasing size and complexity, frame specimens comprising a frame, two stringers and skin were fabricated without and with prestressing, and subjected to compression loading along the stringer direction. Because of the complexity of the frame structure, care was taken to establish its fabrication process, and the final product was checked against the minimum PRSEUS criteria.

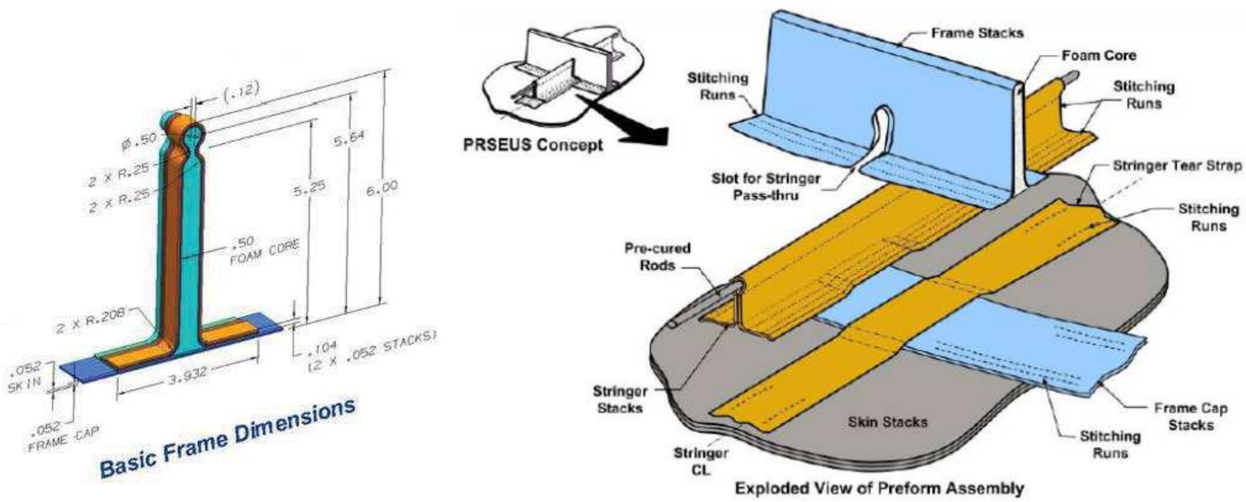

Figure 82. The PRSEUS frame structure.

Figure 83 shows the CAPRI process setup for “frame” PRSEUS specimens. Assembly of the dry fiber preforms for processing the PRSEUS specimen starts with cutting and kitting of the plies of dry fabric that make up the skin, the stringer and the frame components. The 50-inch wide warp-knit multi-axial carbon fiber fabric was cut into individual details, and placed into kits. One piece of 3.4 x 20 in, two pieces of 3.4 x 40 in, one piece of 20x40 in and one piece of 20x50 in fabric were used to assemble the PRSEUS frame specimen. The foam core was CNC machined with all the detail features required to support the frame plies, carbon fiber rods and resin infusion processing. The fabric plies for the frame were cut net as described above including the keyhole features required at stringer intersections. The details were then joined by stitching in order to create a preform assembly. The completed preform assembly was then transferred to a rigid tool (outer mold) (Figure 83a). After attaching the vacuum (outlet) and resin line (inlet) to the preform, the epoxy resin was pre-heated and degassed for 15 minutes at 250°F. Once the desired vacuum level was established, the resin was introduced into the flow media (which rests on the inner surface of the part) where it rapidly moved across the part surface before finally migrating through the thickness. Once the part was filled with resin at 250°F, the cure cycle was implemented at 350°F (Figure 83c).

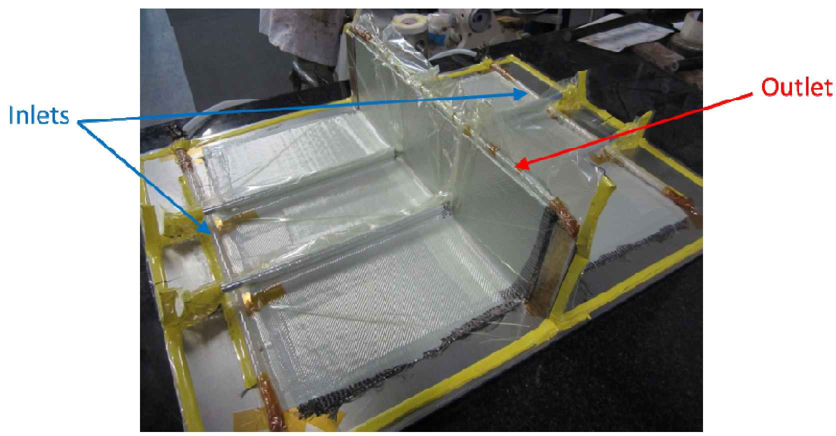

(a) Tooling

Figure 83. PRSEUS fabrication steps.

Figure 83 (cont'd).

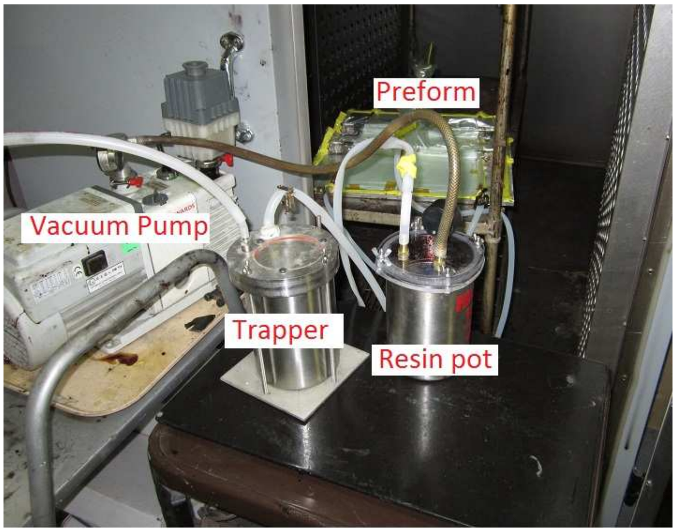

(b) Infusion and curing setup

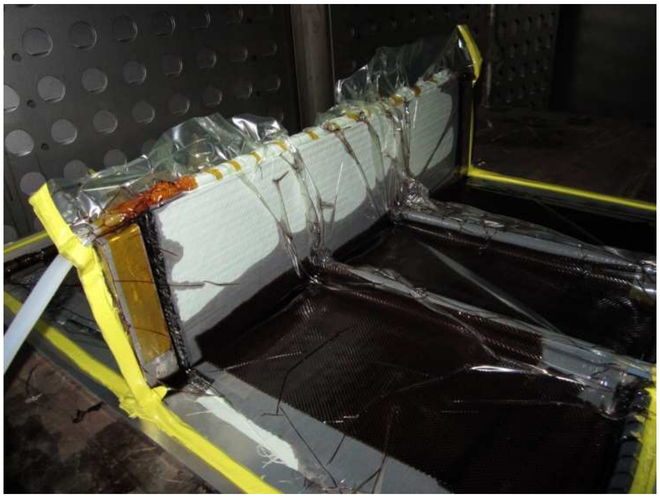

(c) Infusion step

As noted earlier, bonding of the pultruded rods to the multiaxial constituent of PRSEUS was prevented during resin infusion by a Teflon tube covering the rods. Once the infusion and curing cycles were completed, the pultruded rods were withdrawn from the wrapping (multiaxial) stiffener constituent, and prepared for the subsequent prestressing/bonding step.

4.5.1. Prestressing of PRSEUS Frame

The rods were wrapped with the non-creep, high-performance adhesive film. The adhesive film would help establish aerospace-quality, thermally stable bonds between the pultruded rods and the multiaxial fabric constituent of PRSEUS, which exhibit minimum creep deformations. After inserting the pultruded rods into the holes of the stiffeners (stringers), the prestressing fixtures (introduced in previous reports) were mounted at the ends of the pultruded rods. Each fixture comprises a steel tube filled with high-performance epoxy. The steel tube length is 250 mm; it has an outer diameter of 25 mm and a wall thickness of 5 mm. The inner surface of the tube is threaded in order to enhance bonding between the filled epoxy and the steel tube.

The pultruded rods were subjected to (pre-)compression loading using the light-weight prestressing tooling introduced earlier. The compressive load is transferred from the tooling to the fixture tube via bearing action, and then transferred to the wall of metal end fixtures. The load is finally transferred to the rods via interfacial shear between the epoxy filled end fixtures and the pultruded rod. The pre-compression load is shown as red arrows in Figure 84. The rod pre-compression is balanced by the pre-tension developed in the multi-axial composite constituent of PRSEUS (blue arrows in Figure 84). This pre-tension is transferred by the gripping mechanism between the prestressing tooling and the specimen during the application of pre-compression. The grips used here are similar to those employed in tension tests on composites. The prestress level was monitored by strain gages mounted on the pultrudeds rod and the multi-axial composite constituent of PRSEUS. The targeted compressive pre-strain developed in the pultruded rod was 8,000 microstrain. The pre-compression in pultruded rods and the balancing pre-tension in multi-axial composite were retained, and the whole system was placed in an oven where it was subjected to the curing cycle of the epoxy adhesive film. This curing cycle comprised one hour of exposure to 300^{o}F.

Figure 84. Application of the compressive prestrain to the pultruded rods using the new prestressing tooling, with balancing pre-tension developed in the multi-axial composite constituent of PRSEUS.

Once the curing cycle was completed, four strain gages were mounted on the PRSEUS specimen, and connected to the data acquisition system. The pretressing force in pultruded rod was then released from the external support system, and transferred to the multiaxial fiber composite constituent of PRSEUS via interfacial bond shear between them.

4.5.2. Specimen Preparation, and Compression Test Procedures

To prepare the specimen for compression test, two potted plates were used as end plates. The end plates produce fixed support conditions, and also allow for load transfer to specimen via shear mechanism between the end grips and the ends of the PRSEUS frame specimen. As shown in Figure 85, a steel plate 25 mm in thickness, with a TT shaped piece cut out of it, constitutes the end plate. The gap between the end plate cut-off and the stringer specimen is filled by a high-performance epoxy to simulate the actual support condition of PRSEUS stringer under service loads.

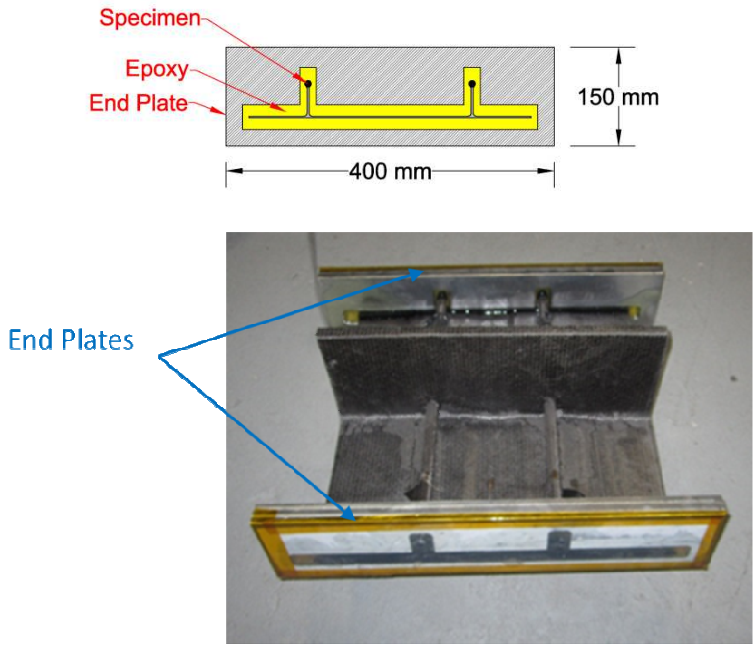

Figure 85. End potted plates constraining the PRSEUS frame specimen ends in compression tests.

PRSEUS frame specimens were subjected to compression loading to failure in a servovalve-controlled hydraulic test system at a constant displacement rate of 0.1 mm/sec. During compression loading, the applied force and the crosshead displacement were recorded using a computer-based data acquisition system. Compressive force was applied along the stringer direction. Figure 86 shows the compression test setup.

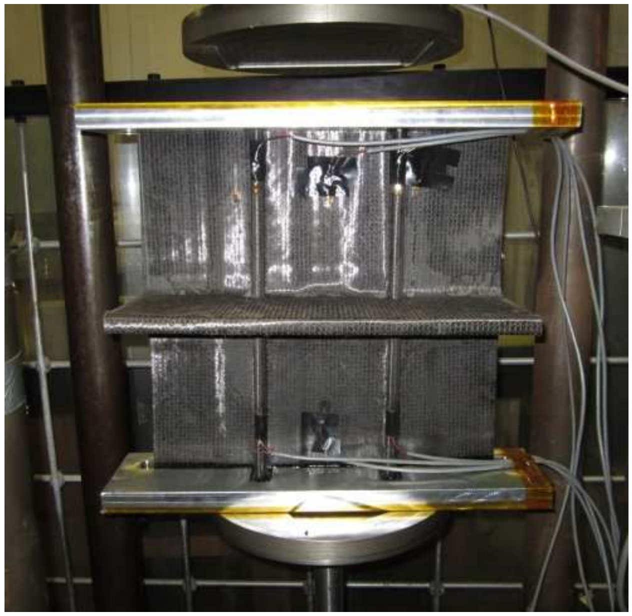

Figure 86. Compression test setup.

4.5.3. Experimental Results and Discussion

The measured value of peak compressive load for prestressed the PRSEUS frame specimen was 387 KN which was approximately ~25% (based on one replicated test) higher than that of the non-prestressed specimen (301 KN). Figure 87 shows the results of compression tests on non-prestressed and prestressed PRSEUS specimens. The failure mechanism in compression initiated from the conjunction area of the stringer and skin, leading to failure of the stringer web followed immediately by failure of the wrapping multiaxial composite. The failure path and mechanism were similar to those observed in compression tests on non-prestressed PRSEUS stringer specimens reported earlier. Figure 88 shows a failed frame specimen.

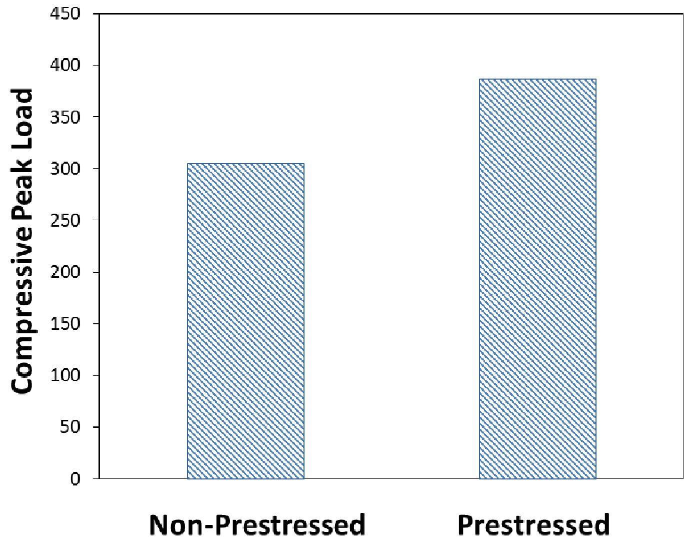

Figure 87. Peak compressive loads of prestressed vs non-prestressed prseus frame specimens.

Figure 88. Prestressed PRSEUS frame specimen after failure in compression.

4.6. Evaluation of the Stability of Prestressing Force over Time in Prestressed PRSEUS

Stability of the prestressing force is important for preserving the structural benefits of prestressing over the life of structure. A comprehensive experimental work was conducted towards determining and mitigating any excess creep deformations and losses of prestressing force. Also, effects of thermal cycliing at high humidity on prestressed structures was investigated in order to assure stability of prestressing under repeated freez-thaw cycles.

4.6.1. Creep

Creep is the time-dependent deformation of a material under constant stress. While all materials exhibit an initial elastic strain when stressed, strain tends to increase over time under sustained stress. If a material is perfectly elastic, either linear or nonlinear, strain (ε) will not increase over time, and will be a function of stress (σ) only, as expressed below (the following equations assume that environmental conditions such as temperature and moisture are held constant).

$$\varepsilon = f(\sigma) \tag{1}$$

Elastic solids store energy when they are loaded, and use this energy to return to their original shape when unloaded. Liquids, on the other hand, are viscous in that they flow when loaded externally, and the extent to which they deform is time-dependent. However, if a material exhibits a behavior that is a combination of viscous and elastic responses to external forces, it is considered viscoelastic (with time-dependent response to stress). The strain developed in a viscoelastic material is a function of both stress and time:

$$\varepsilon = f(\sigma, t) \tag{2}$$

A viscoelastic material can be characterized as either linear or nonlinear with respect to stress. In Eq. (2), $f(\sigma, t)$ can be expressed in terms of two components, one dependent on time, $h(t)$, and the other dependent on stress, $g(\sigma)$ (implying that the stress- and time-dependencies of strain are separable):

$$\varepsilon = g(\sigma).h(t) \tag{3}$$

Assuming that the material is linear viscoelastic, the function $g(\sigma)$ would be linear with respect to stress. Likewise, if the material is non-linear viscoelastic, then $g(\sigma)$ would not be linear. For a linear viscoelastic material, the constant associated with $g(\sigma)$ could be included with $h(t)$ in a newly defined function, $S(t)$, which is called creep compliance. Therefore, Eq. (3) becomes:

$$\varepsilon = S(t).\sigma \tag{4}$$

Rearranging Eq. (4), creep compliance can be expressed as:

$$S(t) = \varepsilon(t)/\sigma \tag{5}$$

If the material is linear viscoelastic, the creep compliance, $S(t)$, will be identical for any given constant stress, $\sigma = \sigma_o$. However, for a material that is assumed to be linear elastic (strain does not increase with time), creep compliance is simply $\varepsilon/\sigma = 1/E$, where E is the elastic modulus of the material. For a nonlinear viscoelastic material, compliance would be dependent on both time and stress:

$$S(t, \sigma) = \varepsilon(t, \sigma)/\sigma \tag{6}$$

Creep compliance, $S(t)$, is determined through performance of creep tests that measure strain as a function of time for a given level of sustained stress, regardless of whether the material is linear or nonlinear viscoelastic. In contrast to strain data alone, creep compliance is normalized with respect to stress, allowing creep data produced in tests at differing stress levels to be compared.

Under sustained stress, the inherent creep deformations of PRSEUS structural components (rod and multiaxial composite) combined with the creep deformation within the bond region between the two lead to losses of the prestressing force over time. Typical experimentla data reported in the literautre on creep deformations of carbon fiber/epoxy composites at different temperatures

(Figure 89a) and under different sustained stress levels (Figure 89b) indicate that creep strains of composites are relatively small, and occur mostly within few days of application of sustained stress. Creep strains tend to increase slightly with increasing temperature.

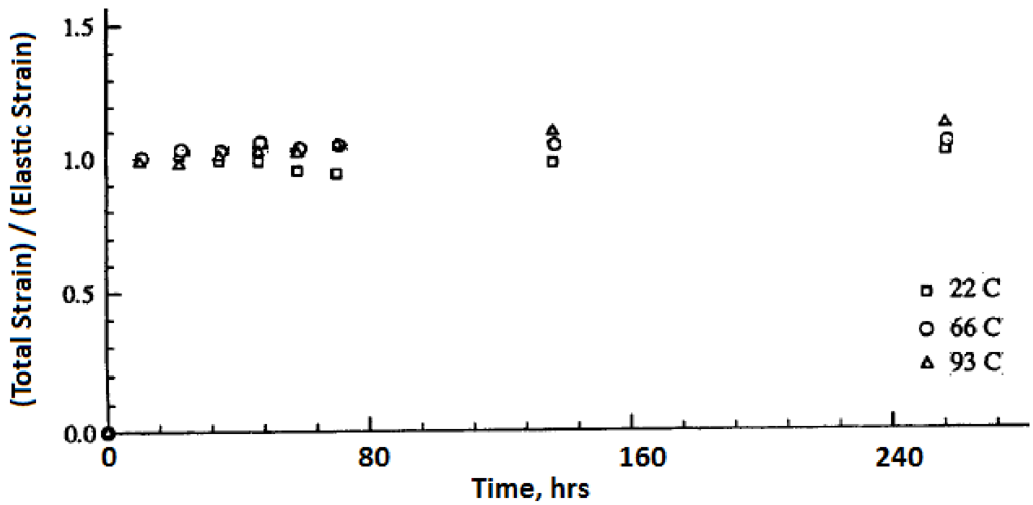

(a) Strain Rise Over Time Under Sustained Tensile Stress of ~25% the Ultimate Strength [65]

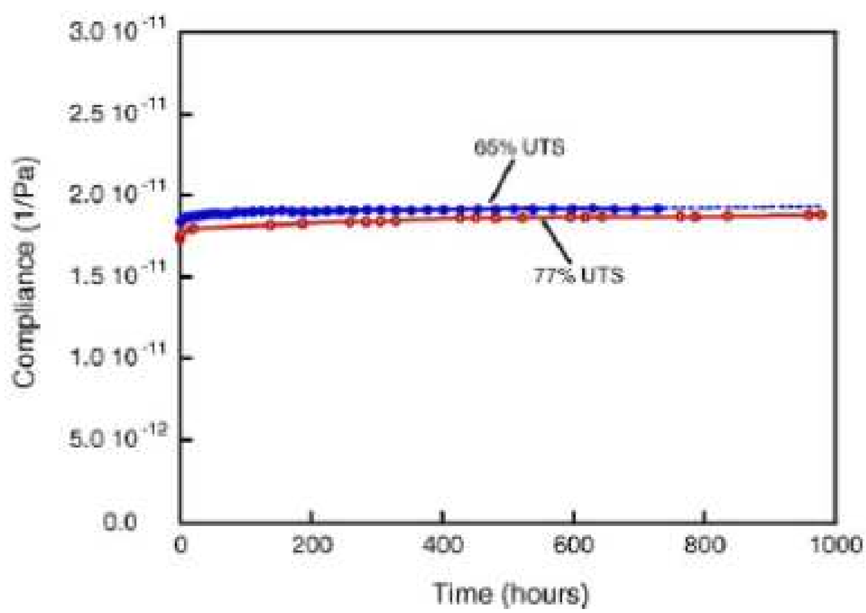

(b) Effect of Sustained Stress Level (expressed as a percent of ultimate tensile strength – UTS) on Compliance (invese of elastic modulus) at 22^{o}C [66]

Figure 89. Typical creep test results for carbon fiber/epoxy composites.

Under sustained stress, creep deformations of composite structures combined with stress relaxation of prestressing rods produce losses of prestressing force over time. The approach devised in this research to prestressing of PRSEUS composite structures starts with prestressing of pultruded rods against an outside support. Upon release of this prestress after curing of either composite or the bond between pultruded rods and the multiaxial composite, the prestressing force is transferred from external support to the multiaxial fiber composite constituent of PRSEUS via interfacial bond. The bond between the pultruded rod and the multiaxial composite should be capable of transferring the prestress from pultruded rods to the multiaxial fiber composite constituent of the PRSEUS composite structure.

The fact that the interfacial bond region between the pultruded rods and the multiaxial fiber composite in PRSEUS is generally non-reinforced makes this region susceptible to excess creep deformations. The relatively small thickness of this region, on the other hand, limits the contributions of its relatively large creep deformations to the losses of prestressing force over time. The creep strain, $\gamma(t)$,occurring in the bond region between the pultruded rod and the multiaxial fiber composite can be expressed as:

$$\gamma(t) = \Delta L(t) / h$$

where, h is the thickness of the bond region, and $\Delta L(t)$ is the time-dependent shear deformation within the bond region. In addition, the average shear stress, τ, acting along the bond length can be computed as follows:

$$\tau = P / A \qquad (7)$$

where, A is the interfacial bond area responsible for stress transfer, and P is the prestressing force in pultruded rod. The normalized creep compliance, $J_n(t)$, of the bond region can be computed as follows [67]:

$$J_n(t)=(1/J(0)).(\gamma(t)/\tau) \quad (8)$$

Where, J(0) is the elastic compliance, and $(\gamma(t)/\tau$ is the creep compliance.

4.6.1.1 Evaluation of the Compressive Creep of Pultruded Rod in Prestressed PRSEUS (Stringer) Specimen

The creep phenomenon occurs in the pultruded rod, the multiaxial composite, and the interfacial bond region of PRSEUS composite structures. Experimental investigations of the creep attributes of these PRSEUS constituents started with evaluation of the long-term creep deformations of the pultruded rod under sustained loading. Creep tests were conducted at room and elevated (85°C) temperatures over a time period of 120 hours.

Figure 90 shows schematics of the creep test setup for pultruded rod under sustained compressive loading. The rod, which was wrapped with a non-friction release film (which prevents any physical bonding or mechanical interlocking of the rod) is supported against lateral buckling by a multiaxial composite; the rod is sandwiched between two stacks of multiaxial composite. The non-friction release film interfacing the rod and the multiaxial composite assures that no portion of the applied force, P, is transferred to the multiaxial composite.

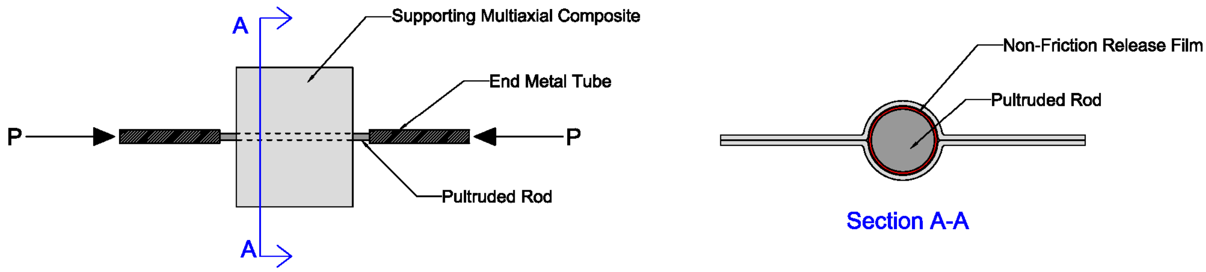

Figure 90. The pultruded rod creep test setup.

Strain values were recorded over time for each sample at ambient and elevated temperatures. Figure 91 shows results of creep tests performed on a pultruded rod subjected to sustained compression. Generally, in both tests at room and elevated temperatures, the bulk of creep deformations occurred within a short time period after the test began. Then rate of creep reduced until creep deformations approached a constant value. As expected, creep deformations at elevated temperature were larger than those at room temperature. Creep strains at room temperature produced about 1% (based on one test) rise in elastic strains (with the rod strain increasing from 8000 to 8105 microstrain over 120 hours). This rise was ~5% (based on one test) at elevated temperature (with the pultruded rod initial strain of 8000 microstrain increasing to

8360 microstrain over 120 hours). The relatively low compressive creep strains observed here can be attributed to the effect of lateral support of the multiaxial composite which prevents local buckling of fibers in the pultruded rod under compression. This positive feature also exists in PRSEUS composite structures where pultruded rods are supported against lateral buckling by the multiaxial composite constituent of PRsEUS. Pretensioning of the multiaxial composite greatly benefits its confinement/lateral support actions when compared with the test specimen of Figure 90.

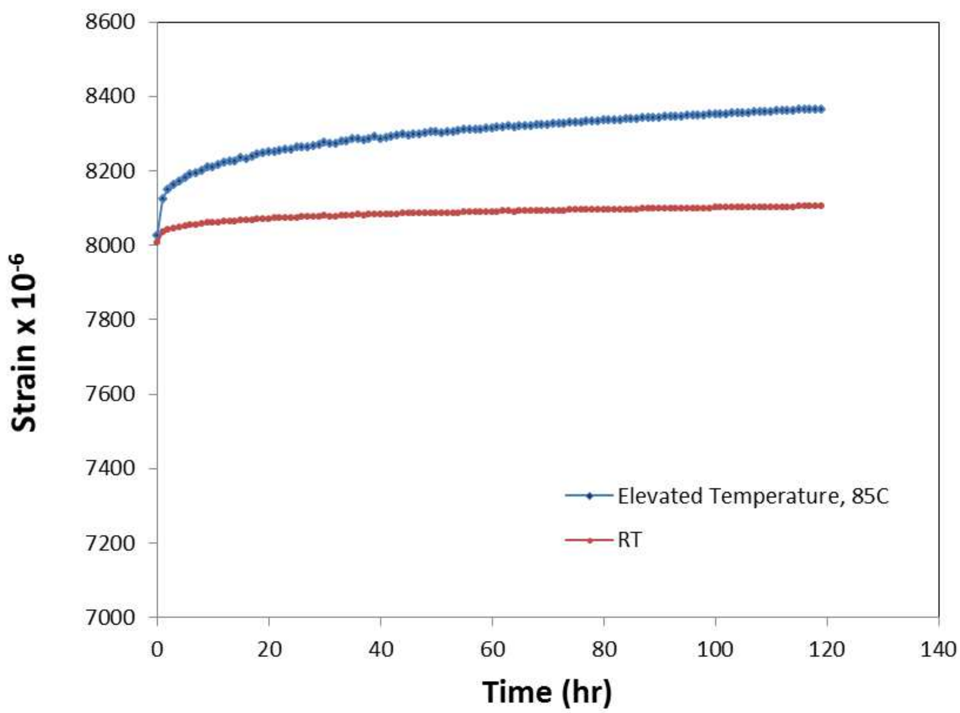

Figure 91. Compression creep test results at room and elevated temperatures for pultruded rod supported against lateral buckling by multiaxial composite.

The compressive creep test data for pultruded rod in conditions (conservatively) simulating those in PRSEUS indicated that the compressive creep deformations of pultruded rod are negligible even at elevated temperatures. Hence, losses of prestressing force cannot be attributed (to any large extent) to the creep deformations of pultruded rods.

4.6.1.2. Creep Deformations within the Interfacial Bond Region

As noted earlier, the non-reinforced bond region is vulnerable to excess creep deformations. Efforts were made to employ an adhesive agent with minimal creep deformations. Thus, creep tests on the interfacial bond region in PRSEUS were conducted using three different adhesive bond agents: (i) bonding form via infusion of the multaxial constituent of PRSEUS with epoxy resin; (ii) Redux 312 adhesive film; and (iii) AF162-2A adhesive film. The processing steps involved in formation of PRSEUS stringer specimens with these interfacial bonding conditions were explained in part 4.5. For the infused bonded specimens (first set) interfacial bonding is established simultaneously with the infusion of the multiaxial composite.

Once the curing cycle was completed, four strain gages were mounted on the PRSEUS specimen, and connected to the data acquisition system. Figure 92 shows the prestressed specimen, after transfer of the prestressing force, that is subjected to creep tests. The strain values recorded by strain gages were recorded over a 36-hour period at ambient and elevated (85°C) temperatures. The reference strain gage (Figure 92) was used to monitor the losses of prestressing force.

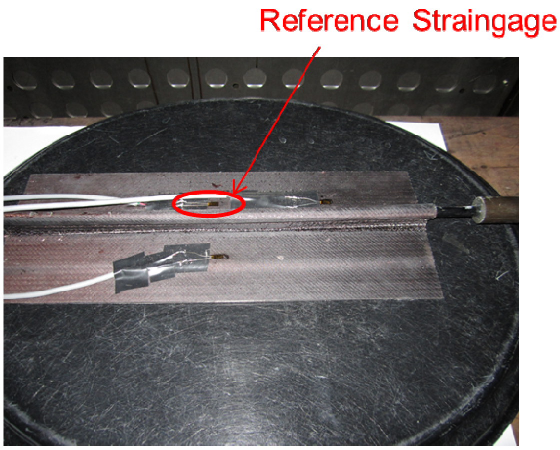

Figure 92. Creep test setup.

Experimental Results and Discussion

Figure 93 presents the values of strain, measured at room and elevated (85^{o}C) temperatures, on top of the stringer specimen (at mid-span) versus time. The losses of prestress are observed to occur at a relatively fast rate within few hours after transfer of the prestressing force. After about 24 hours, the prestressing force tends to stabilize. As noted earlier, we have attributed these losses primarily to creep deformations within the polymeric interface of the pultruded rod and the multiaxial composite constituent of PRSEUS. Since the (uniaxial fiber composite) pultruded rod experiences less creep, which would have already occurred during the time period it is prestressed against an external support, its creep (relaxation) is not expected to make any important contribution to the loss of prestressing force after it is transferred to the multiaxial composite constituent of PRSEUS. The contributions of creep within the multiaxial composite constituent of PRSEUS to losses of prestressing force are also secondary when compared with those of the interfacial bond region.

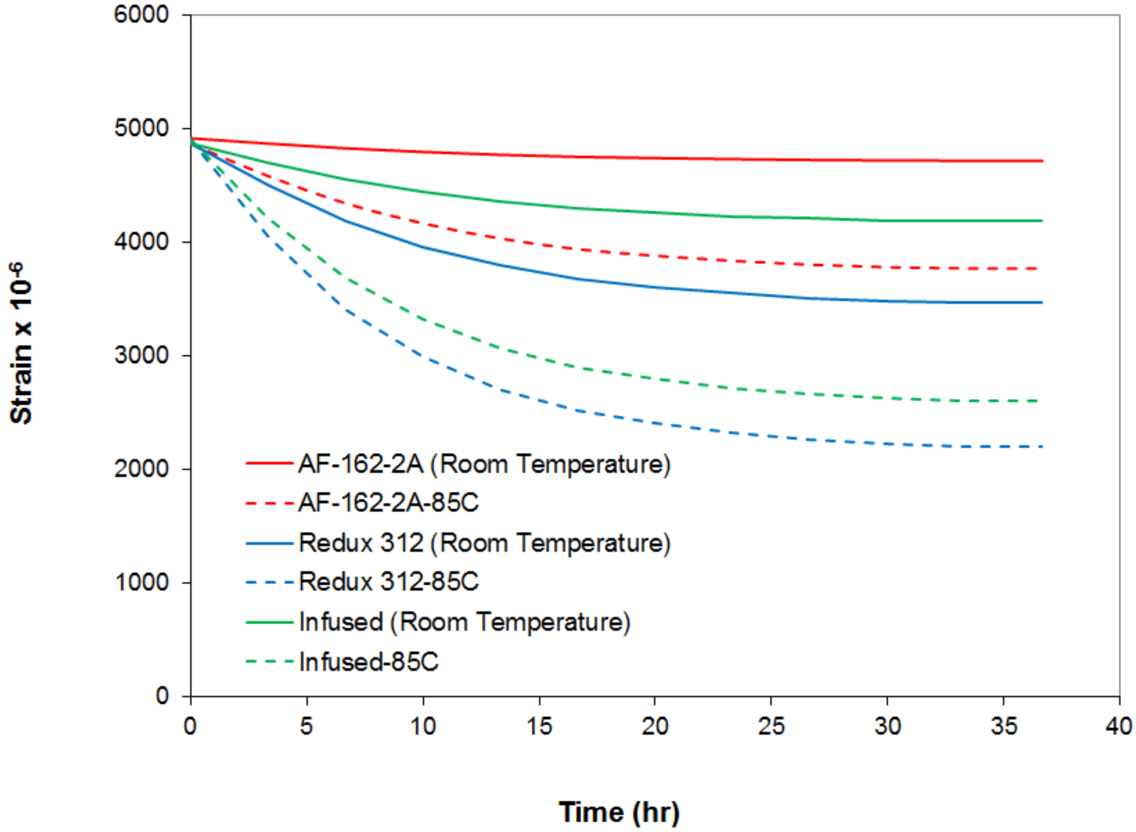

Figure 93. Strain versus time at different temperatures for prestressed PRSEUS stringer specimens.

The creep test results summarized in Table 10 indicate that the low-creep adhesive film (AF-162-2A) controls losses of the prestressing force. An initial prestrain of 4,950 microstrain dropped to 4,740 microstrain after 36 hours at room temperature (corresponding to ~4% loss of prestressing force, based on one test) when the AF-162-2A low-creep adhesive film was employed. As expected, the loss of prestressing force was more pronounced at the elevated temperature of 85°C (22% over 36 hours based on one test), from 4,940 to 4,340 microstrain. The levels of creep loss observed with other bonding agents were significantly higher than the upper creep threshold of ~20%.

Table 10. Summary presentation of creep test data for prseus stringer specimens.

	Total Creep	
Bond Agent	Room Temperature	Elevated Temperature (85°C)
Infusion-Based	14%	47%
Redux 312 Adhesive	29%	55%
AF-162-2A Adhesive	4.0%	22%

4.6.2. Environmental Effects

Since aircraft experience thermal cycling during each take-off from a warm airfield, which can turn into freeze-thaw cycling in the case of take-off from a warm and humid airfield, stability of the structure and the prestressing force under freeze-thaw cycles is a concern. Freeze-thaw cycling aggravates any adverse effects of thermal cycling due to the expansive stresses applied by freezing water absorbed in constrained areas. Similar effects of freeze-thaw cycles on prestressed concrete structures have been investigated [68, 69]; some investigations have also undertaken on the stability of pultruded (FRP) composite reinforcement and concrete under freeze-thaw cycles [70-72]. These studies concluded that freeze-thaw cycles can deteriorate the bond between concrete and composites. Abdol and Aglan conducted an experimental investigation of the performance of adhesive joints between composite parts under temperature cycles [73]. Single-lap shear tests indicated that temperature cycles insignificantly lower the shear strength of adhesive bonds between composites, and also increase the deformation at failure (by lowering the elastic modulus) of adhesive bonds by 20%.

The fact that the interfacial bond region between the pultruded rods and the multiaxial fiber composite in PRSEUS is generally non-reinforced makes this region potentially susceptible to degradation under thermal cycling.

Experimental work

In order to evaluate the stability of prestressing under freeze-thaw cycles, one prestressed PRSEUS stringer specimen was subjected to repeated cycles of freezing and thawing. Each cycle comprised 8 hours of freezing at -30^{o}C followed by 8 hours of thawing at 50^{o}C temperature and 100% relative humidity. In order to prevent thermal shock upon transition from freeze to thaw step, the sample was kept at room temperature for one hour after the freeze step. The total duration of each cycle was 18 hours. The temperature time-history for each freeze-thaw cycle is shown in Figure 94. The specimen was subjected to 10 freeze-thaw cycles.

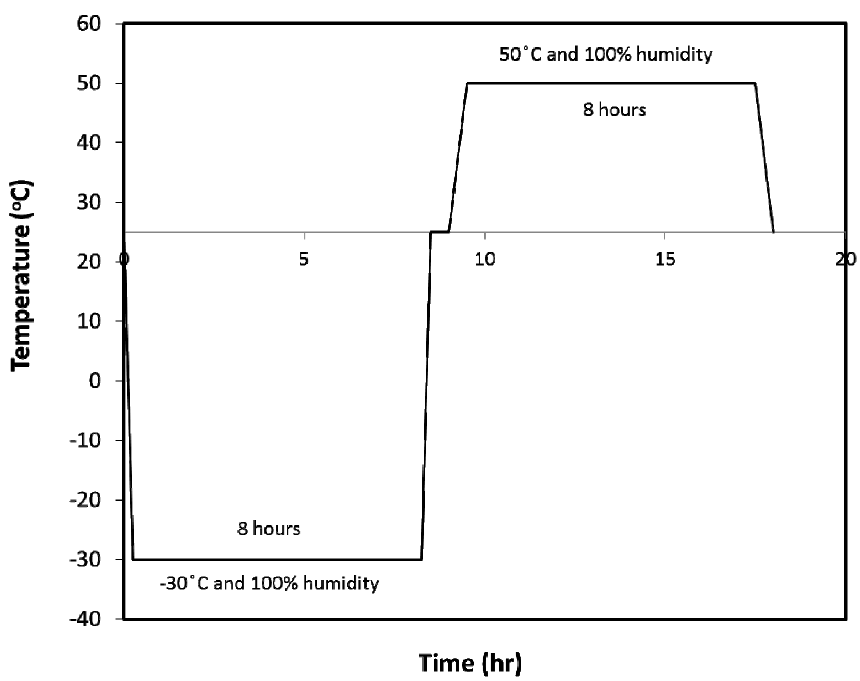

Figure 94. Temperature time-history during one freeze-thaw cycle.

The prestressed PRSEUS stringer was fabricated and prestressed. Once the curing cycle was completed, four strain gages were mounted on the PRSEUS specimen, and connected to the data acquisition system. Then the thermal cyclic started while the specimen was transferred into freezer for 8 hours followed by 8 hours of thawing step in humidity chamber. Figure 95 shows the specimen during freezing and thawing step.

(a) Freezing step (b) Thawing step

Figure 95. Freeze-thaw test setup.

Figure 96 presents the values of strain versus time, measured during the freeze-thaw cycles with a strain gage placed on top of the stringer specimen (at midspan). The losses of prestress are observed to occur at a faster rate within the first few cycles after transfer of the prestressing force. After 24 hours, the prestressing force tends to stabilize. We have attributed these losses primarily to two phenomena: (i) partial degradation of the polymeric bond at the interface of the pultruded rod and the multiaxial composite constituent of PRSEUS under freeze-thaw cycles; and (ii) creep deformations within the polymeric bond region at the elevated temperature of 50^{o}C (corresponding to the thaw step in freeze-thaw cycles).

Experimental results indicated that an initial prestrain of 4,970 microstrain dropped to 4,310 microstrain after 10 cycles. (corresponding to ~10-15% loss of the prestressing force based on one test). Although this loss of prestressing force is within the acceptable level of 20% assumed in design, the freeze-thaw loss can be mitigated by selecting an adhesive agent which offers improved stability in humid environments when exposed to temperature cycles. It should be noted that the adhesive agent used here was selected based on its structural performance and high-temperature creep behavior.

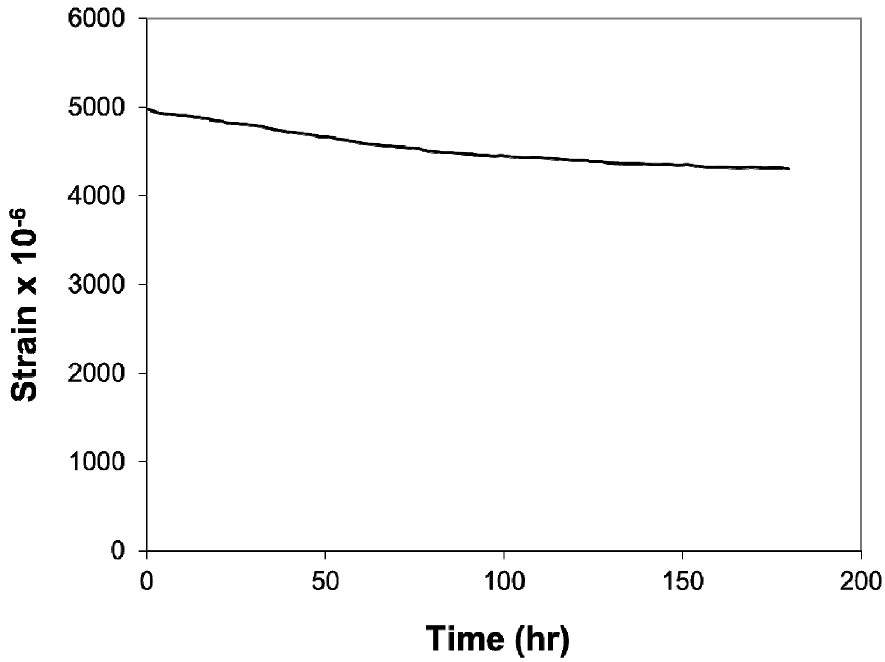

Figure 96. Prestrain time-history in prestressed PRSEUS specimen subjected to repeated freeze-thaw cycles in humid environment.

Chapter 5. Analytical and Numerical Modeling

This chapter presents an analytical model to predict the contribution of prestressing towards delaying the buckling of the web of the PRSEUS stringer subcomponent. Finite element analysis of the stringer subcomponent is also reviewed. Comparisons are made between analytical predictions of prestressing effects versus experimental results.

5.1 Analytical formulation

Experimental observations indicate that failure of PRSEUS is governed by the buckling of stringer, which involves initial local buckling of its web (multiaxial component) followed by failure of the wrapping multiaxial wrapping around the pultruded rod, which leads to buckling of the pultruded rod due to loss of confinement. The pultruded rod, which is under-utilized here, can carry more load if local buckling of the web could be delayed. A prestress system comprising pre-compressing of the pultruded rod and pre-tensioning of the multiaxial composite delays local buckling in compression of the (pre-tensioned) web. This prestress system is schematically depicted in Figure 97.

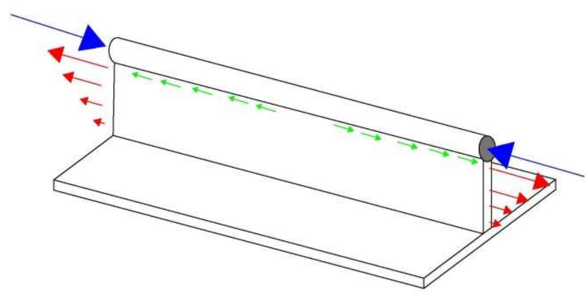

Figure 97. Schematic depiction of the prestress system comprising pre-compression in pultruded rod and pre-tension in the web.

5.1.1. Analytical Formulation

Since failure occurs at the web of the PRSUS stringer, a simplified analytical model was developed for the buckling failure mode of this component. The web was modeled as an orthotropic plate restrained along the four edges, with edges along y-axis subjected to a linear uniform load (Figure 98). The effect of the pultruded rod was modeled as an elastically flexible support whose with a stiffness that reflects the flexural stiffness of the pultruded rod. A camped support condition was assumed at the conjunction of the skin and the web. This simplified model reflects presence of a relatively thick skin that is stitched to the web plate. Other edges along the y-axis are assumed to be simply supported.

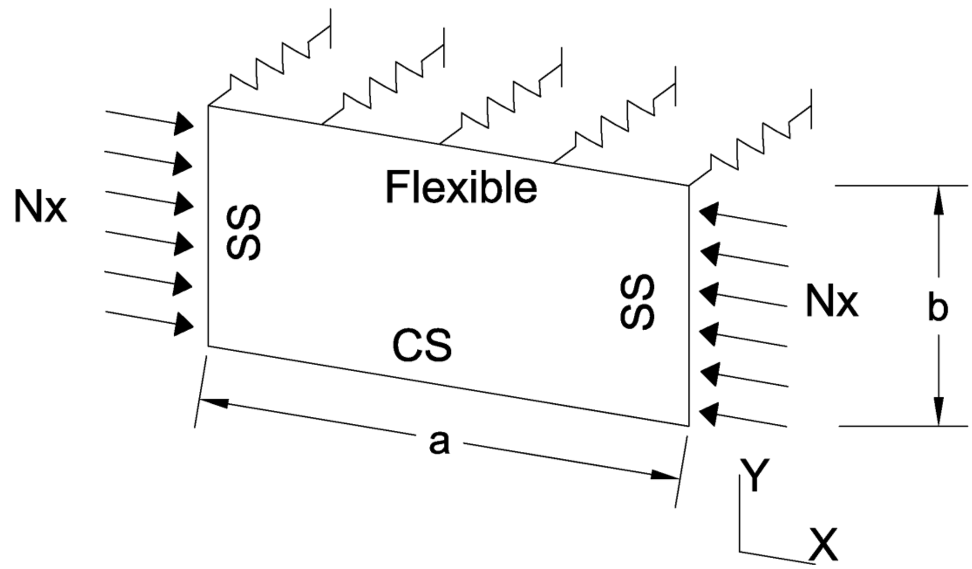

Figure 98. Model of the stiffener plate under uniform compressive loading.

The prestressing effect was modeled as external linear loading calculated using classic prestressing equations (Figure 99). An explicit solution was developed for calculating the local buckling of the prestressed composite plate. Prestressing was be considered as a parameter in analysis of composite plate structures.

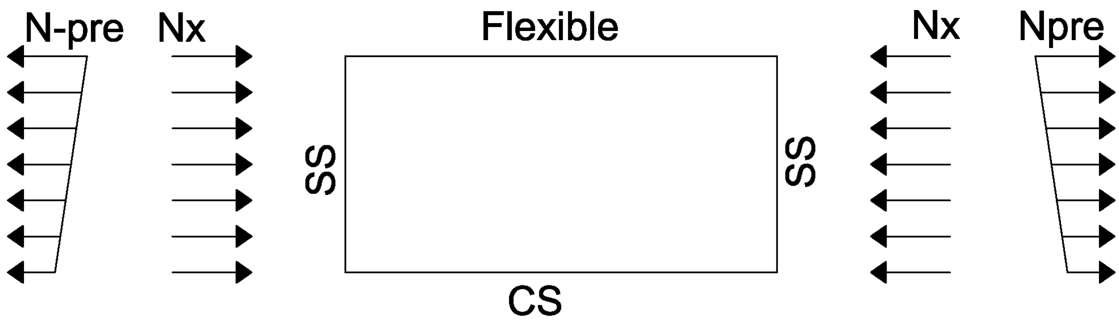

Figure 99. The prestress (Npre) and compressive load (Nx) systems applied to the stiffener web plate.

5.1.2. Variational Energy Formulation

In order to analyze local buckling of the web plate, the first variational principle of total potential energy was employed [74]. In general, the total potential energy (Π) of a plate structure is equal to the summation of the strain energy (*U*) stored in the plate and the flexible restraint edges, and the work (*V*) done by external loads. It can be expressed as:

$$\Pi = U + V \tag{5.1}$$

where, $V = -\sum N_i\, q_i$, and $U = U(\varepsilon_{ij})$. Thus,

$$\Pi = -\sum N_i\, q_i + U(\varepsilon_{ij}) \tag{5.2}$$

For linear elastic problems, strain energy is expressed as

$$U = \frac{1}{2}\int_V \sigma_{ij}\, \varepsilon_{ij} dV \tag{5.3}$$

The stationary state for a system corresponds to the state where the first variation of the total potential energy ($\delta\Pi$) is zero. Hence, the condition for state of equilibrium can be expressed as

$$\delta\Pi = -\sum N_i \delta q_i + \int_V \sigma_{ij}\, \varepsilon_{ij} dV = 0 \tag{5.4}$$

A variational formulation of the Ritz method [75] was then applied to solve the elastic buckling problem of the elastically restrained orthotropic plate subjected to non-uniform, in-plane axial load (i.e., N_x and N_{pre}). The plate was elastically restrained with the elastic translational restraint stiffness coefficients k along x-axis at $Y = b$ (see Figure 99). In the variational form of the Ritz method, the first variation of the elastic strain energy stored in the plate (δU_e), the strain energy stored in the elastic restraints along the rotationally restrained boundaries of the plate (δU_e), and the work done by the in-plane biaxial force (δV) are computed by proper selection of the out-of-plane buckling displacement functions (w). The elastic strain energy in an orthotropic plate (U_e) is expressed as

$$U_e = \frac{1}{2}\int_\Omega \int \left\{ D_{11} w_{xx}^2 + D_{22} w_{yy}^2 + 2D_{12} w_{xx} w_{yy} + 4D_{66} w_{xy}^2 \right\} dxdy \tag{5.5}$$

where, D_{ij} (i, j = 1, 2, 6) are the coefficients of the plate bending stiffness (Jones 1999), and Ω is the area of the plate. Therefore, the first variational form of elastic strain energy stored in the plate (δU_e) becomes

$$\delta U_e = \iint_\Omega \left\{ D_{11} w_{xx} \delta w_{xx} + D_{22} w_{yy} \delta w_{yy} + D_{12}(w_{xx} \delta w_{yy} + w_{yy} \delta w_{xx}) + 4D_{66} w_{xy} \delta w_{xy} \right\} dxdy$$

(5.6)

The strain energy stored in the translational restrained edge (U_Γ) is equal to the energy stored in the pultrueded rod as flexible support of the plate, and can be expressed as:

$$U_\Gamma = \frac{1}{2}\int_0^a EI(w_{xx}|_{y=b})^2 dx \tag{5.7}$$

where, E and I are the elastic modulus and the moment of inertia of the pultruded rod. The corresponding first variation of strain energy stored in the elastic restraints along the translational restrained boundary of the plate (δU) can thus be calculated as

$$\delta U_\Gamma = \int_0^a EI(w_{xx}|_{y=b})\delta(w_{xx}|_{y=b}) dx \tag{5.8}$$

The work (V) done by the in-plane non-uniformly distributed axial compressive force (N_x, N_{pre}) (Figure 98) can be written as

$$V = \frac{1}{2}N_x \iint_\Omega w_x^2\, dxdy - \frac{1}{2}N_{pre-b} \iint_\Omega (1+\alpha\frac{y}{b})w_x^2\, dxdy$$

(5.9a)

where, Nx is the uniform compressive force per unit length and Npre-b is the prestressing (tension) load at the level of y=0, and α is defined to reflect the non-uniformity of prestresing load along the y-axis, expressed as

$$\alpha = \frac{(N_{pre-u} - N_{pre-b})}{N_{pre-b}} \tag{5.9b}$$

Hence, the first variation of work done by the in-plane biaxial force becomes

$$\delta V = N_x \iint_\Omega w_x\, \delta w_x dxdy - N_{pre-b} \iint_\Omega (1+\alpha\frac{y}{b})w_x \delta w_x\, dxdy \tag{5.10}$$

Using the equilibrium condition of the first variational principle of the total potential energy (see Eq. (5.4))

$$\delta\Pi = \delta U_e + \delta U_\Gamma - \delta V = 0 \tag{5.11}$$

and substituting the proper out-of-plane displacement function (w) into Eq. (5.11), the standard buckling eigenvalue problem can be solved by the Ritz method.

5.1.3. Out-of-Plane Displacement Function

Choice of a proper out-of plane buckling displacement function (w) is very important in solving the eigenvalue problem. Several shape functions are proposed in the literature based on either combined sinusoidal or polynomial functions [76-78]. Qiao proposed a combined harmonic and polyniomial function for plates with a free edge [79]. This shape function develops one harmonic shape along the free edge and polynomial shape along the edge perpendicular to that.

For the particular case of the first buckling mode, which develops one half-wave and one polynomial shape along the X axis and Y axis, respectively, of the plate was considered in this study to obtain the explicit local buckling solution of the plate. The general form of the buckling displacement is

$$w(x,y) = w_0\left(\left(\frac{y}{b}\right)^2 + \eta_1\left(\frac{y}{b}\right)^3 + \eta_2\left(\frac{y}{b}\right)^4\right)\sin\frac{\pi x}{a} \tag{5.12}$$

By properly choosing the weight constants of η's, the novel displacement function in Eq. (5.12) provides an approach to account for the effect of the free edge of the plate.

As shown in Figure 98, the boundary conditions along the restrained and loaded edges can be written as

$$w(0,y) = 0 \tag{5.13a}$$

$$w(a, y) = 0 \tag{5.13b}$$

$$M_x(0, y) = -D_{11}\left(\frac{\partial^2 w}{\partial x^2}\right)_{x=0} = 0 \tag{5.13c}$$

$$M_x(a, y) = -D_{11}\left(\frac{\partial^2 w}{\partial x^2}\right)_{x=a} = 0 \tag{5.13d}$$

$$w(x, 0) = 0 \tag{5.13e}$$

$$\theta(x, 0) = \left(\frac{\partial w}{\partial y}\right)_{y=0} = 0 \tag{5.13f}$$

$$M_y(x, b) = -D_{22}\left(\frac{\partial^2 w}{\partial y^2}\right)_{y=b} = 0 \tag{5.13g}$$

$$Q_y = -D_{22}\left[\frac{\partial^3 w}{\partial y^3}\right]_{y=b} - EI\,\frac{\partial^3 (w|_{y=b})}{\partial x^3} = 0 \tag{5.13h}$$

By applying the boundary condition of general form, the coefficients will be obtained, and the shape function will be expressed as

$$w(x, y) = w_0\left(\left(\frac{\mathrm{y}}{b}\right)^2 - \frac{2}{3}\left(\frac{\mathrm{y}}{b}\right)^3 + \frac{1}{6}\left(\frac{\mathrm{y}}{b}\right)^4\right)\sin\frac{\pi x}{\mathrm{a}} \tag{5.14}$$

5.1.4. Explicit Solution

By substituting Eq. (5.14) into Eqs. (5.6), (5.8) and (5.10), and summing them up according to Eq. (5.11), the solution of an eigenvalue problem for local buckling of the prestressed, elastically restrained plate subjected to uniform, in-plane axial compressive load is obtained. After some symbolic computation, the local buckling coefficient for the elastically restrained plate (see Figure 98) can be explicitly expressed as:

$$\mathrm{N}_x = \frac{1}{405\mathrm{a}^2\mathrm{b}\,\pi^2}[6480\lambda^4\mathrm{bD22} - 6480\mathrm{a}^2\mathrm{b}\pi + 2592\lambda^2\mathrm{bD11}\pi + 2880\lambda^2\mathrm{b\,D66}\pi^2 + \mathrm{a}^2\mathrm{b}\,\pi^2(405 + 301\alpha)\mathrm{N_{preb}} + 1080\mathrm{EI}\pi^4] \tag{5.15}$$

where, $\lambda = a/b$ is the aspect ratio of the plate, α is defined in equation 5.9a.As shown in eq. 15, the presence of prestressing increases the buckling load of the plate.

In order to assess the effect of the pate geometry on the prestressing effects, the above equation was solved for a plate structure resembling the web of PRSEUS stringer. The assumed input data reflected the material properties and dimensions of the stringer web. The prestressing load was considered to be the resultant stress system produced in the web of the prestressed PRSEUS stringer. Table 11 shows the parameters used for this analysis.

Table 11. Properties and the prestressing load of the PRSEUS stringer web.

a (mm)	380
b (mm)	35
l	10.9
D11 (GPa-mm^3)	10.44
D22 (GPa-mm^3)	6.75
D66 (GPa-mm^3)	5.18
E (Gpa)	1.40E+11
I (m^4)	4.04E-10
NpreTOP (N/m)	4.38E+05
NpreBOT (N/m)	1

By substituting the above values in Eq. 5.15, the buckling load of prestressed and non-prestressed plates were calculated as 58.8 and 47.2 KN, respectively. This corresponds to ~25% enhancement of budkling load via prestressing.

In order to assess the effect of aspect ratio on the performance of prestressed and non-prestressed plates under compressive in-plane loading, and also determine the correlation between the prestressing benefits and the plate aspect ratio, the buckling loads for prestressed and non-prestressed plates with Table 11 inputs were calculated, with the outcomes presented in Figure 4. These results indicate that prestressing is more effective as the aspect ratio increases, while it becomes negligible for plates with high aspect ratios. Figure 5 presents the predicted benefits of prestressing versus the plate aspect ratio.

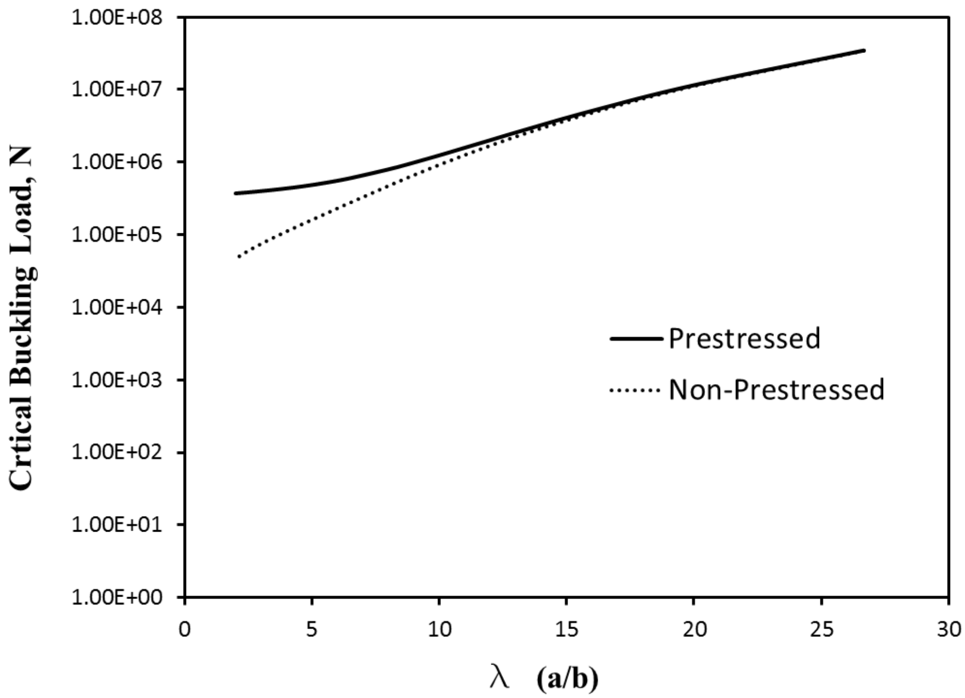

Figure 100. Buckling loads versus aspect ratio of prestressed and non-prestressed plates.

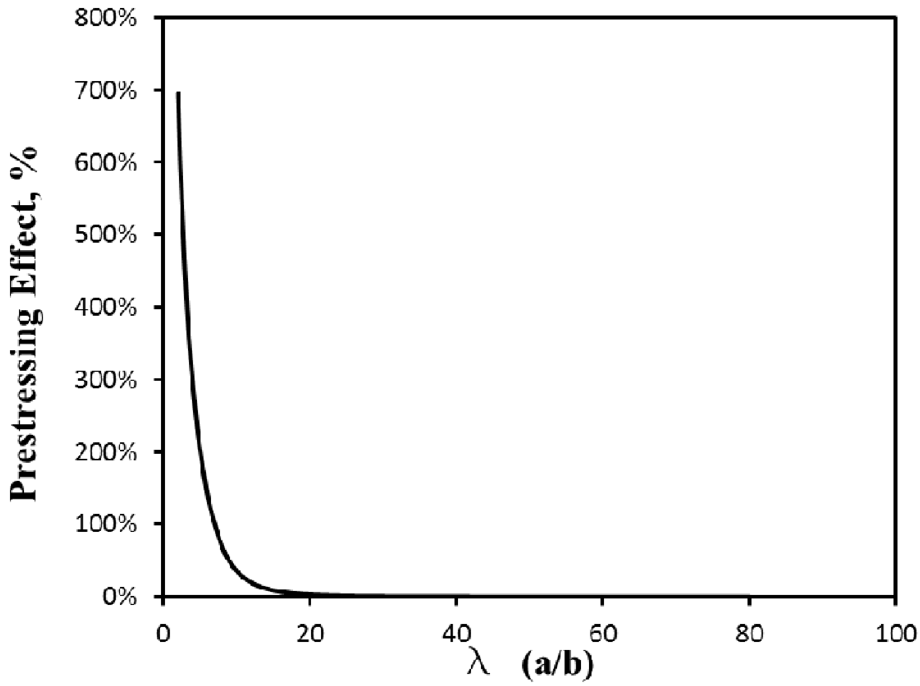

Figure 101. Prestressing benefits versus the plate aspect ratio.

5.2. Finite Element Modeling

5.2.1. Introduction

The PRSEUS stringer subcomponents were analyzed using the ABAQUS package [80]. The analysis accounted for geometric nonlinearities but not plasticity. Structural constituents were modeled using quadrilateral shell elements, except for pultruded composite rods which were modeled as solid elements attached to the top of the stiffener webs. Through-the-thickness stitches were not modeled as their effect on numerical analysis is not significant [81, 82]. The buckling loads and mode shapes were analyzed using the Eigen-value method [83].

The finite element model for a rod-stiffened PRSEUS stringer specimen is shown in Figure 102; this model has 50380 nodes and 46284 elements. The degrees of freedom on the specimen edges and the boundary conditions were defined to reflect the specimen end restraints and edge supports. For a region of one inch from each end, i.e., inside the potted region, all degrees of freedom were restrained except for that allowing for shortening of the specimen.

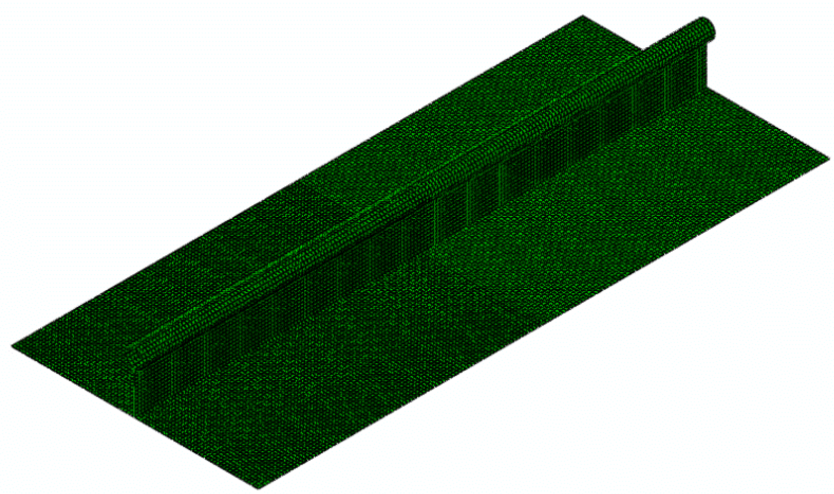

Figure 102. Finite element model of the PRSEUS stringer subcomponent.

5.2.2. Eigen-Value Analysis

Linear elastic analysis was used to identify the buckling mode of the stringer subcomponent under compressive loading. In order to obtain a symmetric loading pattern, the middle of the specimen was restrained, and unit load are applied to the ends of the model. It is noteworthy that by restraining just one end of model and application of load to the other end, the distribution of load will not be uniform. The reason is that at the support end displacement is uniform (zero), while at the loaded end the applied force but not the displacement is uniform.

The potting material was not modeled. Each configuration was first analyzed to determine the linear, nonlinear and buckling behavior using assumed properties for each individual ply. Buckling loads and modes were derived based on a linear prebuckling stress state. Figure 103 shows an example of the buckling mode shaper of the PRSEUS stringer subcomponent.

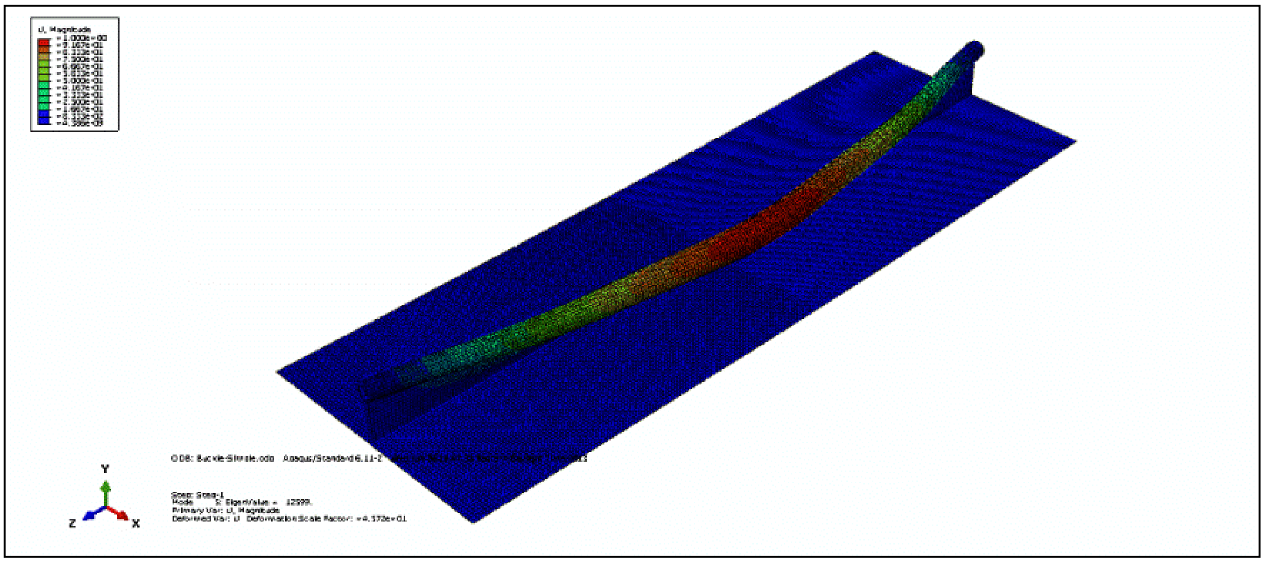

Figure 103. Buckling mode shape of the PRSEUS stringer subcomponent.

5.2.3. Nonlinear Analysis

A nonlinear analysis was conducted with an assumed initial imperfection in the shape of the buckling mode corresponding to minimum buckling. The imperfection mode with amplitude of 0.025 mm (approximately 1/100 of the thinnest skin) was input to trigger nonlinear behavior. Load was applied to the specimen in the form of displacement equal to 10 mm at each end.

Analysis was performed using Ritz method, initial displacement increment set at 0.01 mm and minimum and maximum increment of displacement loading set at 0.01 and 10^{-8} mm, respectively. These limits decide when the change in internal load is significant, and reduce the increment in loading (noting that loading is in term of displacement) accordingly. Properties for each ply in each stack were used in failure analysis. The assumed ply properties for the rod-stiffened specimens are given in Table 12.

Table 12. Material properties used for finite element analysis [32].

Longitudinal Stiffness, GPa	144
Transverse Stiffness, GPa	5
Shear Stiffness, GPa	2.5
Poisson Ratio	0.35
Ply thickness, mm	0.14
Failure compressive longitudinal strain	6500×10^{-6}
Failure tensile longitudinal strain	11000×10^{-6}
Failure compressive transverse strain	6500×10^{-6}
Failure compressive transverse strain	11000×10^{-6}
Failure Shear Strain	20000×10^{-6}

The axial strains throughout the specimen, determined from finite element analysis, are shown in Figure 104.

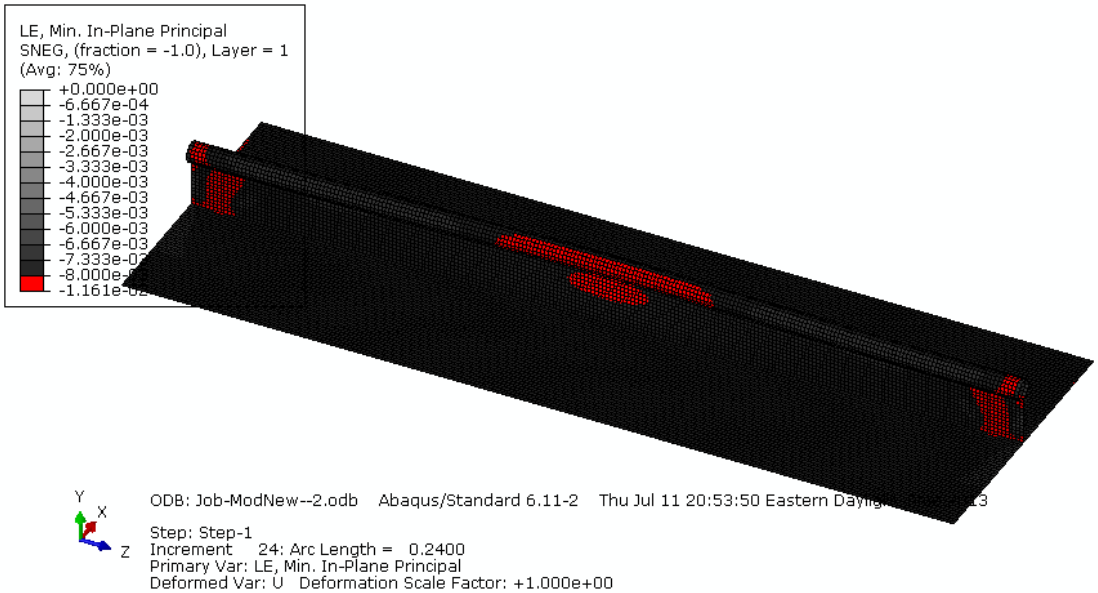

Figure 104. Strain distribution in the PRSEUS stringer subcomponent.

5.2.4. Progressive Failure Analysis

In order to evaluate the effect of failure of each ply on the system behavior, the progressive failure method was employed. In this analysis, compressive loading was applied incrementally to the specimen, and the damage index of each ply was calculated at each increment; once the ply reached to its ultimate capacity, it was removed from the model, and loading was continued on without the failed plies. Hashin model was used in order to take the material degradation into account [84, 85]. The ultimate load obtained from finite element analysis was 201 KN. This value is in good agreement with experimental peak load of 185 KN for non-prestressed PRSUS stringer subcomponents. The finite element analysis prediction of failure load was ~9% higher than the experimental value (compared to experimental results performed on 4 specimens). This difference could be attributed to the assumed properties and support conditions used as inputs to the finite element analysis (for example, end potting plates may not create fully clamped conditions in experiments). Figure 105 shows the experimental and numerically predicted load versus longitudinal strain of non-prestressed PRSEUS stringer subcomponent.

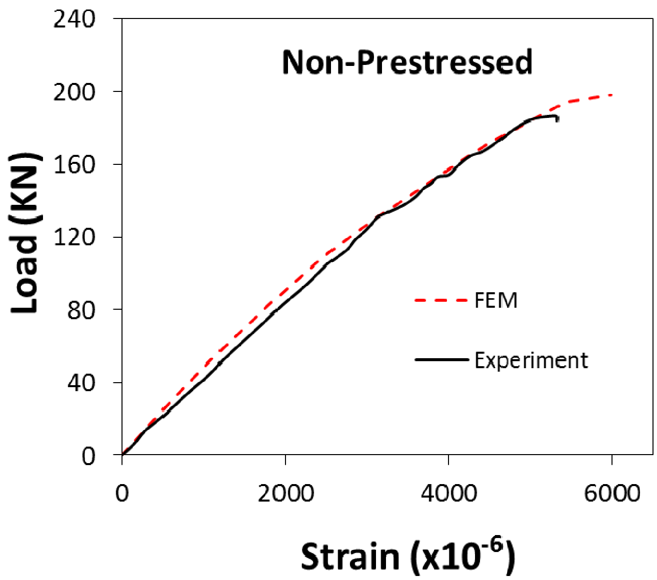

Figure 105. Load versus longitudinal strain obtained through finite element analysis and compression testing of the PRSEUS stringer subcomponent.

5.2.4. Finite Element Analysis of the Prestressed PRSEUS Stringer Subcomponent

The analysis was performed for the stringer subcomponent with application of prestressing. The prestressing load was applied by defining a thermal expansion coefficient, α, for the pultruded rod with that of the remainder of the structure set at zero. Thermal loading, ΔT, was applied to cause prestraining of the pultruded rod: $\varepsilon pre=\alpha.\Delta T$. The thermal expansion coefficient was set to 10^{-3} 1/C, and a thermal load of 8 C was applied (with initial temperature set at 0 C) in order to simulate prestressing of the PRSEUS stringer subcomponent. Subsequent analysis of the subcomponent under load thus reflected the prestressing effect.

The interfacial bond region between the pultruded rod and the multiaxial composite was initially modeled as a thin elastic-plastic material; analysis, however, did not converge. Since failure occurred at mid-span (as observed in experiments), tie interaction was used as the interface zone between the pultruded rod and the multiaxial composite. Figure 106 shows stress distribution after the prestressing step. Finite element analysis verified development of tensile stress profile within the stiffener constituent of the PRSEUS stringer subcomponent.

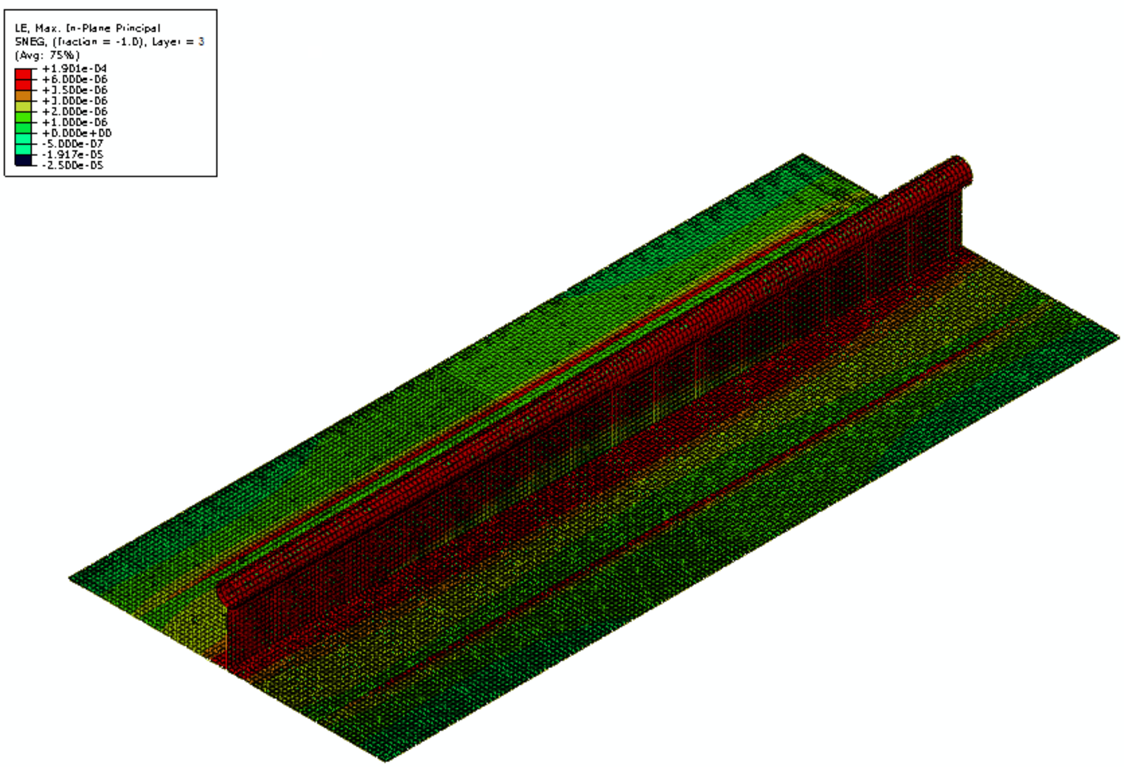

Figure 106. Stress distribution after the prestressing step.

The loading step was performed on the specimen following the analysis procedures used with the non-prestressed model. Loading was continued until the model did not converge. Figure 107 shows the ultimate strain distribution within the prestressed PRSEUS stringer subcomponent. Finite element analysis of the prestressed subcomponent yielded an ultimate compressive load of 279 KN. This is ~15% higher than that obtained in experiments. The difference can be attributed to imperfections and creep deformations in the interfacial area of experimental specimens, which lead to loss of the prestressing force and thus lower the effectiveness of prestressing. According to the outcomes of finite element analysis, prestressing enhanced the ultimate compressive load-carrying of the PRSEUS stringer subcomponent by ~40%. Because of the reasons explained above, the gain in structural performance with prestressing in the experimental work was lower than that predicted by finite element analysis. The finite element analysis prediction and experimental relationships of compressive load versus longitudinal strain are shown in Figure 108.

Figure 107. Longitudinal strain for prestressed PRSEUS stringer

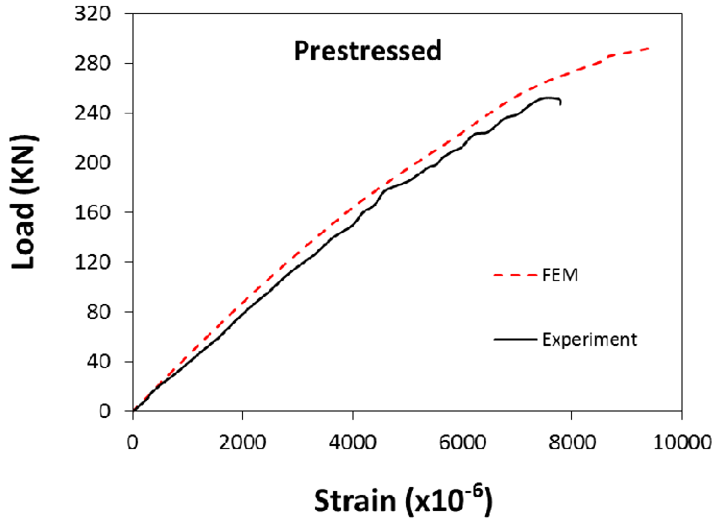

Figure 108. Experimental versus finite element analysis prediction of load versus strain relationship for the prestressed PRSEUS stringer subcomponent.

Chapter 6. Summary and Recommendation

Fiber reinforced composites offer particularly desired performance characteristics under tensile loading; their compressive properties, however, generally fall short of than in tension. The generally inferior material properties of composites in compression together with the buckling modes of failure in compression tend to govern failure of composite structures, leaving their high tensile properties under-utilized. An approach to prestressing which generate a pre-tension in composite structures was investigated in an effort to delay the compressive modes of failure in order to effectively utilize material properties in tension.

6.1. Summary

Throughout this research, comprehensive experimental and numerical investigations were conducted in order to evaluate the contributions of prestressing towards enhancement of the structural performance of composite structures under flexural and compressive loads. A summary of these investigations is presented below.

Analytical and experimental results demonstrated that prestressing can benefit the efficiency of composite structures by inducing a stress system which counteracts the critical stresses developed under service loads. The tensile stress system developed in composite structures upon prestressing favorably shift the stress range developed under flexural loading to delay compressive stress excursions, under service loads, thus benefiting the ultimate load carrying capacity of composite structures. Flexural tests performed on replicated non-prestressed and prestressed composite box sections confirmed that prestressing increases the flexural strength of the composite box section by inducing a tensile prestress system. Prestressing of the composite box section increased the peak load by ~90% ((based on one test) while it added only ~15% to the weight of the structure. The gain in strength-to-weight ratio upon prestressing was ~65% (based on one prestressed and 4 non-prestressed test).

1. Experimental results demonstrated the damaging effect of repeated compressive stress excursions during fatigue loading (i.e., tension-compression fatigue) on the service life of composite structures under fatigue loading. Prestressing of composite structures can introduce tensile stress systems which favorably shift the stress range developed under fatigue loading to avoid compressive stress excursions, and ensure a tensile-tensile fatigue. This shift can significantly improve the fatigue life of composite structures. Flexural fatigue tests performed on non-prestressed and prestressed composite box sections confirmed that prestressing, by shifting tension-compression fatigue to tension-tension fatigue, significantly reduced the rate of stiffness loss under fatigue loading. Prestressing of the composite box section doubled the number of load cycles required to produce 30% stiffness loss when compared with similar non-prestressed sections. Flexural testing of composite box sections to failure indicated that, although the prestressed section were subjected to twice the number of load cycles applied to non-prestressed sections, the ultimate load carrying capacity of prestressed sections was over ~50% more than that of non-prestressed sections.

2. A refined fabrication process for prestressing of the PRSEUS composite structure employing the under-utilized pultruded rod was developed, which did not impose any weight penalty. The setup for fabrication of PRSEUS 'stringer' specimens via the CAPRI approach to resin infusion was established. The fiber volume fraction and void content of the resulting PRSEUS composites were measured, and were compared against those of PRSEUS composites produced by Boeing. The measured value of fiber volume fraction

(62%) was comparable to the 60% fiber volume fraction of Boeing specimens. The measured value of void content (~1.5%) was also within the range (<2%) reported for aerospace composite structures. light-weight and efficient tooling was introduced into the PRSEUS fabrication process for application of the prestressing force.

3. The structural performance of PRSEUS under compressive loads was enhanced by employing prestressing. The prestressing was implemented via application of the preexisting pultruded rod which leave the structure being prestressed with no weight penalty. Fabrications processes of non-prestressed and prestressed composite structures were established to produce pretentioned PRSEUS. Non-prestressed and prestressed pretentioned PRSEUS "stringer" specimens with different level of prestressing were fabricated, and were subjected to compression tests. The contributions of prestressing to structural performance of PRSEUS composite systems were verified in compression tests. The experimentally observed enhancement to buckling strength due to prestressing effects increased by increase of level of prestressing. The maximum level of prestressing which corresponded to exploit of 100% of reserved capacity of the pultruded rod showed 32% (with 95% level of confidence) gain in postbuckling strength of the specimen. Prestressed and non-prestressed PRSEUS frame specimens were subjected to compression tests in order to evaluate the contribution of prestressing towards enhancement of the compressive strength of the relatively large and complex PRSEUS frame specimen. Each PRSEUS frame specimen comprises two stringers (stiffeners) and one frame component. The enhancement realized in the compressive strength of frame specimen through prestressing was over 25% (based on one test).

4. The long-term stability of the prestress system developed in PRSEUS composite structures is important for preserving the structural benefits of prestressing over the life of structural systems. The negligible creep deformations observed in creep tests conducted on pultruded rods and further analyses of the multiaxial composite constituent of prestressed structures suggested creep deformations occur largely at the interfacial bond region between the pultruded rod and the multiaxial composite. This region is not reinforced, and thus relatively large deformations of the polymeric bond region (in spite of the relatively small thickness of this region) tend to govern losses of the prestressing force. Steps were implemented to reduce the losses of prestressing force by limiting the creep deformations within the interfacial bond region in PRSEUS composite structures. Several attempts made in order to reduces the losses of prestressing force through use of creep-resistant adhesive bonds between the pultruded rod and the multi-axial composite constituent of prestressed PRSEUS composite structures. A low-creep adhesive agent was found to perform well in ensuring the stability of prestressing force over time at extreme temperatures. Two similar pretressed PRSEUS specimens were fabricated with this (AF-162-2A) adhesive agent, which were subjected to room temperature and 85°C (185°F) temperature over extended time periods. The creep deformations occurred largely within 36 hours. The prestressing force experienced losses of about ~4% and ~22% over 36 hours at room temperature and at 85°C temperature, respectively. It should be noted that the approach developed in the project to design of prestressed PRSEUS composite structures has assumed effective prestress levels (after losses) of 80%. Hence, the loss of 22% produced under extended exposure to the extreme service temperature of 85°C is very close to the assume level of 20%. Given the

relatively rapid rate of creep deformations in polymers and composites, the prestress level tends to stabilize after 36 hours, and limited losses are expected to occur thereafter.

5. In order to evaluate the stability of prestressed PRSEUS under thermal cycling, freeze-thaw test was conducted. For this purpose, a prestressed PRSEUS stringer was fabricated and processed and subjected to freez-thaw cycles. The specimen was subjected to 10 cycles, each cycle consisted of 8 hours at freezing temperature of -30oC followed by 8 hours at 50^{o}C and 100% humidity. The prestressing level was recorded during the throughout the test. The results showed that level of initial prestressing was dropped by ~10-15% (based on one test) which was combination of creep loss and freez-thaw effect. However, the 10-15% loss is still under the assumed prestressing loss of 20%.

6. An analytical approach was developed in order to assess the benefits of presstressing toward increasing the buckling threshold of plates. The first variational principle of total potential energy was employed to explicitly express the buckling load of the plate structures. The explicit expression included prestressing as an input. As expected, the predicted buckling force increased with prestressing. Analytical evaluation of the buckling load for plates with different aspect ratios indicated that the benefits of prestressing are more pronounce for plates with aspect ratios close to 1. Also, analytical investigations indicated that prestressing can raise the critical buckling load of the PRSEUS web by ~25%.

7. The contributions of prestressing to the structural performance of PRSEUS stringer subcomponent was evaluated by finite element modeling. Two cases were evaluated: (i) non-prestressed; and (ii) prestressed (where the prestressing effect was induced using a thermal expansion coefficient mismatch between the pultruded rod and the muliaxial composite constituents of PRSEUS). The ABAQUS finite element analysis package was

employed for numerical modeling of prestressed and non-prestressed systems. Eigen-value, non-linear, progressive failure analysis procedures were employed in order to find the peak loads of the prestressed and non-prestressed models under compressive loading. The ultimate compressive load-carrying capacities of prestressed and non-prestressed PRSEUS stringer subcomponents were found to be 201 and 279 KN, respectively, indicating 38% gain upon prestressing. These values are somewhat higher than the corresponding experimental results; the predictions of finite element analyses were ~9% and ~15% higher than experimental values for non-prestressed and prestressed subcomponent, respectively. These deviations from experimental results were attributed to the imperfections in interfacial bonding of pultruded rod to multiaxial composite, processing of PRSEUS, and loading and support conditions during experiments.

6.2. Recommendations

The following subjects need to be addressed in future works as this investigation would not cover them thoroughly.

Stability of Prestressing

In order to consider uncertainty sources associated with material and prestressing system, replicated tests on the following experimental works must be implemented:

i. Creep of specimens at both room and elevated temperature

ii. Thermal/freez-thaw cycling

The above tests can help to select more compatible materials (adhesive agents) for the prestressed composite structures with more stable prestressing system.

Fatigue

Also, the above tests should be performed on scaled-up specimens to evaluate stability of prestressing in more complex structures.

Another issue should be addressed is performance of prestressed rod-stiffened panel under cyclic load. Moreover, the effect of cyclic loading on specimen with impact damaged is a critical issue which should be addressed by experimental work.

The fatigue life of more complex specimens is important and should be considered for future experimental works.

Realistic Loading and Larger Specimens

In order to assess efficiency of prestressing in large PRSEUS panels, fabrication and prestressing of full scale panel is required. The final goal of prestressing is to enhance structural efficiency of large panels under all load combinations. As PRSEUS is under both compressive loads and internal cabin pressure, the prestressed large scale panel should be loaded according to its designs loads.

New Design

Within this investigation the prestressing was employed to enhance structural performance of the available PRSEUS design. In order to realize the weigh saving realized through prestressing, a new design of prestressed PRSEUS for the service loads which the PRSEUS was designed based on and considering the prestressing should be implemented. A comparison between the new design and current PRSEUS design will show prestressing benefits in term of weight saving.

Comprehensive Numerical Study and Optimization

The finite element modeling used in this study can be employed and expanded in order to predict behavior of more complex specimens (structure with multiple stringers and frame componenets) under more complex loading. Effect of initial damage in different constituents of the model and prediction of damage propagation under static, dynamic, and cyclic loads should be evaluated numerically. Also, ballistic impact load on different constituents of the large structure can be numerically evaluated.

By using numerical analysis on models with different layup and material properties, optimum design for prestress PRSEUS (and other rod-stiffened panels) shall be assessed.

BIBLIOGRAPHY

BIBLIOGRAPHY

1. Reinoso, J., et al., *Postbuckling behaviour of a pressurized stiffened composite panel. Part I: Experimental study.* Composite Structures, 2011.

2. Riks, E., *Buckling and post-buckling analysis of stiffened panels in wing box structures.* International Journal of Solids and Structures, 2000. **37**(46): p. 6795-6824.

3. Buch, A., *Prediction of the comparative fatigue performance for realistic loading distributions.* Progress in Aerospace Sciences, 1997. **33**(5-6): p. 391-430.

4. Nijssen, R.P.L., *Fatigue life prediction and strength degradation of wind turbine rotor blade composites.* Contractor Report SAND2006-7810P, Sandia National Laboratories, Albuquerque, NM, 2006.

5. Hu, Z. and X. Du, *Reliability analysis for hydrokinetic turbine blades.* Renewable Energy, 2012. **48**: p. 251-262.

6. Hayes, M.D., et al., *Performance of tube and plate fiberglass composite bridge deck.* Journal of Composites for Construction, 2000. **4**(2): p. 48-55.

7. Kato, Y.K., Masaki; Hu, Ning; Fukunaga, Hisao, *Optimum design of composite wing considering stiffened panel buckling.* Nippon Kikai Gakkai Ronbunshu, A Hen/Transactions of the Japan Society of Mechanical Engineers, Part A, 2004. **70**(3): p. 479-486.

8. Guo, S., *Aeroelastic optimization of an aerobatic aircraft wing structure.* Aerospace Science and Technology, 2007. **11**(5): p. 396-404.

9. Petersen, D., R. Rolfes, and R. Zimmermann, *Thermo-mechanical design aspects for primary composite structures of large transport aircraft.* Aerospace Science and Technology, 2001. **5**(2): p. 135-146.

10. Ryu, C.-Y.L., Jung-Ryul; Kim, Chun-Gon; Hong, Chang-Sun, *Buckling behavior monitoring of a composite wing box using multiplexed and multi-channeled built-in fiber Bragg grating strain sensors.* NDT and E International, 2008. **41**(7): p. 534-543.

11. Falzon, B.G., K.A. Stevens, and G.O. Davies, *Postbucking behaviour of a blade-stiffened composite panel loaded in uniaxial compression.* Composites - Part A: Applied Science and Manufacturing, 2000. **31**(5): p. 459-468.

12. Kong, C.W.L., I. Ch; Kim, Ch G.; Hong, Ch S., *Postbuckling and failure of stiffened composite panels under axial compression.* Composite Structures, 1998. **42**(1): p. 13-21.

13. Meeks, C., E. Greenhalgh, and B.G. Falzon, *Stiffener debonding mechanisms in post-buckled CFRP aerospace panels.* Composites Part A: Applied Science and Manufacturing, 2005. **36**(7): p. 934-946.

14. Stevens, K.A., R. Ricci, and G.A.O. Davies, *Buckling and postbuckling of composite structures.* Composites, 1995. **26**(3): p. 189-199.

15. Ryu, C.-Y., et al., *Buckling behavior monitoring of a composite wing box using multiplexed and multi-channeled built-in fiber Bragg grating strain sensors.* NDT and E International, 2008. **41**(7): p. 534-543.

16. Kong, C.W., et al., *Postbuckling and failure of stiffened composite panels under axial compression.* Composite Structures, 1998. **42**(1): p. 13-21.

17. Goutianos, S., T. Peijs, and C. Galiotis, *Comparative assessment of stress transfer efficiency in tension and compression.* Composites Part A: Applied Science and Manufacturing, 2002. **33**(10): p. 1303-1309.

18. Bai, J. and S.L. Phoenix, *Compressive failure model for fiber composites by kink band initiation from obliquely aligned, shear-dislocated fiber breaks.* International Journal of Solids and Structures, 2005. **42**(7): p. 2089-2128.

19. Effendi, R.R., J.J. Barrau, and D. Guedra-Degeorges, *Failure mechanism analysis under compression loading of unidirectional carbon/epoxy composites using micromechanical modelling.* Composite Structures, 1995. **31**(2): p. 87-98.

20. Prabhakar, P. and A.M. Waas, *Micromechanical Modeling to Determine the Compressive Strength and Failure Mode Interaction of Multidirectional Laminates.* Composites Part A: Applied Science and Manufacturing, 2013.

21. Lee, S. and A.M. Waas, *Compressive response and failure of fiber reinforced unidirectional composites.* International Journal of Fracture, 1999. **100**(3): p. 275-306.

22. Butler, R., et al., *Compressive fatigue limit of impact damaged composite laminates.* Composites Part A: Applied Science and Manufacturing, 2007. **38**(4): p. 1211-1215.

23. JI, W. and A. WAAS, *Progressive failure analysis for the interaction of interlaminar and intralaminar failure modes in composite structures with an initial delamination.* Aeronautical Journal, 2013. **117**(1187): p. 71-85.

24. Kardomateas, G.A., A.A. Pelegri, and B. Malik, *Growth of internal delaminations under cyclic compression in composite plates.* Journal of the Mechanics and Physics of Solids, 1995. **43**(6): p. 847-868.

25. Van Paepegem, W. and J. Degrieck, *Tensile and compressive damage coupling for fully-reversed bending fatigue of fibre-reinforced composites.* Fatigue and Fracture of Engineering Materials and Structures, 2002. **25**(6): p. 547-561.

26. Caprino, G. and A. D'Amore, *Fatigue life of graphite/epoxy laminates subjected to tension-compression loadings.* Mechanics Time-Dependent Materials, 2000. **4**(2): p. 139-154.

27. Beukers, A., H. Bersee, and S. Koussios, *Future aircraft structures: from metal to composite structures.* Composite Materials, 2011: p. 1-50.

28. Baker, A.A. and S. Dutton, *Composite materials for aircraft structures*. 2004: AIAA (American Institute of Aeronautics & Astronautics).

29. Elaldi, F., *Structural Efficiency and Post-buckling Strength of J-and Hat-stiffened Composite Panels.* Journal of Reinforced Plastics and Composites, 2010. **29**(10): p. 1590-1594.

30. Wang, X., et al., *Influence of tool assembly schemes and integral molding technologies on compaction of T-stiffened skins in autoclave process.* Journal of Reinforced Plastics and Composites, 2010. **29**(9): p. 1311-1322.

31. Gigliotti, M., et al., *Weight optimisation of damage resistant composite panels with a posteriori cost evaluation.* Composite Structures, 2009. **88**(2): p. 312-322.

32. Velicki, A. and D. Jegley, *PRSEUS development for the hybrid wing body aircraft.* 2011.

33. Jegley, D.C., *Failure at Frame-Stringer Intersections in PRSEUS Panels.* 2012.

34. Jegley, D.C., *Experimental Behavior of Fatigued Single Stiffener PRSEUS Specimens.* 2009.

35. Jian, Z. and X. Jinwu, *Nonlinear Aeroelastic Response of High-aspect-ratio Flexible Wings.* Chinese Journal of Aeronautics, 2009. **22**(4): p. 355-363.

36. Tuttle, M., *A mechanical/thermal analysis of prestressed composite laminates.* Journal of composite materials, 1988. **22**(8): p. 780-792.

37. Dvorak, G.J. and A.P. Suvorov, *The effect of fiber pre-stress on residual stresses and the onset of damage in symmetric laminates.* Composites science and technology, 2000. **60**(8): p. 1129-1139.

38. Hadi, A. and J. Ashton, *On the influence of pre-stress on the mechanical properties of a unidirectional GRE composite.* Composite structures, 1997. **40**(3): p. 305-311.

39. Fancey, K.S., *Viscoelastically prestressed polymeric matrix composites–Potential for useful life and impact protection.* Composites Part B: Engineering, 2010. **41**(6): p. 454-461.

40. Schulte, K. and R. Marissen, *Influence of artificial pre-stressing during curing of CFRP laminates on interfibre transverse cracking.* Composites science and technology, 1992. **44**(4): p. 361-367.

41. Ha, S.K., H.H. Han, and Y.H. Han, *Design and manufacture of a composite flywheel press-fit multi-rim rotor.* Journal of Reinforced Plastics and Composites, 2008. **27**(9): p. 953-965.

42. Portmann, H., *Process for manufacturing a pre-stressed fiber-reinforced high pressure vessel*, 2003, Google Patents.

43. Littlefield, A. and E. Hyland, *Prestressed Carbon Fiber Composite Overwrapped Gun Tube*, 2006, DTIC Document.

44. Kerboua, B. and A. Tounsi, *Impact of the Fiber-reinforced Plastic (FRP) and the Thermal Effect for the Interfacial Stresses.* Journal of Reinforced Plastics and Composites, 2010. **29**(6): p. 921-935.

45. Krishnamurthy, S., *Pre-stressed advanced fibre reinforced composites fabrication and mechanical performance.* 2006.

46. Dano, M.L., M. Jean-St-Laurent, and A. Fecteau, *Morphing of Bistable Composite Laminates Using Distributed Piezoelectric Actuators.* Smart Materials Research, 2012. **2012**.

47. Daynes, S., K. Potter, and P. Weaver, *Bistable prestressed buckled laminates.* Composites Science and Technology, 2008. **68**(15): p. 3431-3437.

48. Daynes, S., et al., *Bistable prestressed symmetric laminates.* Journal of composite materials, 2010. **44**(9): p. 1119-1137.

49. Almeida, A., et al., *The effect of piezoelectrically induced stress stiffening on the aeroelastic stability of curved composite panels.* Composite Structures, 2012. **94**(12): p. 3601-3611.

50. Triantafillou, T.C., N. Deskovic, and M. Deuring, *Strengthening of concrete structures with prestressed fiber reinforced plastic sheets.* ACI structural Journal, 1992. **89**(3).

51. Wight, R.G., M.F. Green, and M.A. Erki, *Prestressed FRP sheets for poststrengthening reinforced concrete beams.* Journal of Composites for Construction, 2001. **5**(4): p. 214-220.

52. Kim, Y.J., R. Gordon Wight, and M.F. Green, *Flexural strengthening of RC beams with prestressed CFRP sheets: Using nonmetallic anchor systems.* Journal of Composites for Construction, 2008. **12**(1): p. 44-52.

53. Malekzadeh, K., et al., *Dynamic response of In-plane Pre-stressed sandwich panels with a viscoelastic flexible core and different boundary conditions.* Journal of Composite Materials, 2006. **40**(16): p. 1449-1469.

54. Cheng, Z.-Q. and S. Kitipornchai, *Prestressed composite laminates featuring interlaminar imperfection.* International Journal of Mechanical Sciences, 2000. **42**(3): p. 425-443.

55. Jones, R.M., *Mechanics of composite materials*. Vol. 2.

56. Leonhardt, F., *Prestressed concrete: design and construction*. 1964: W. Ernst.

57. Sayyar, M., P. Soroushian, and R. Weerasiri, *Evaluation of the prestressing effects on the fatigue life of composite box sections.* Journal of Composite Materials, 2012.

58. Akerman, J., *Sustainable air transport - On track in 2050.* Transportation Research Part D: Transport and Environment, 2005. **10**(2): p. 111-126.

59. Li, V. and A. Velicki. *Advanced PRSEUS Structural Concept Design and Optimization*. in *12th AIAA/ISSMO Multidisciplinary Analysis and Optimization Conference*. 2008.

60. Woods, J., Modin, A.E., Hawkins, R.D. and Hanks, D.J. , *"Controlled Atmospheric Pressure Infusion Process"*, I.P. WO, Editor 2003.

61. Niggemann, C., et al., *Experimental investigation of the controlled atmospheric pressure resin infusion (CAPRI) process.* Journal of Composite Materials, 2008. **42**(Compendex): p. 1049-1061.

62. Outwater, J.O. and M.C. Murphy, *FRACTURE ENERGY OF UNIDIRECTIONAL LAMINATES.* Modern Plastics, 1970. **47**(9): p. 160-&.

63. Wilkinson, L., *SYSTAT for Windows: statistics, graphics, data, getting started, version 5*. 1992: Systat.

64. Brown, M.B. and A.B. Forsythe, *Robust tests for the equality of variances.* Journal of the American Statistical Association, 1974. **69**(346): p. 364-367.

65. Govindarajan, S., N.A. Langrana, and G.J. Weng, *Experimental and theoretical study of creep of a graphite/epoxy woven composite.* Polymer Composites, 1996. **17**(3): p. 353-361.

66. Goertzen, W.K. and M.R. Kessler, *Creep behavior of carbon fiber/epoxy matrix composites.* Materials Science and Engineering A, 2006. **421**(1-2): p. 217-225.

67. Soliman, E., U.F. Kandil, and M. Reda Taha, *Limiting shear creep of epoxy adhesive at the FRP-concrete interface using multi-walled carbon nanotubes.* 2011.

68. Nawy, E.G., *Fundamentals of high-performance concrete*. 2001: Wiley. com.

69. Zou, C., et al., *Degradation of mechanical properties of concrete caused by freeze-thaw action [J]*. Journal of Building Structures, 2008. **1**: p. 017.

70. Chajes, M.J., T.A. Thomson Jr, and C.A. Farschman, *Durability of concrete beams externally reinforced with composite fabrics.* Construction and building materials, 1995. **9**(3): p. 141-148.

71. Green, M.F., et al., *Effect of freeze-thaw cycles on the bond durability between fibre reinforced polymer plate reinforcement and concrete.* Canadian journal of civil engineering, 2000. **27**(5): p. 949-959.

72. Toutanji, H. and P. Balaguru, *Durability characteristics of concrete columns wrapped with FRP tow sheets.* Journal of materials in civil engineering, 1998. **10**(1): p. 52-57.

73. Abdo, Z. and H. Aglan, *Analysis of aircraft adhesive joints under combined thermal and mechanical cyclic loadings.* Journal of adhesion science and technology, 1997. **11**(7): p. 941-956.

74. Brush, D.O. and B.O. Almroth, *Buckling of bars, plates, and shells*. Vol. 6. 1975: McGraw-Hill New York.

75. Sokolnikoff, I.S. and R.D. Specht, *Mathematical theory of elasticity*. Vol. 83. 1956: McGraw-Hill New York.

76. Webber, J., P. Holt, and D. Lee, *Instability of carbon fibre reinforced flanges of I section beams and columns.* Composite structures, 1985. **4**(3): p. 245-265.

77. Bank, L.C. and J. Yin, *Buckling of orthotropic plates with free and rotationally restrained unloaded edges.* Thin-Walled Structures, 1996. **24**(1): p. 83-96.

78. Qiao, P. and L. Shan, *Explicit local buckling analysis of rotationally restrained composite plates under biaxial loading.* International Journal of Structural Stability and Dynamics, 2007. **7**(03): p. 487-517.

79. Qiao, P., et al., *Local buckling analysis of restrained orthotropic plates under generic in-plane loading.* Journal of Engineering Mechanics, 2012.

80. Simulia, D., *ABAQUS 6.11 Analysis User's Manual.* Abaqus 6.11 Documentation, 2011: p. 22.2.

81. McGowan, D.M., C.G. Davila, and D.R. Ambur. *Damage progression in buckle-resistant notched composite plates loaded in uniaxial compression*. in *Proceedings of the AIAA/ASME/ASCE/AHS/ASC 42nd Structures, Structural Dynamics & Materials Conference, April*. 2001.

82. Karal, M., *AST composite wing program: executive summary*. 2001.

83. Simulia, D., *Abaqus 6.11 theory manual*. Providence, RI, USA: DS SIMULIA Corp, 2011.

84. Hashin, Z., *Fatigue Failure Criteria for Unidirectional Fiber Composites*, 1980, DTIC Document.

85. Hashin, Z. and A. Rotem, *A fatigue failure criterion for fiber reinforced materials.* Journal of composite materials, 1973. **7**(4): p. 448-464.